QATAR UNIVERSITY

COLLEGE OF ENGINEERING

A HYBRID NONLINEAR VIBRATION ENERGY HARVESTER FOR REMOTE SENSING APPLICATIONS

BY

MUHAMMAD HAFIZH

A Thesis Submitted to

the College of Engineering

in Partial Fulfillment of the Requirements for the Degree of

Masters of Science in Mechanical Engineering

January 2023

COMMITTEE PAGE

The members of the Committee approve the Master's Thesis of
Muhammad Hafizh defended on January 2023.

Prof. Asan Gani Abdul Muthalif
Thesis/Dissertation Supervisor

Prof. Sadok Sassi
Committee Member

Prof. John-John Cabibihan
Committee Member

Prof. Faris Tarlochan
Committee Member

Prof. Khairul Azwan Ismail
Committee Member

Approved:

Khalid Kamal Naji, Dean, College of Engineering

ABSTRACT

Hafizh, Muhammad, Masters: January: 2023, Masters of Science in Mechanical Engineering.

Title: A Hybrid Nonlinear Vibration Energy Harvester for Remote Sensing Applications

Supervisor of Thesis: Asan, G.A, Muthalif.

Energy harvesting mechanisms can be used to extract energy from ambient surroundings to power small electronic devices which has a significant advantage in realizing self-sustaining wireless devices. The piezoelectric energy harvester was modeled with a Macro Fiber Composite (MFC) P2-type while the electromechanical transduction was modeled by an elastic magnet coupled to the bluff body movement. A numerical solver was used to estimate harvestable voltage for this submerged hybrid energy harvester model by using ordinary differential equations. Computational fluid dynamics and finite element analysis with ANSYS were used to visualize the response in synchronization and output the voltage extracted from the harvesting mechanisms. Increasing the water velocity increases the overall output voltage and is a maximum at the natural frequency of the system when synchronization phenomena is observed. Broadband energy harvester is achieved by attaching magnets on the bluff body and is useful for increasing the harvestable range of variable flows. While conventional narrowband energy harvesters are still superior when near the natural frequency, the magnet coupling broadens the synchronization range of the harvesters by 35%. Implementing a hybrid piezoelectric-electromagnetic energy harvesting system increased the voltage output by up to 23% compared to a conventional piezoelectric energy harvester.

DEDICATION

I dedicate this work to both of my parents for providing me with the support and guidance to pursue higher education with the necessary tools and mindset.

ACKNOWLEDGMENTS

Alhamdulillah, primarily I am profoundly grateful to Allah for providing all the opportunities, good health and dedication that led to this documentation of the thesis. I would like to acknowledge the support of my family members and my friends for encouraging me to pursue education beyond a Bachelor's Degree. I would like to thank Prof. Dr. Asan Muthalif for his continued support and mentorship during the past 2 years; I learnt an extensive amount about academia and critical thinking under his tutelage. I would like to also thank the support of Dr. Jamil Renno, Dr. Mohammed Paurobally, Dr. Sadok Sassi and the other faculty members of the Department of Mechanical Engineering for laying the foundation to my learning. Finally, I would like to acknowledge the support of Qatar University for providing all the needs to achieve the requirements of this study which included scholarships, funding, and access.

TABLE OF CONTENTS

LIST OF TABLES

LIST OF FIGURES

NOMENCLATURE OF HYBRID ENERGY HARVESTER

Units	Description	Symbol
ρ_{piezo}	Piezoelectric Material density	kg/m^3
$\rho_{cylinder}$	Circular cylinder oscillator density	kg/m^3
ρ_{fluid}	Fluid density	kg/m^3
A	Cross-section of piezoelectric	m^2
K	Piezoelectric stiffness	N/m
D	Cylinder bluff body diameter	m
K_{trans}	Transduction gain	$-$
K_p	Proportional gain	$-$
C	Piezoelectric Capacitance	nF
L_1	Length of layer	m
L	Length of the beam	m
b	Width of the beam	m
h	The thickness of the beam	m
H_a	Cylinder height	m
a	Force application distance point	m
α	Voltage-induced bending factor	$A \cdot s/m$
J_{wt}	Cylinder inertia moment	$kg \cdot m^2$
C^S	Clamp capacitance for piezoelectric transducer	F
R_L	Load Resistance	Ω
C_L	Lift coefficient evolution	$-$
Θ	Electromechanical Coupling Coefficient	$N\,V^{-1}$

CHAPTER 1: INTRODUCTION

1.1 Background

Industrialized countries around the world transport water, oil, and gas through pipeline networks spanning thousands of kilometers. The infrastructure built around this distribution requires strict monitoring and inspections to prevent leakage or failures, which can be detrimental to the environment or human health and safety. These monitoring techniques employ high-accuracy sensors that capture a wide range of information transmitted to a data center for analysis and decision-making. Real-time information monitoring requires an integrated system of sensors, wireless communication routers, and a power supply to relay the information effectively. Implementing an integrated system like that requires well-optimized and efficient components and a smart decision-making system. Powering up microelectromechanical systems (MEMS) used in such systems often requires energy to power the sensors, storage, and communication devices. In Qatar, temperatures can go up to 50^{o}C during summer, and receives little rainfall annually. Lifespan degradation and periodic replacement would make the use of batteries unfeasible, especially with the large scope of pipeline applications. Main's power (from fossil fuels) supply is sometimes used near urban areas but becomes challenging as the pipelines extend to more isolated and harder-to-reach areas. Alternatively, renewable and sustainable sources of electricity can be considered, such as solar power. Although solar panels possess a large power density, their performance is often limited by soft shading or hard shading caused by air pollution or dust accumulation, respectively [1]. Figure 1 illustrates the wireless node architecture and the comparison of available energy supplies.

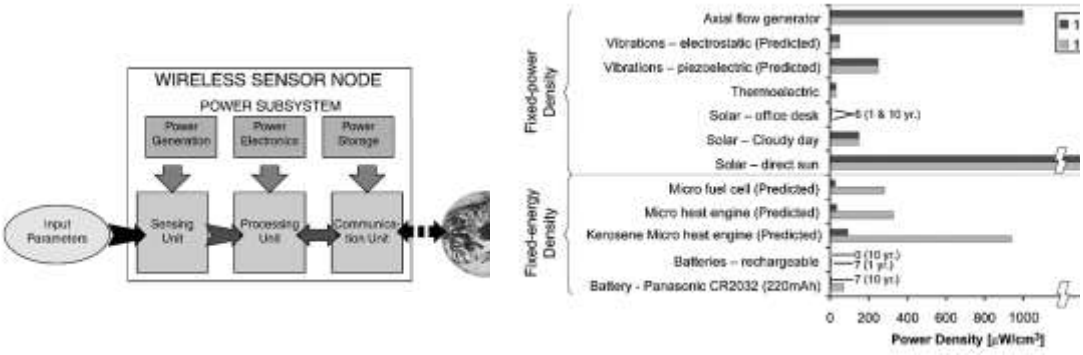

(a) (b)

Figure 1 Integrated System Overview; (a) Wireless sensor node architecture; (b) Comparison of energy sources for nodes [2]

Vibration-based energy harvesting is an emerging method for powering small devices as it utilizes the surrounding medium or applications in converting kinetic energy into electrical energy. Self-sustaining wireless devices have recently been shown to be viable with the addition of control systems and storage mechanisms [3].

Piezoelectric energy harvesting (PEH) is often selected in research because it offers excellent performance, versatility, and compactness at a competitive price [4–7]. The patches are usually attached to oscillating beams that generate charge when mechanically stressed. Optimization work in the literature has provided parameter insights to maximize PEH [8]. Although the power density of piezoelectric-based vibration energy harvesters is not as high as other alternatives shown in Figure 1, the flexibility to use multiple configurations can improve the efficiency at any node. Figure 2 shows piezoelectric arrays used to harvest energy.

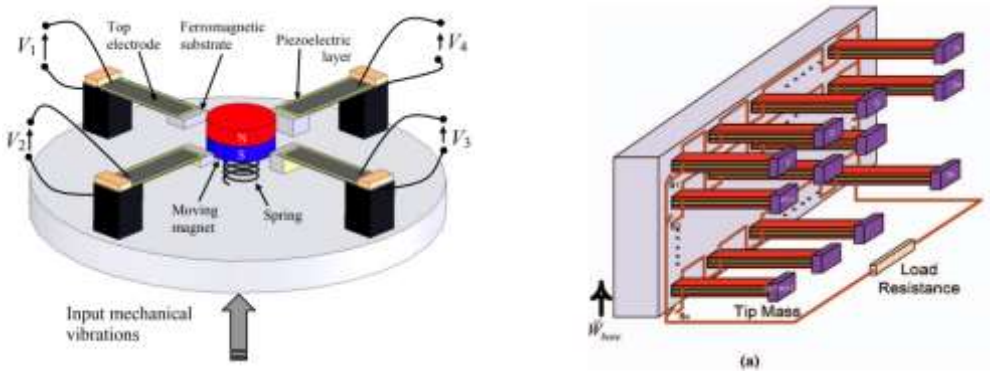

(a) (b)

Figure 2 Piezoelectric array configurations; (a) nonlinear harvester array with magnet oscillator; (b) piezoelectric bimorph array in series-parallel connection [9,10]

Electromagnetic energy harvesting produces an electrical charge when a magnet is moving inside a coil of wire. The instantaneous motions can be excited by applied vibration [11]. Electromagnetic generators are also employed in energy harvesting but are bulkier than PEH and generally reserved for larger devices [12]. A hybrid system is one where two or more multiple systems are integrated; a hybrid energy harvester can harvest from both piezoelectric and electromagnetic systems, for example. Recently, hybrid systems have been shown to outperform conventional piezoelectric composite strains [13,14]. Challa et al. [15] highlighted that adding an electromagnetic system to a piezoelectric energy harvester improved the power output by 30%.

Broadband energy harvesting applications are usually implemented to capture a broader range of harvestable frequencies with additional parameters. Linear vibration energy harvesters operate close to the structure's natural frequency, called the resonance frequency, where the deformation is the largest. The main drawback of this approach is that resonance is narrow-banded and will not perform well if ambient conditions are dynamic (i.e., water flow inside the pipe is continuously changing). Nonlinear vibration energy harvesters exploit vibration in the nonlinear regime to broaden the bandwidth

so that the harvester is more responsive to random vibrations and is more robust. Dauda et al. [16] investigated the broadband properties of piezoelectric beams by introducing nonlinear magnetic forces. Ali et al. [17] highlighted the piezoelectric plate properties in enhancing energy harvesting properties.

Energy harvesting from pipework did not receive a lot of attention in the literature. Most of the current work in vibration energy harvesting of flowing mediums looks at flow-induced vibration effects. Here, the periodic oscillation of vortices around bluff bodies is well-documented and can be used with piezoelectricity [18–21]. The addition of a hybrid electromagnetic oscillator with a macrofibre composite piezoelectric patch shown further increases the performance in comparison to conventional vibration-based energy harvesters from vortices. As for powering a network of sensors for monitoring purposes, there is an apparent gap in the application of energy harvesting from vibrating pipework for condition monitoring purposes.

Efficiency is the main factor in energy harvesting, especially with vibration-based energy harvesting for MEMS where frictional heat losses decrease the overall output. In this research, a piezoelectric and electromagnetic energy harvester is proposed. Studying nonlinear wave propagation characteristics in a finite strain of a fixed, periodic structure is a rapidly expanding research field.

1.2 Research Objectives

Objectives of the project are to:

i) Derive mathematical model for the piezoelectric nonlinear harvester on hybrid model.

ii) Perform numerical simulation to estimate and optimize the hybrid harvesters to

increase harvesting efficiency.

iii) Design and develop a prototype model for the hybrid piezoelectric-electromagnetic harvester.

iv) Obtain experimental verification in a lab-scale water monitoring system that enables power and regulates water flow in pipes in various operational scenarios.

1.3 Research Significance

i) ***Eco-economy and Environment:*** The outcome of the research can have a significant impact on society and the environment by realizing lower costs and more efficient sensors for improved monitoring. This research will train graduate and undergraduate students in the modeling, design, and characterization of nonlinear vibration-based energy harvester devices. The students will be trained to use analytical skills, through the application of perturbation theory, and numerical skills, through the implementation of various numerical techniques, and unify both skills to gain more in-depth insight into the behavior of such devices, which are important for qualifying today's engineers for the emerging energy scavenging technology field.

ii) ***Training of Personnel:*** This research will also support teaching a course in the modeling of Energy Harvester devices in mechanical vibratory systems concentration in the Department of Mechanical & Industrial Engineering. This will provide in-depth training in the energy harvester technology developed in the proposed research project.

iii) ***Intellectual Property:*** In addition to the energy harvester unit, it must be

emphasized that the constituent technology can lead to building a capacity to apply the outcomes of this work in many other applications, such as energy harvesting vibration in roads and sea waves. This project will also lead to self-powered products that can be used in a variety of remote-sensing applications. It is envisaged that the proposed project will produce intellectual properties of sustainable wireless remote sensing.

iv) ***Benefits to Qatar:*** The total estimated length of the oil and gas pipelines in Qatar in 2013 of 3,830 km. The implementation of this hybrid energy harvester is of immense importance in the areas of wireless communication/signal processing as well as sensing electronics used in numerous harsh environment applications or pipelines to power sensors to monitor physical and chemical parameters in the pipelines. The outcome of this work can be extended to harvest energy from many vibration sources, such as roads and sea waves.

1.4 Research Methodology

A novel implementation of a tunable nonlinear hybrid energy harvester is proposed in this project shown in Figure 3.

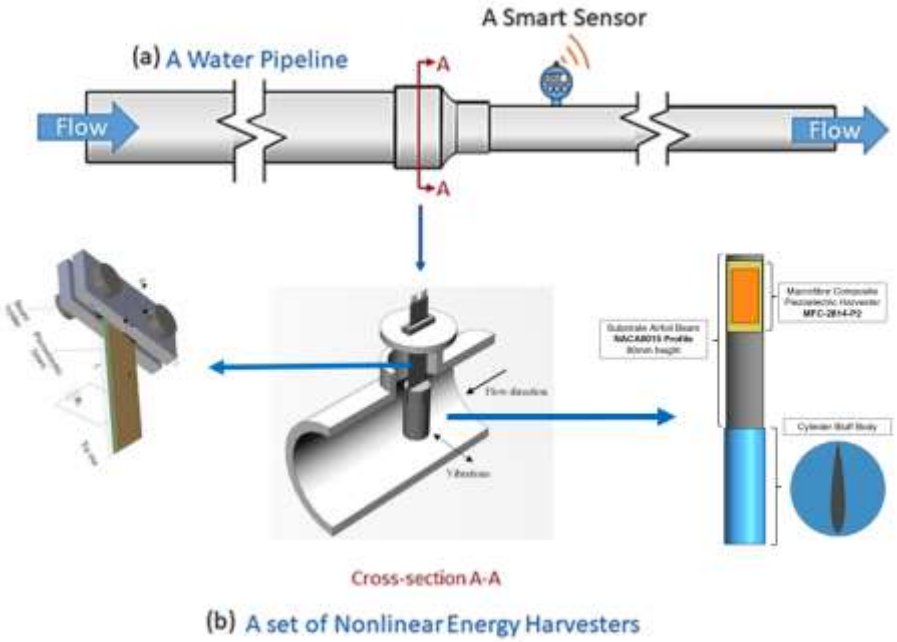

Figure 3 Schematic of energy harvesters deployed in a pipe

The harvester is mounted on low friction bearing inside of a pipeline circular array and then subjected to different flow conditions from the inlet. A bluff body is attached to the bottom of a cantilevered beam that causes flow separation that leads to random vibrations inside the pipeline. A piezoelectric macrofibre composite is attached to the substrate beam to harvest kinetic energy into electrical energy. The methodology flowchart (overview) is given in the following Figure 4.

- **Fluid-Structure Interaction (FSI) Analysis:** The structure of the energy harvester will be interacting with the flow stream of water that causes the piezoelectric composite to vibrate due to induced vortex-induced vibration. A generalized Multiphysics coupling model will be developed using computational fluid dynamics (CFD) numerical analysis.
- **Solving the Nonlinear Structural Mechanics Model:** The system of

partial/integral differential equations is to be discretized using a so-called DQM-FDM-based reduced-order modeling process (ROM). The ROM is then to be solved and used for the simulations of the harvester's nonlinear structural responses. The outcomes of the numerical model are to be compared with the results obtained from computational tools including ANSYS.

- **Design Optimization of Energy Harvester:** Optimum design parameters of the harvester will be investigated at this phase of the project. The shape and size of the bluff body are also affecting harvesting efficiency.
- **Setting up the Experimental Platform:** The energy harvester array will be manufactured and tested under the lab-scale water monitoring system in the Department of Mechanical and Industrial Engineering at Qatar University. The team is to set up the experimental platform to evaluate the harvester in a controlled, real-time environment.

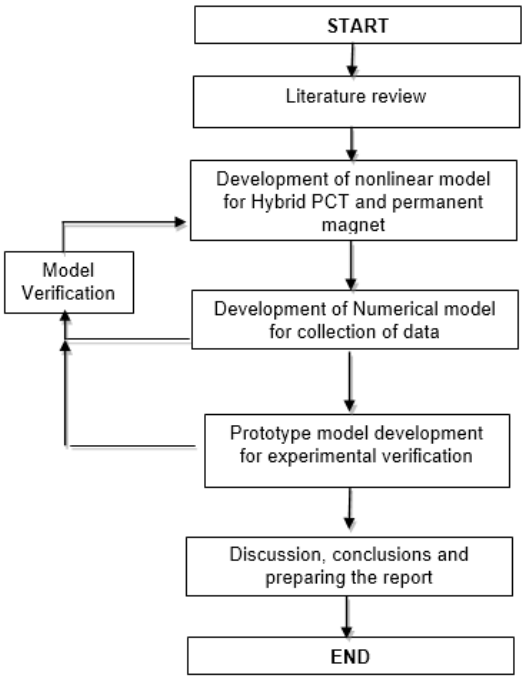

Figure 4 Flowchart showing an overview of the research methodology

1.5 Thesis Outline

The remainder of this thesis is organized as follows. Chapter 2 outlines the literature review and gaps in the research for a vortex-induced vibration-based hybrid energy harvester. Chapter 3 discusses the analytical modeling and equations for a single degree of freedom to multiple degrees of freedom model with state-space equations. Chapter 4 outlines the numerical analysis and solver used to predict the performance output of the hybrid energy harvester. Chapter 5 presents the computational modelling using computational fluid dynamics and finite element analysis software. Chapter 6 presents the findings of the experiments and the verification of the analytical models for frequency tuning and synchronization. Conclusions for the work are drawn in Chapter 7, with some recommendations for future work.

CHAPTER 2: LITERATURE REVIEW

With the growing maturity in efficient devices and energy harvesting mechanisms, the advances in self-sustaining powered devices have the potential to improve the sustainability of energy use and service life. Flow-induced vibration is one of the many clean and renewable ways of powering small devices by converting ambient vibration energy into electrical energy. Self-sustaining energy harvesters that can power such devices are important for autonomous monitoring and improving the service life without reliance on batteries [22]. The process of energy harvesting is especially useful in areas where access to a surplus power input is not readily available and can instead be collected from renewable ambient sources and utilized for process monitoring purposes. Real-time monitoring of information requires an integrated system of sensors, wireless communication routers, and a power supply to relay the information effectively [23,24]. This requires well-optimized and efficient components and a smart decision-making system. Powering up microelectromechanical systems (MEMS) in such systems often requires energy to power the sensors, storage, and communication devices [25]. Renewable and sustainable electricity sources can be considered an alternative power source to batteries as it overcomes logistic challenges and lifespan degradation [26].

The main methods for vibratory energy harvesting in fluid flow come from piezoelectricity, electromagnetism, and electrostatic generators [12,18,27,28]. Piezoelectric energy harvesting (PEH) has received an extensive amount of research and development over the last decades due to its versatility in converting kinetic energy into electric power and storing it in batteries or capacitors[29]. Previous work has provided useful insights into the well-optimized design of piezoelectric energy harvesting as well as the driving mechanisms behind it [30]. More recent work has

shown the potential of realizing self-sustaining piezoelectric energy harvesters for wireless transmission devices with power storage by adding an IGBT H-Bridge and a bi-directional buck-boost converter [31]. The addition of a tip mass (i.e., cylindrical bluff-body) adds a design parameter that can tune the resonance frequency and maximize power output by increasing the cantilever deflection from vortex-induced vibrations (VIV) [32,33]. Although PEH work in liquid media has been limited in comparison to that done in the air, the advancements in piezoelectric materials, mechanisms, and analytical models have helped improve the conversion of vibratory energy to electrical energy [34,35]. The generated voltage output through turbulent flow would be sufficient to power small electronics [36]. This is because harvesting energy from fluid flow gives rise to periodic oscillations found in "von Karman's" vortex street where it was suggested that conversion efficiency increases with decreasing harvester size due to the oscillation frequency [37–39].

The addition of bluff bodies helps generate vortices as the fluid separates from the boundary layer and coalesces into concentrated regions behind the body. The time-varying non-uniform pressure distribution causes inline and transverse vibration where the inline shedding frequency is approximately twice the transverse shedding frequency; however, the amplitude of the transverse shedding force is roughly 10 times that of the inline shedding force [40]. This corresponds with the work done by Vandiver and Jong (1987) [41] who initially proposed the quadratic relationship between the inline and transverse motion. Circular bluff bodies experience vortex-induced vibrations (VIV) and their response has been studied extensively in the literature [42–45]. Norberg (2003) [46] presented review data of the lift coefficients from VIV for stationary circular cylinders of varying diameters. Also, Blevins (2009) [47] developed non-linear VIV models based on experimental data of elastically supported cylinders in

water flow. More recently, Konstantinidis et al. (2020) [48] presented the dynamic response of flow of an inline excitation for low Reynolds number flow regimes and proposed a new model which includes the inviscid inertial, a quasi-steady drag and an inline fluid force. The response of the amplitude of a cylindrical bluff body increases greatly under synchronization or within the 'lock-in' region when the vortex shedding frequency matches the structural frequency for a stationary cylinder [21,49]. Williamson and Govardhan (2008) [50] outlined parameters for design optimizations of VIV energy harvesters in synchronization such as the vortex shedding modes at various reduced velocities and the critical mass. Additionally, lower mass-ratio systems can have a broader synchronization, and velocities for vortex modes can overlap. The large displacements on an elastically mounted submerged cylinder are advantageous for piezoelectric energy harvesters (PEH) that utilize this phenomenon [51]. This behavior introduces design parameters for energy harvesting by fluid flow as the synchronization region maximizes the harvested power. Galloping-based vibrations can also be found for non-circular geometries and have been shown to generate more power compared to pure VIV at higher Reynolds numbers [32,33]. Mehmood et al. (2013) [52] proposed a numerical model that coupled the motion of the cylinder with the fluid loads and highlighted the difference in responses for pre-synchronous, synchronous, and post-synchronous regimes at low Reynolds numbers. A piezoelectric energy harvester performs best for an optimized value of load resistance. A piezoelectric shunt-effect self-limits the amplitude of the cylinder vibratory oscillations in resonance through increased electromechanical damping [53,54].

Furthermore, work done on upright piezoelectric energy harvesters has also provided derived theoretical expressions and experimental results that lay the groundwork for multiple array orientations and structural design [13]. Recently, more

work has emerged from flow-induced vibrations (FIV) of other cross-sectional geometries and forced vibration modes. FIV is the generalized term that denotes oscillations as a result of a flowing fluid, of which vortex-induced vibration, galloping, and buffeting can be categorized [18,56,57]. Aramendia et al. [58,59] have also shown that geometric differences and optimization parameters can influence the performance of a piezoelectric energy harvester such that a U-shaped one performs better than a circular bluff body. Abdelkefi et al. [33] looked at the performance of piezoelectric energy harvesters with square, triangular, and D-shaped bluff bodies in galloping-based vibrations in the air, which highlighted the importance of electromechanical coupling on a system to extract the maximum amount of harvested power. Akaydin et al. [60] also demonstrated the importance of the coupling of aerodynamic, electrical, and mechanical interactions that play a significant impact on the power output, damping, and electrical resistance. Sun et al. [32] also investigated the effects of vortex-induced vibrations and galloping at lower velocities of water flow through Van der Pol models and Quasi-Steady models, respectively. The experimental work also outlined that galloping energy harvested is superior to VIV and that a larger lift force leads to larger oscillation amplitudes and harvested power. They also demonstrated an experimental setup with an open channel which showed that cylindrical bluff-bodies perform better at lower velocities due to VIV but do not perform as well as triangular prisms at higher velocities due to the additional galloping effects.

Work on combined flow-induced vibration energy harvesters has also emerged in the research field. Also, the addition of an electromagnetic oscillator placed outside of the beam working in conjunction with a piezoelectric harvester beam has the potential to further increase the power output of the system by up to 30% [61–63]. The application of piezoelectric harvesters can be extended to be modeled with sea waves

using wave models [64,65]. Also, Zhao et al. [13] proposed a combined hybrid system where the oscillations of vortex-induced vibration could harvest energy through piezoelectric strain and electromagnetic induction. Zhang et al. [66] also demonstrated that the use of magnetic forces on broadband energy harvesting through VIV can increase the level of harvester power by 29% and increase the synchronization region by 138%.

In this design, a compact form factor hybrid energy harvester can collect power from a fluid stream through a piezoelectric material and electromagnetic oscillator. The long-term goal would be to use the harvester in a system as part of a self-sustaining diagnostic and data collection system. Also, a proposed design of a nonlinear model of vortex-induced vibration-based piezoelectric-electromagnetic hybrid energy harvester system with dual mass configuration for broadband applications is proposed and optimized. Outside of the synchronization region, the amplitude of the VIV-based energy harvesters declines and negatively impacts the efficiency of power extraction. The addition of another energy harvesting mechanism and a secondary system can improve performance and be suitable for the broadband response of variable flow velocities. Jianan et. al. [67] investigated design parameters that can increase voltage output in electromagnetic energy harvesting (EEH) systems experiencing nonlinear wing flutter. Also, an alternative two-part winding scheme enhanced the voltage output for low-frequency applications. Hybrid energy harvester systems in VIV motion have been shown to efficiently harvest energy and increase the power output when synchronized (i.e., $f_{vortex} = f_{structure}$). Lai et al. [14] demonstrated that the addition of a dielectric system is superior to galloping-based and traditional VIV piezoelectric energy harvesters (VIVPEH). Zhao et al. [13] initially proposed a PE hybrid energy harvester by suspending a horizontal beam with a piezoelectric transducer that is

elastically connected to an electromagnetic system inside of a submerged cylinder experiencing VIV. The work demonstrated that maximum power output and efficiency from a hybrid PE system was greater than traditional piezoelectric or electromagnetic energy harvesters, and more power can be harvested from the electromagnetic than from the piezoelectric system. Hafizh et al. [61] investigated the bluff body optimization parameters for resonant vibration under fluid flow for a hybrid piezoelectric-electromagnetic system. The proposed hybrid harvester departs from previous work by utilizing a vertical harvester with an internal electromagnetic compact geometry that is fully submerged in water under the influence of VIV. Like hybrid energy harvesters, the dual mass configuration can also increase the power extraction and be tuned for variable flow velocities. Ideally, the addition of a secondary system can enhance the harvestable power where the response will coincide with the primary system. However, a dual-mass system can be less effective than a single-mass system when parasitic loss and electromechanical parameters are not considered. Tang and Zuo [68] performed a theoretical study on a dual-mass system and showed that with harmonic and base-excitation forces it can harvest more energy than a single degree-of-freedom system. Nishi [69] investigated the power extraction from a dual-mass system by modeling forces on the primary system submerged in water with a wake oscillator model. Xu-Xu et al. [70] expanded the aforementioned work by including VIV force coefficients and investigated optimized dual mass and stiffness relationships for maximizing energy harvesting efficiency.

Vortex-induced vibration (VIV) is one of the widely adopted methods of VEH, where periodic oscillations generated by vortex shedding provide the vibration excitation to the VEH [41]. Flow-induced vibrations can be classified into different modes such as fluttering, buffeting, and galloping [18,56,71]. The addition of a bluff

body allows for energy harvesting through vortex-induced vibration of a fluid medium which can further increase the energy harvester performance through a piezoelectric patch [20]. The response of VIV has been shown to output large structural deformations during 'synchronization' or in the 'lock-in region' when the structural natural frequency matches the vortex shedding frequency [42,44,45,48,72]. Williamson & Govardhan [50] outlined parameters for VIV harvesters by taking advantage of synchronization and vortex shedding modes. Norberg [46] provided data on VIV response in the literature for various Reynolds numbers and dimensions. Blevins [47] proposed mathematical models for the cylindrical bluff body response under the influence of VIV and demonstrated a robust agreement with experimental results. Synchronization during VIV energy harvesting relies on the vortex-formation and vortex-shedding pattern. Tuning the energy harvester to the vortex formation can further increase the energy harvesting performance [51]. The natural vibration characteristics of submerged plates in air and water can be accurately predicted according to the literature [73]. The response of vortex wake modes can be principally classified as 2S (single vortices), 2P (vortex pairs), and P+S (combination) mode regimes under synchronization [50]. The influence of boundary conditions can also change the vortex-shedding pattern. When an elastically-mounted cylinder is placed near a wall at a critical distance, vortex-shedding is suppressed by mixing counter-rotating boundary layer vortex to a single S or P vortex shedding pattern [74]. Vortex-shedding near the plane boundary does not change the synchronization range but can significantly reduce the vibration amplitude [75].

Linear vibration energy harvesters operate close to the structure's natural frequency, called the resonance frequency, where the deformation is the largest. The adoption of VIV vibration piezoelectric energy harvesting (VIVPEH) enhances energy

harvesting by attaching piezoelectric beams to bluff bodies [21]. The main drawback of this approach is that the resonance is narrow-banded and will not perform well if the excitation frequency drifts for any reason. Broadband energy harvesting applications are usually implemented to capture a broader range of harvestable frequencies with additional design parameters. Additionally, nonlinear vibration energy harvesters exploit vibration in the nonlinear regime to broaden the bandwidth so that the harvester is more responsive to random vibrations and is more robust [37,76]. Ibrahim et al. [16] investigated the broadband properties of piezoelectric beams by introducing nonlinear magnetic forces. Hybrid energy harvesters are made up of multiple systems suitable for broadband applications as each system can be tuned for a different range of frequencies. Challa et al. [15] highlighted that adding an electromagnetic system to a piezoelectric energy harvester improved the power output by 30%. Also, Zhao et al. [13] proposed a piezoelectric-electromagnetic energy harvester excited by VIV that outputs more energy than traditional PEH. More recently, Hafizh et al. [61] proposed an alternative design of a piezoelectric-electromagnetic energy harvester with bluff-body parameter optimizations. The Author's previous work expanded to include dual-mass configuration to increase the voltage output of piezoelectric-electromagnetic hybrid energy harvesters (PEHEH) and saw a performance increase of up to 52% [77]. Additional enhancement parameters by tuning the secondary system to the inline frequency of oscillation saw an improvement of 21-52% in cascade systems. The proposed models provided an electromagnetic oscillator system's theoretical and analytical framework.

The advantages of hybrid energy harvesting can combine different systems to further enhance energy harvesting performance. In this thesis, a hybrid piezoelectric-electromagnetic energy harvester excited by fluid flow is proposed and deals with the

energy module implemented in smart sensors. VEH captures kinetic energy from the ambient surroundings and converts it into electrical energy to power wireless sensors and transmitters. An analysis is done by considering the nonlinear vibration characteristics of the oscillation, and the subsequent mathematical model is used to find the output voltage. Magnets are also added to the harvester to enhance the performance and efficiency of electromagnetic energy harvesting. Research results have shown the adoption of PEMHEH for VIV applications with the electromagnetic system placed on the outside of the bluff body in an external orientation [13,78–80]. This is because electromagnet coils are rarely miniaturized for energy harvesting purposes since the external space helps increase the conversion efficiency through more coil windings and magnet size [15,81]. To the best of our knowledge, an internal electromagnetic energy harvester arrangement where an oscillating electromagnetic system is placed inside the bluff body has not yet been adopted. Considering that the effects of vortex-induced vibration can be utilized in pipeline systems, internal electromagnetic energy harvesters can open new opportunities in energy harvesting compared to conventional PZT energy harvesters. Therefore, this research proposes a compact form-factor hybrid piezoelectric-electromagnetic energy harvesting with synchronization tuning in different boundary applications. The performance is then compared with energy harvesters in the literature to demonstrate that the proposed energy harvester can satisfy the operating power requirements of smart sensors.

CHAPTER 3: ANALYTICAL MODELLING

In this chapter, the analytical modelling of the proposed piezoelectric-electromagnetic hybrid energy harvester (PEHEH) submerged in a moving fluid is explored. A schematic for the design of the proposed harvester is attached in Figure 5. The analytical model follows the methodological progression for a single mass harvester typically found in the literature [63,82,83]. Afterward, a dual-bluff harvester was explored to improve the performance output by taking advantage of both lift and drag coefficients in transverse and in-line oscillations. Transverse oscillations refer to the lift force effect that causes deformation perpendicular to the flow of water. Conversely, in-line oscillations refer to the drag force effect that causes deformation parallel to the direction of the flow of water. Finally, analytical modeling of magnetic coupling with nonlinear bandwidth enhancement properties were explored for tandem arrangements.

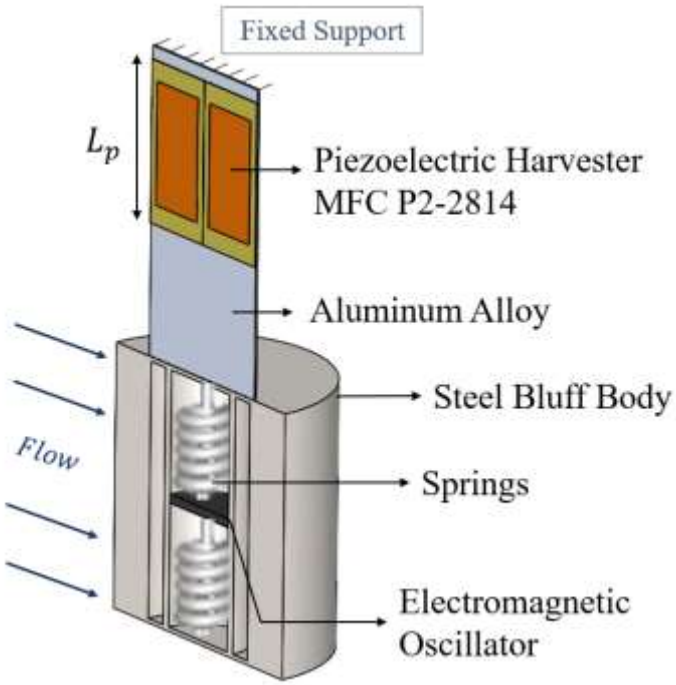

Figure 5 Schematic of proposed PEHEH submerged in moving fluid.

The harvester in Figure 5 is made up of MFC-P2 patches attached to the top of an aluminum beam. MFC-P2 utilizes the d31 effect of the piezoelectric effect designed for energy harvesting from bending motions with low impedance. The bluff body, which is used to enhance the VIV oscillations is made of steel with a hollow spacing. The electromagnetic oscillator is attached inside of the cylindrical body with coiled wires and two springs attached above and below it. The PEHEH excited by VIV oscillates the bluff body in both the transverse and inline direction with the fluid flow. The electromagnetic system oscillates vertically that is elastically coupled to the bluff body motions. A cross-sectional figure of the proposed hybrid energy harvester is shown in Figure 6.

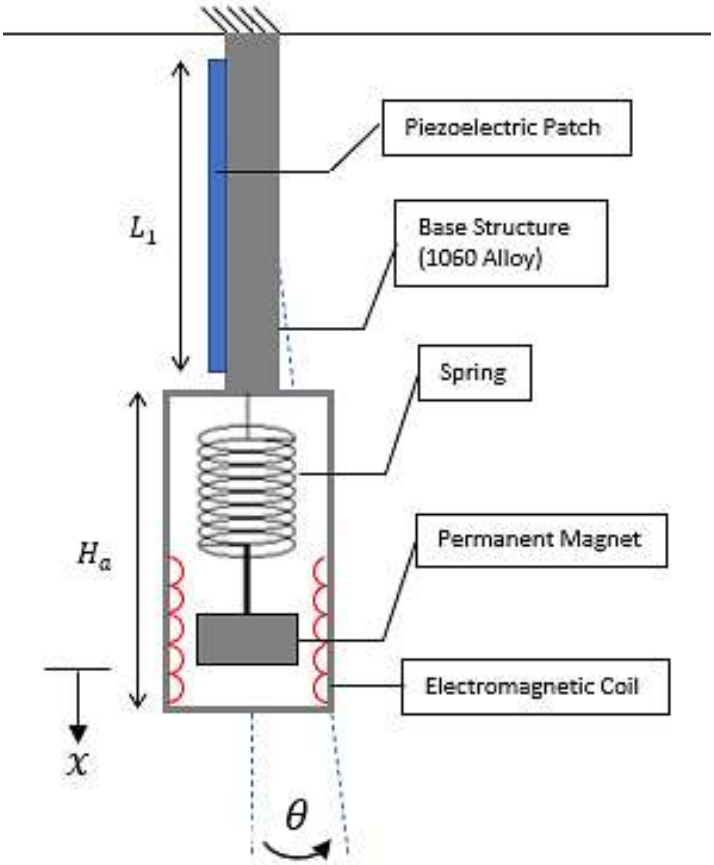

Figure 6 Electromagnetically coupled piezoelectric energy harvester system

The method by which energy will be harvested within this model through two methods; firstly, through the strain experienced by a piezoelectric patch; secondly, through the movement of a permanent magnet along a coil through a magnetic field. After that, the two motions will be combined into a single equation and then studied. The combined system will first be examined through a traditional energy harvester model using a tip mass and then expanded to include the force of water modeled as a sinusoidal function input. The main goal of the current work is to increase the energy harvested from a hybrid energy harvester from vortex-induced vibration as shown in Fig. 1. The harvester comprises a piezoelectric patch that is mounted on a cantilevered beam with an electromagnetic oscillator inside a bluff-body at the free tip. The

generation of 'Von Karman' vortex shedding around a cylindrical bluff body creates the transverse vibrations normal to the direction of the flow of water. The parameters used for the system are defined in Table 1 and additional nomenclature is in Table 2. The material for the beam and oscillator used in this study is 1060 aluminum alloy since it provides good elastic properties to induce internal strain on the piezoelectric patch. The piezoelectric patch selected was Polypropylene (PP) for having a high fatigue resistance to aqueous solutions [24] and being inert for drinking water applications [25].

3.1 Piezoelectric System

3.1.1 Single Degree of Freedom Equation

Piezoelectric patches can produce electricity when it is exposed to a force that deflects their shape. There are many orientations, types, and shapes of piezoelectric patches that can be used to maximize the energy harvesting properties within this study. The patch will be attached to a sufficiently elastic metal (i.e., 1060 Alloy) that can elastically bend when subjected to external forces.

For a SDOF system with one beam and one bluff body, the transverse oscillations modeled as a mass-spring-damper system follows Newton's Second Law which can be expressed per unit time as shown in Eq.1. The addition of a piezoelectric patch is modeled as a damper in the system with a load resistance R as shown in Figure 7.

$$M\ddot{x} + C\dot{x} + Kx + \Theta V_p = F(t) \qquad \text{Eq. 1}$$

Here $\ddot{x}$, $\dot{x}$ and x are the acceleration, velocity, and displacement of the cylinder, respectively. C is the equivalent system damping, Θ is the electromechanical coupling coefficient and V_p is the voltage produced when the piezoelectric patch experiences

mechanical strain. It is assumed that a low mass-damping assumption is made that there is no restoring force for an unrestricted displacement in a volume of water ($K_a = 0$). F is the force of the fluid acting on the bluff body because of VIV.

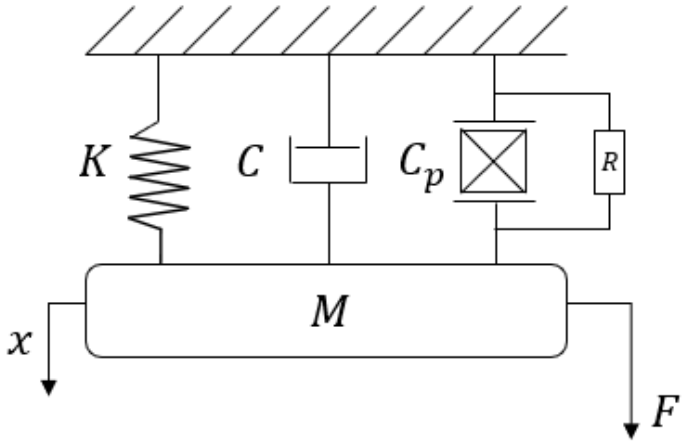

Figure 7 SDOF Hybrid Energy Harvester System Equivalent Bluff Body Mechanical System

Under forced vibrations within the synchronization region (where the oscillation frequency matches the natural frequency in the transverse motion), the oscillation can be modeled as a harmonic motion with a fixed amplitude and frequency. It can be approximated as the product of the two-parameter self-excitation model with in-phase and out-of-phase forces represented as an inertia-force coefficient (C_{mv}) and velocity-force coupling coefficient (C_{dv}) [47]:

$$F_{f,transverse} = \frac{\rho U^2 DL(C_{mv}\sin(2\pi f_v t) + C_{dv}\cos(2\pi f_v t))}{2} \quad \text{Eq. 2}$$

Where f_v is the vortex shedding frequency, D is the diameter of the bluff body, ρ_f the density of the moving fluid, ω_s, m the mass of the system, A_y the amplitude and C_D the coefficient of drag. To simplify the equation of motion, the resistance of the

piezoelectric sensor on the attached substrate beam can be modeled as a force ($F_{piezo} = \Theta V$), thereby summarizing the total force exciting the body as:

$$F(t) = F_{f,i} - F_{p,i} \quad \text{Eq. 3}$$

3.1.2 U-Beam Dual Mass System

The Cascaded U-Beam System is a dual-bluff body design in which both bluff bodies undergo transverse oscillations due to vortex shedding as a result of the lift coefficient. In this orientation, the system treats the main bluff body and the secondary bluff body as semi-dependent motions, is shown in Figure 8. This dependency arises because of the spacing in the beam to where the secondary system is attached to. That is to say that it can be simplified as two single-degree-of-freedom systems with natural frequencies that can be tuned to the same vortex shedding frequency. The Dual-Mass System follows the same parameters as a single-mass system described in Eq. (4) – (5). As the values of l_x get bigger and l_y get smaller, the secondary beam becomes stiffer – hence the relationship $k_\delta \propto l_x, l_y$ for the range of $0 < l_x < l$:

$$M_1\ddot{x_1} + c_1\dot{x_1} + k_1x_1 + k_3(x_1 + x_2) = F_1 \quad \text{Eq. 4}$$

$$M_2\ddot{x_2} + c_2\dot{x_2} + k_2x_2 + k_3(x_1 + x_2) = F_2 \quad \text{Eq. 5}$$

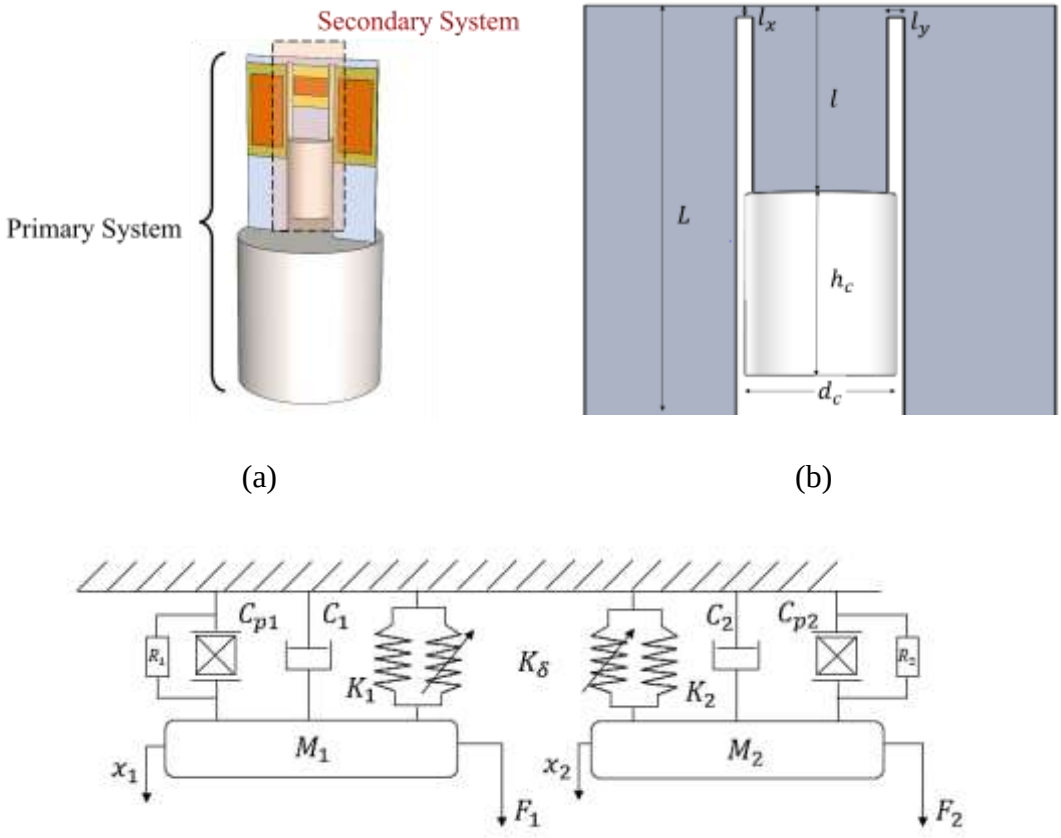

Figure 8 Cascade U-Beam System; (a) 3D Model; (b) Parameter Modeling; (c) Equivalent Bluff-Body Mechanical System

3.1.3 Cascaded Dual-Mass System

A cascaded dual-mass system is a dual-bluff body design that consists of two bluff bodies; a primary system and a secondary system that undergo vortex shedding as a result of the flow of water. In a cascaded system, the primary system is tuned to the vortex-shedding frequency of transverse oscillations due to the lift coefficient. Conversely, the secondary system is tuned to the vortex shedding frequency of inline oscillations due to the drag coefficient. The other configurations have been abbreviated as either vertical or horizontal to denote the secondary L-shaped dual mass

configuration for simplicity. These different designs were proposed to study the optimal dual-mass design that can be optimized for both lift and drag coefficients. The behavior of the cascaded body system can be modeled like a tuned-mass damper system. Thus, the equivalent mechanical system and its equation of motion and the coupling coefficients can be summarized as the following:

$$M_1\ddot{x_1} + C_1\dot{x_1} + K_1x_1 + \Theta_1 V_{p1} - K_2(x_2 - x_1) - C_2(\dot{x_2} - \dot{x_1}) = F_1 \quad \text{Eq. 6}$$

$$M_2\ddot{x_2} + C_2(\dot{x_2} - \dot{x_1}) + K_2(x_2 - x_1) + \Theta_2 V_{p2} = F_2 \quad \text{Eq. 7}$$

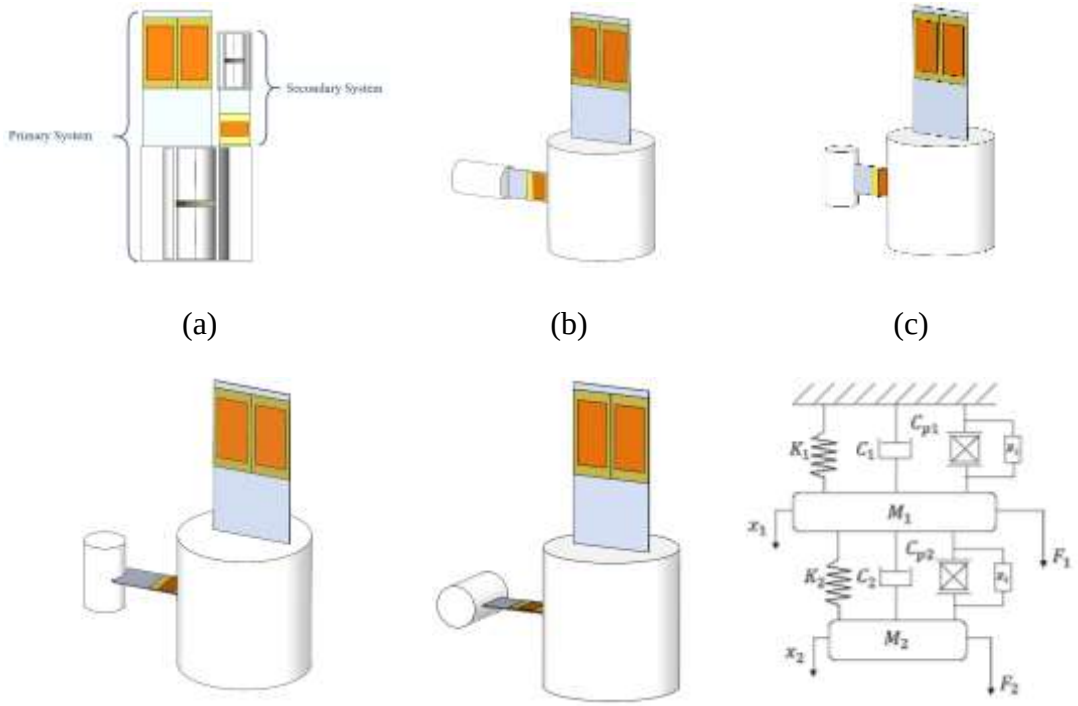

(a) (b) (c)

(d) (e) (f)

Figure 9 Cascade Body Systems; (a) Vertical Body (VB); (b) L-Vertical beam and horizontal bluff-body (LV-HB); (c) L-Vertical and Vertical Bluff-body (LV-VB); (d) L-horizontal beam and vertical bluff-body (LH-VB); (e) L-horizontal beam and Horizontal Bluff-Body (LH-HB) (f) Equivalent Bluff-Body Mechanical System

3.1.4 Magnetically Coupled System

The proposed design of the nonlinear vibration energy harvester is shown in Figure 10, which is submerged in water. The design specifications and parameters were expanded from work done by the author in creating a compact hybrid energy harvester [61]. An identical system is facing each other, and the magnetic field attached to both allows for the interaction. The entire system is made from 3D-printed thermoplastic which allows for increased versatility in manufacturing and decreases the overall mass. 15% carbon-fiber infused polylactic acid (PLA) was used as the substrate for flexibility (compared to conventional aluminum and steel substrates) with the composite blend adding rigidity to prevent plastic deformation during deformation. The bluff body is made from polyethylene terephthalate (PETG), which has good water properties and does not break down at higher temperatures.

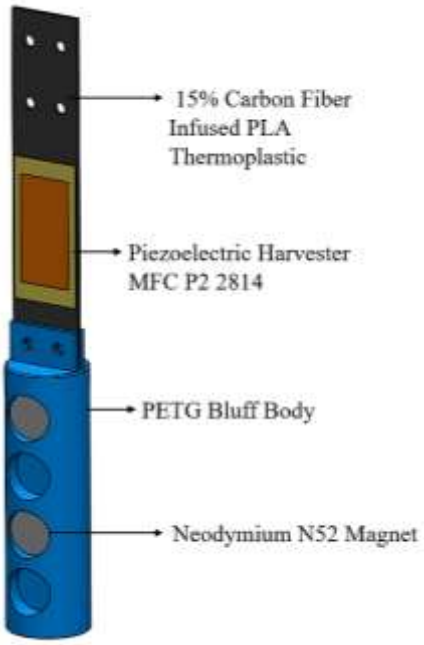

Figure 10 Schematic of a magnetically coupled tandem vibration energy harvester

VIV oscillations form behind the bluff body and cause the deflection of the

substrate which can be modeled in Figure 11 and derived in Equations (8) – (10) for a tandem magnetically coupled system. The voltage output of the system is calculated in Equations (11) and (12). Vibration-based kinetic energy was converted to electrical energy using a piezoelectric macro fiber composite from smart materials: MFC-2814-P2 [84].

$$M_1\ddot{x_1} + C_1\dot{x_1} + K_1x_1 + \Theta_1V_1 = F(t) \quad \text{Eq. 8}$$

$$M_2\ddot{x_2} + C_2\dot{x_2} + K_2x_2 + \Theta_2V_2 = F(t) \quad \text{Eq. 9}$$

$$F(t) = F_{Fluid}(t) \pm F_{magnet} - F_{Piezo}(t) \quad \text{Eq. 10}$$

$$V_1(t)/R + C^s\dot{V}_1(t) - \Theta_1\dot{x}(t) = 0 \quad \text{Eq. 11}$$

$$V_2(t)/R + C^s\dot{V}_2(t) - \Theta_2\dot{x}(t) = 0 \quad \text{Eq. 12}$$

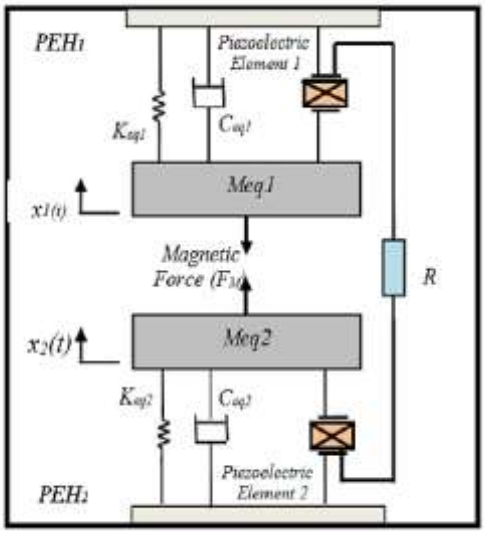

Figure 11 Equivalent Bluff Body Mechanical System of Two Magnetically Coupled Energy Harvesters [19]

Because the magnet can be either attractive or repulsive, both instances will be evaluated and compared [16]. In this study, F_{magnet} looks at only the repulsive forces

of the magnet on the energy harvesting. F_{Fluid} represents the transverse oscillations because of the bluff body [47]. F_{piezo} is the actuating effect caused by the accumulated charge on the piezoelectric patch [7]. Equation (13) represents the equations used to derive the forces. τ_0 is the permeability of the medium, m_1 and m_2 the moments of the magnetic dipoles and D_0 is the distance between magnetic tip mass and the fixed magnet.

$$F_{magnet} = 3\tau_0 m_1 m_2 / 2\pi [x_1(t) - x_2(t) + D_0]^4 \quad \text{Eq. 13}$$

3.2 Electromagnetic System

The concept of electromagnetic induction makes use of a varying magnetic field to produce a voltage across a conductor by changing the magnetic flux in magnetic field. This can be achieved by passing a magnet through a coil of wire. However, if the motion of said magnet only comes in one direction and remains stationary, the emf (electromotive force) will only be generated at that instant. Thus, it is important to continue to vary the magnetic field by either moving the coil or moving the magnet. The rapid change in motion of the magnet can be achieved by attaching a spring to the end of the magnet and allowing it to fall freely under gravity.

During induction, the current i is generated by the coil of wire, and the emf produced introduces a resistive force, which in turn introduces electromagnetic damping and slows down the motion of the magnet. The reaction force can be expressed in Eq. 14, while the equation of motion for the electromagnetic system is expressed in Eq. 16.

Therefore, the equation of motion to describe a vertical mass-spring motion (of

a mass m and spring stiffness k) that is suspended vertically and allowed to oscillate without any damping properties has the kinematics of simple harmonic motion that can be described using Newton's Second Law as:

$$\ddot{x} + \frac{k}{m}x \pm F_{magnet} = 0 \qquad \text{Eq. 14}$$

$$F_{magnet} = BIL_{coil} \qquad \text{Eq. 15}$$

$$\ddot{x} + \frac{k}{m}x + BIL_{coil} = 0 \qquad \text{Eq.16}$$

Where B is the flux density (strength of the magnetic field) measures in Teslas; I is the current measured in Amperes; L_{coil} is the length of the coil (conductor) measured in meters. From the equation above, the factors associated with the movement of the electromagnet system come from the properties of the mass (and its magnetic properties) and spring as well as the coil. Since the electromagnetic force can be attractive or repulsive, it is simplified to be a restoring force in this equation.

Adding another harvesting mechanism to the existing structure is an added contribution to implementing a hybrid energy harvester for hydrokinetic applications. It involves a spring attached to a permanent magnet mass within a coil of the movement of the harvesting structure causes spring oscillations. Soti et al. [28] summarized that the maximum average power does not significantly change for variations in coil length and coil radius. According to Faraday's Law of electromagnetic induction, an electromotive force (emf) is produced by the movement of a magnet within a coil of wire because of a change in magnetic flux. Also, the emf generated is directly proportional to the change in the flux, resulting in greater energy conversion because of the restoring oscillatory motions. Thus, the governing equation for induced emf of a disk-shaped magnet moving with a velocity v in a magnetic field B of a coil is expressed

as Eq. 17 [85]:

$$\varepsilon = \oint (\bar{v} \times \bar{B}) \cdot \bar{dl} \qquad \text{Eq. 17}$$

Once the electromagnetic coil is connected resistive load R_L, the induced current ($i = \varepsilon / R_L$) in the circuit opposes the motion of the magnet experiencing an opposing electromagnetic force because of the now present electromagnetic coupling. This reaction force acting on the magnet can be expressed in Eq.18 [29]:

$$F = \int i\, \bar{dl} \times \bar{B} \cdot \hat{z} \qquad \text{Eq. 18}$$

Eq.19 shows the expression for a single dipole magnetic moment μ, the approximated electromagnetic force for a coil with N number of turns and vertical height L_{coil} is the coil length looped around the bluff-body enclosure [29]:

$$F = \frac{\left(\frac{N}{L_{coil}} 2\pi a^2 \mu\right) v}{R_{coil}} \left[\frac{1}{[a^2 + h]^{\frac{3}{2}}} - \frac{1}{[a^2 + (h + L)^2]^{\frac{3}{2}}}\right]^2 F$$

$$= \int i\, \bar{dl} \times \bar{B} \cdot \hat{z} \qquad \text{Eq. 19}$$

If a is the internal radius of the electromagnetic coil, h is the distance from the center of the magnet to the height of the coil. The internal electrical resistance of the conduction coil $R_{coil} = \frac{4N(2\pi a)}{\sigma \pi D^2}$ with a wire conductivity σ. The added benefit of having the electromagnetic transduction mechanism mounted internally is to have the freedom

to retrofit the hybrid energy harvester and placed it in tandem or combined arrangement with multiple other devices like it. By shifting the resonance point of the electromagnetic harvester near the piezoelectric harvester, the behavior can be adjusted for a fixed water flow to maximize the harvestable energy output or to target a wider range of frequencies for a broadband energy harvesting application. Since the electromagnetic energy harvester is fixed inside the bluff body, there will be another degree of freedom for the coupled electromagnetic system that generates electricity through the vibration of the magnet. The equation of motion for such a system can be simply expressed by Eq. (20) where the deformation is based on the angular displacement and acceleration of the beam expressed as θ and $\dot{\theta}$, respectively:

$$\ddot{x} + \frac{k}{m}x - (L + x)\,\dot{\theta}^2 - gcos\theta + BIL_{coil} = 0 \qquad \text{Eq. 20}$$

Here, θ represents the deflection angle of the beam substrate deflecting with VIV and z is the extended length of the spring. Since the angular motion of the mass-spring system is restricted, the oscillation of the mass occurs in the vertical direction within the confined space of the bluff body. Alternatively, the use of two springs attached on each end of the magnetic mass ($k = k_1 + k_2$) can also enhance the amount of power harvested by forcing the magnet to oscillate close to the center of the coil where the magnetic flux is the densest. Alternatively, springs can replace by two magnets of opposite polarity to the center magnet and exhibit the characteristics of spring with a total stiffness of k. From Eq.8, x refers to the linear displacement of the mass from the static position on the spring, θ is angular displacement experienced by the beam expressed in Eq.1, B is the flux density and I is current within. Therefore, the voltage output from the electromagnetic oscillator can then be modeled as a function of

the electromagnetic induction (Eq. 9) and self-inductance L_{ind} as shown in Eq. (21):

$$V_{electromagnetic} = BL_{coil}\dot{x} - L_{ind}\dot{I} \quad \text{Eq. 21}$$

3.3 Combined Hybrid System

Once both systems have been combined, there needs to be a change to start generating electricity – strain in the case of piezoelectric patch or motion in the case of electromagnetic induction. To achieve this within a fluid-flowing pipe, turbulence must be generated such that the force of the fluid hitting the harvester as well as turbulence and wake formation because of interrupted flow can achieve the required motion and strain. In addition to this, by studying the harvester under resonance, the shape and resonant frequency can be seen for different scenarios of flow speed and harvester. The shape, size, and orientation of the electromagnetic oscillator are to be studied and varied to optimize and select the best one across different times or at resonant frequencies.

For a simple mass-spring system that is fixed at the top end of the spring, the mass can oscillate indefinitely for an undamped system. When introducing the water flow, the random vibration produced as a result of the fluid flow causes the harvester structure to move in an arc motion similar to a pendulum (despite the corresponding structure realistically exhibiting a random motion). Because of the randomness in the formation of turbulence and associated vibration, it is difficult to accurately map the output of the vibration over a while. Nevertheless, by using simulation tools, the movement of mode shapes can be studied and the output at given frequencies can be used to optimize the performance.

To mathematically model the electromagnetic spring system and bind the mass-

spring system to a linear motion and use the corresponding dynamics of the harvester structure to model the movement of the mass-spring system. For a specific angular displacement, the speed, and acceleration of the structure; can be correlated to the movement of the mass and spring in a linear motion. Since the mass-spring system is restricted to only moving linearly, the angular acceleration of the system equates to zero. Thus, if a friction factor[1] was included along the restricted movement, the summarized equation of motion for the electromagnetic coupled system is derived as Eq. (22) – Eq. (26):

$$\ddot{x} + \frac{k}{m}x - (l + x_0 + x)\,\dot{\theta}^2 - g\cos\theta + BIL_{coil} = 0 \quad \text{Eq. 22}$$

$$a_\theta = \ddot{\theta}(l + x_0 + x) + \frac{2}{m}\dot{x}\dot{\theta} = 0 \quad \text{Eq. 23}$$

$$F_{friction} = \mu N = \mu m a_\theta \quad \text{Eq. 24}$$

$$\ddot{x} + \frac{k}{m}x - (l + x_0 + x)\,\dot{\theta}^2 - g\cos\theta + \mu\left[\ddot{\theta}(l + x_0 + x) + \frac{2}{m}\dot{x}\dot{\theta}\right] + BIL_{coil} = 0 \quad \text{Eq. 25}$$

$$V_{ES} = BL_{coil}\dot{x} - L_{ind}\dot{I} \quad \text{Eq. 26}$$

3.3.1 Combined System modeling with Discretized Water Force

The harvester model is made up of a vertical piezoelectric beam with an attached tip mass that oscillates because of the water flow through the pipe with a speed defined as V_{water} and the corresponding force, F_L induced by the water on the cylinder. The

[1] The context of this study neglected the friction factor associated with the motion of the mass rubbing against the walls of the enclosure

turbulence caused by the bluff body results in transverse oscillations (vibrating perpendicular) to the flow of water. The vortex-induced vibration outputs the voltage for the piezoelectric element defined as $V(t)$. The proposed hydro-electromechanical model outlines the equation of motion for the harvester subjected to the incoming water flow submerged in a pipe and affects the lift coefficient, C_L evolution at the studied water speed as expressed in Eq. (27) – (31) for 1.24 m/s [26]:

$$a_2\ddot{\theta} + a_3\dot{\theta} + a_4\theta = a_1 T_{Hydro} \quad \text{Eq. 27}$$

$$a_2\ddot{\theta} + a_3\dot{\theta} + a_4\theta = a_1 T_{Hydro} \quad \text{Eq. 28}$$

$$a_3 = f + \frac{\alpha^2 \cdot a^2}{K_p \cdot K_{trans}} \approx 4.612 \times 10^{-3} \quad \text{Eq. 29}$$

$$a_4 = \frac{K \cdot a^2}{K_{trans}} \approx 0.01579 \quad \text{Eq. 30}$$

$$T_{hydro} \approx sin\omega t \quad \text{Eq. 31}$$

Here θ refers to the angular displacement of the deformed beam as shown in the input hydro-mechanical torque T_{hydro} modeled after the water flow represents a sinusoidal waveform and the evolution of the lift coefficient is modeled as a constant.

3.4 Natural Frequency Synchronization with Submerged Structures

For narrowband applications of vibration-based energy harvesting using an electromagnetic oscillator and a piezoelectric system, the ability to harvest at the natural frequency can enhance performance. The strain experienced by the MFC patch is converted into electrical charge whilst the magnet's motion creates an electrical current.

However, some assumptions were made to derive the natural frequency of bodies in a fluid medium because of the added mass effect in shifting the natural frequency. Since water will have an added hydrodynamic component, the effects of the added mass cannot be ignored:

$$(M + M_a)\ddot{x} + (C + C_a)\dot{x} + (K + K_a)x + \Theta V_p = F(t) \quad \text{Eq. 32}$$

The terms M_a, C_a, K_a denote the added mass, added stiffness, and added damping, respectively. Determining the natural frequency of a discrete system in the air can be represented as Eq. (33) – (35).

$$\omega_n = \sqrt{\frac{K}{M}} \quad \text{Eq. 33}$$

$$\omega_d = \omega_n\sqrt{1 - \zeta^2} \quad \text{Eq. 34}$$

$$\zeta = \frac{C}{2\sqrt{KM}} \quad \text{Eq. 35}$$

Where *K* is the equivalent stiffness of the system, *M* is the equivalent mass of the system, M_a is the equivalent added mass due to the hydrodynamic effect when the system is submerged in water and $f_{n,w}$ is the approximate natural frequency of the energy harvester when submerged in water. By assuming that the natural frequency of air is identical to that in a vacuum, the ratio between the two mediums can be approximated by the following Eq. (36):

$$\omega_{n,w} = \frac{\omega_n}{\sqrt{1 + \frac{M_a}{M}}} \quad \text{Eq. 16}$$

Figure 12 outlines the approximated natural frequency for different mediums at varying submergence depths. The equation with the effects of hydrodynamic fluid can be used to estimate the deviation in natural frequency caused by the new submerged medium. Additionally, the height of the submergence can affect the natural frequency. In a partially submerged harvester, the effects of added mass only influence the submerged section of the body up to the submergence length, L_s. Also, the derived ratios for submerged fluid medium use the damped natural frequency ω_d since the viscous effects of water add a damping property to the overall equation for experimental validation as shown in Eq. (37) – Eq. (39).

$$\frac{\omega_{n,w}^2}{\omega_n^2} = \left(1 + \frac{K_a}{K}\right)\left(1 + \frac{M_a}{M}\right)^{-1} \quad \text{Eq. 37}$$

$$\frac{\omega_{d,w}^2}{\omega_d^2} = \left(\frac{1 - \zeta_w^2}{1 - \zeta^2}\right)\left(1 + \frac{K_a}{K}\right)\left(1 + \frac{M_a}{M}\right)^{-1} \quad \text{Eq. 38}$$

$$\frac{\zeta_w}{\zeta} = \left(1 + \frac{C_a}{C}\right)^2\left(1 + \frac{K_w}{K}\right)^{-1}\left(1 + \frac{M_w}{M}\right)^{-1} \quad \text{Eq. 39}$$

To evaluate the energy harvesting performance and perform comparative analysis across multiple configurations, the root means square (RMS) analysis is adopted, as shown in Eq. 40. RMS voltage presents a unified way of amazing the continuously varying signals from both piezoelectric and electromagnetic systems.

$$v_{rms} = \sqrt{\frac{1}{t}\int_0^t v(t)^2 dt} \quad \text{Eq. 40}$$

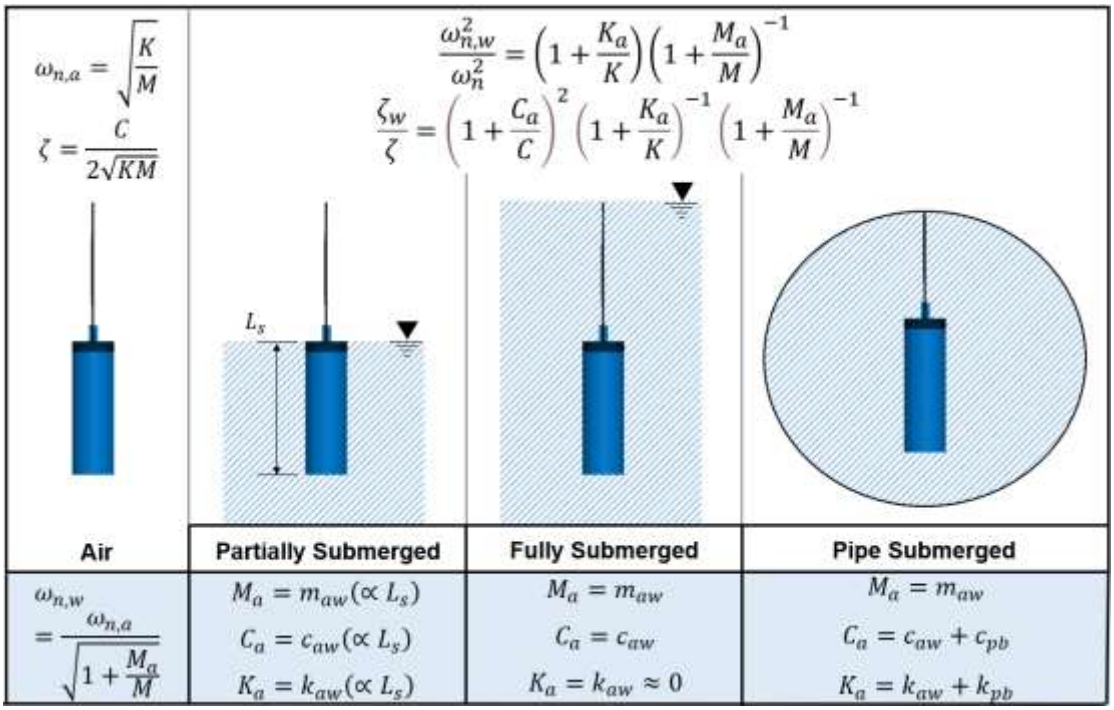

Figure 12 Natural frequency of discrete bodies in different submergence depths [62]

In an infinite-span boundary situation, the added stiffness of partially and fully submerged discrete bodies do not experience a stiffness to constant displacement ($K_a \approx 0$) [86]. In a pipe-submerged scenario, the boundary conditions play a significant role in the added stiffness and damping as there is a visible fluid-structure interaction from the oscillations of the bluff body with the pipe wall. Therefore, the newly added stiffness and damping consist of a new parameter with subscript 'pb' to highlight the effects of the pipe-boundary, which diminish with a widening boundary condition.

Han and Xu [87] investigated this hydrodynamic influence of a submerged structure with the natural frequency and showed good convergence between numerical and experimental results. Alternatively, the investigation performed by Rodriquez et al. [86] highlighted additional damping parameters for consideration to include cases where the apparent added mass effect of submerged structures can be negative.

Moreover, the effects of flowing water on a structure and the observed phenomenon of VIV can be enhanced with synchronization. The synchronization region leads to large amplitude displacements because the shedding frequency of vortices matches that of the submerged structural natural frequency ($f_{n,w} = f_v$). In the literature, the Strouhal number for a fixed cylinder is often approximated as 0.2 and remains nearly constant up to Re $= 10^4$ [42,44]. However, comprehensive empirical work has provided more accurate values based on this thesis's Reynolds number shown in Eq. . The Strouhal number can be expressed as Eq. (41) – (42) [46,88]:

$$St = \frac{f_s D}{U} \qquad \text{Eq. 41}$$

$$St = 0.1853 + 0.0261 \cdot \left[-0.9 \cdot \left(log\left(\frac{Re}{1.6 \times 10^3}\right)\right)\right], \qquad \text{Eq. 42}$$

$$Re = 1.6 \times 10^3 - 1.5 \times 10^5$$

The harvester can be tuned to the water velocity and shedding frequency to increase the amount of energy extracted. Designing around the large amplitudes can be advantageous for both the piezoelectric and electromagnetic systems in extracting energy from the flow. The lock-in range at which this phenomenon is observed can be represented by the dimensionless reduced velocity, $5 < U^*_{sync} < 7$ based on the Strouhal number is shown as Eq. (43) [88,89]:

$$U^*_{sync} = \frac{1}{St} \qquad \text{Eq. 43}$$

A summary of the optimization parameters is presented in Figure 13, where the natural frequency of the harvester in water can be represented by its relationship to the natural frequency in air. Moreover, the onset velocity for oscillations in the transverse

and inline directions has been highlighted as well as the relationship between the vortex shedding frequency.

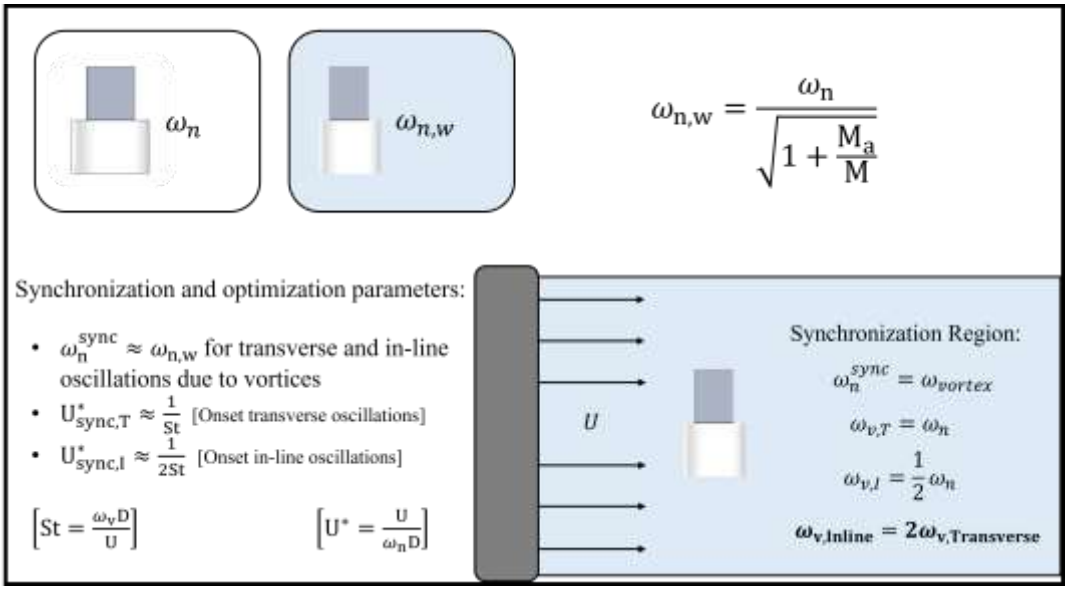

Figure 13 Summarized Parameter Optimization for Submerged Energy Harvester in VIV [77]

CHAPTER 4: NUMERICAL ANALYSIS

4.1 Setup

To visualize the movement of the combined system as well as estimate the voltage output, MATLAB software was used to get the values done through a series of simulations. Since the combined system consisted of non-linear differential equations, the overall solution was solved using Ordinary Differential Equations (ODE) functions with initial conditions. The output of the ODE was then used to model the voltage output of the combined piezoelectric energy harvester in the time and frequency domain. The use of Laplace transforms also explored due to their innate simplicity in converting differential equations into easily solved polynomial equations; however, the manipulation of values to measure the voltage in the time and frequency domain for both systems was not as easily realized. Some optimizations were also done to solve the equation and improve the efficiency of the calculations, primarily through the ode function. Initially, ode45 was used in solving non-stiff ODEs with medium accuracy; however, transitioning from 3 parameters (for single systems of mass-spring or piezoelectric) to a higher degree of 6 parameters greatly extended the computation time with questionable accuracy. Hence, the conversion to a stiff solver (ode15s) greatly improved the computation time to solve the equations with acceptable accuracy [2].

The solver ode15s was used because the output results exhibited a degree of stiffness and whereas ode45 did not yield efficient computing time. Based on the work by Aramendia et al. [26], the calculations were performed similarly where a harmonic apparent force of the water was used to excite the bluff body of the hybrid harvester. The initial displacement, velocity, and acceleration were at zero, and the only parameter

[2] Ode15s is advised to be used when ode45 solver fails, is inefficient or suspected to be stiff [1]

affecting the change was the force of the water hitting the electromagnet oscillator. The parameters used in running the calculations are highlighted in Table 1. For this model, the cylinder bluff body was used and will continue to be used as a reference shape in subsequent studies.

Table 1 Modeled Parameters of Hybrid Energy Harvester

Symbol	**Description**	**Value**	**Units**
ρ_{piezo}	Piezoelectric Material density	5319	kg/m^3
$\rho_{cylinder}$	Circular cylinder bluff-body density	2700	kg/m^3
ρ_{fluid}	Fluid density	999.06	kg/m^3
D	Cylinder bluff body diameter	0.04512	m
L_1	Length of layer	0.038	m
L	Length of the beam	0.13	m
b	Width of the beam	0.05	m
h	The thickness of the beam	0.006	m
H_a	Cylinder height	0.06	m
J_{wt}	Cylinder inertia moment	4.069×10^{-7}	$kg \cdot m^2$
C_L	Lift coefficient evolution	1	–

4.2 Results

The initial conditions assigned to the ODEs were that the initial displacement, velocity, and acceleration were at zero and the only parameter affecting the change was the force of the water disturbing the bluff-body in flow stream. Figure 14 highlights the results of the simulation performed on MATLAB.

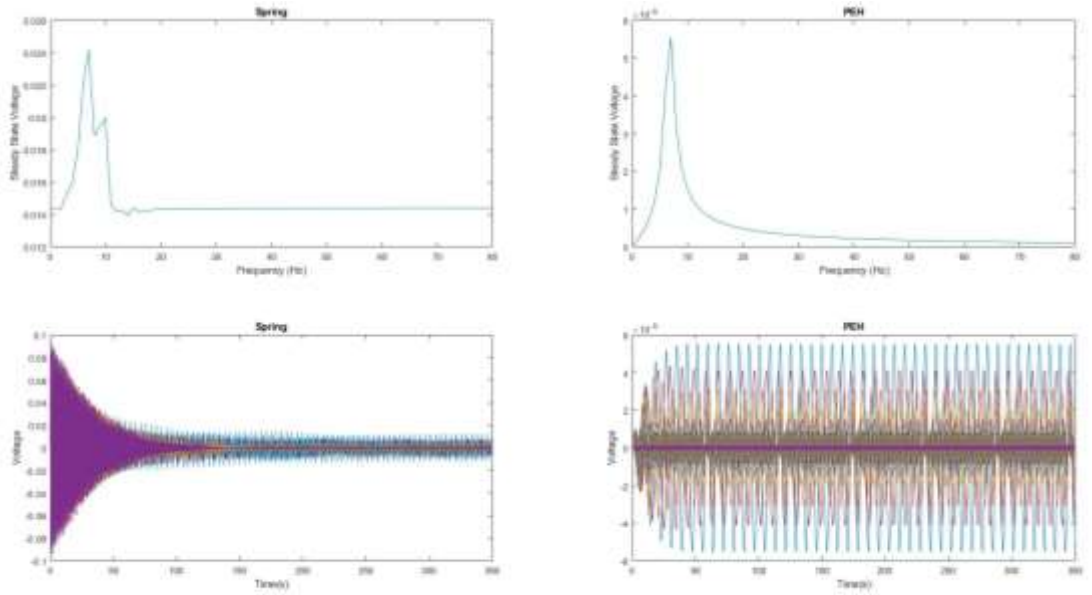

Figure 14 MATLAB Run Simulations for Energy Harvesting System; (a) Voltage output in the frequency domain for spring system; (b) Voltage output in the frequency domain for PEH system; (c) Voltage output in the time domain for spring system; (d) Voltage output in the time domain.

In Figure 14 there appears a distinct peak for the PEH system in the frequency domain, which correlates to its resonant point. In addition to that, the time-domain plot shows that the influence of the water flow provides sufficient vibration to generate vibration which reaches a steady state. In contrast, the spring system experiences its resonant frequency in the voltage-frequency plot and shows another peak that correlates

to the resonant frequency of the PEH system. Also, the time domain of the spring system shows that it starts unsteadily and reaches a steady state.

The time responses of frequencies up to 80Hz were calculated, and the maximum amplitude at each frequency was used. Figure 15 shows the maximum harvestable voltage from the coupled system at a steady state by analyzing the last half of the time response to remove transient effects. Figure 15(a) displays the electromagnetic oscillator system, while Figure 15 (b) displays the harvested voltage through the piezoelectric energy harvester (PEH) system. This approach has been able to sow the response in the frequency domain to approximate the resonant frequency.

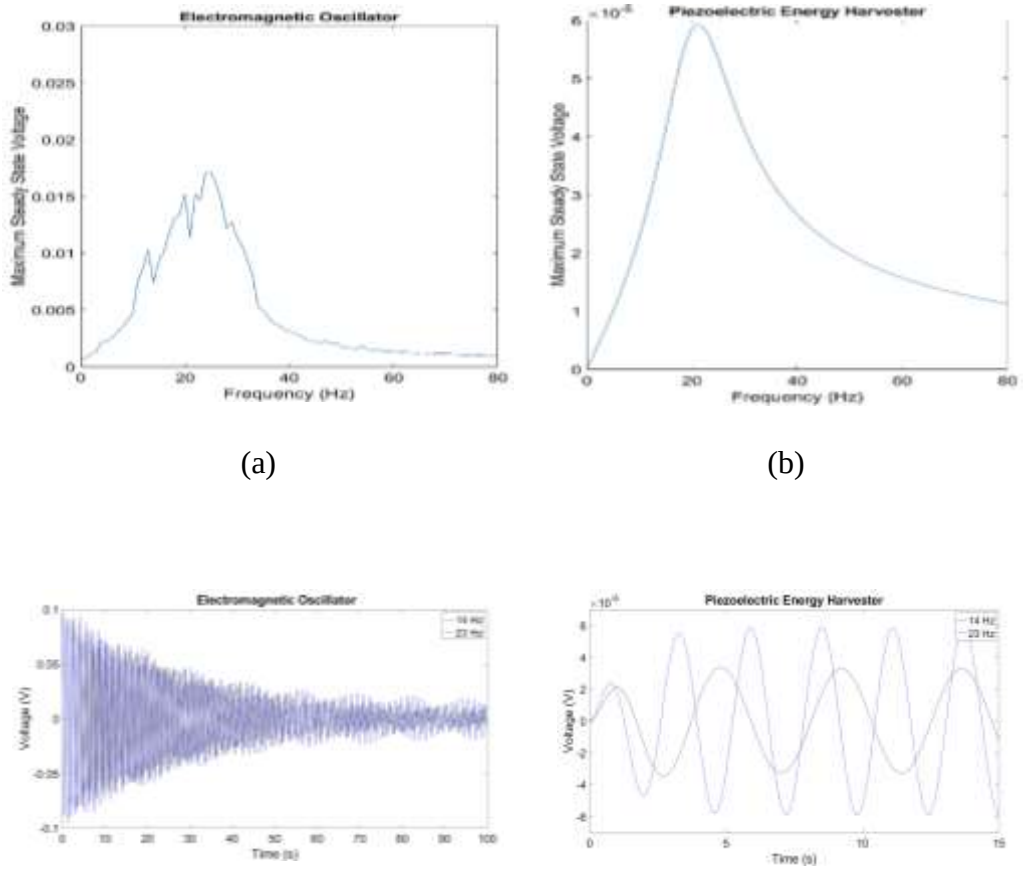

Figure 15 MATLAB Simulations for Energy Harvesting System; (a) Maximum steady state voltage output in the frequency domain for the electromagnetic system; (b)

Maximum steady state voltage output in the frequency domain for PEH system; (c) Electromagnetic oscillator time response; (d) PEH time response [61]

Based on the results of the MATLAB simulation, a distinct peak in Figure 15 (b) is seen for the PEH system in the frequency domain, which correlates to the natural frequency of the structure that it is attached. In contrast, Figure 15 (a) shows two peaks that are measurable in the electromagnetic coupled system; the first peak corresponds to the resonant point of the electromagnetic oscillator, and the second for the coupled PEH system. The natural frequency for the electromagnetic oscillator is 14Hz, whilst the PEH is 23Hz; their time response is shown in Figure 15 (c) and Figure 15 (d), respectively. By tuning the hybrid energy harvest into having the two resonant points closer to each other, the system can operate near the natural frequency of both systems. Working near the structural resonance of the system is advantageous in maximizing the total power harvested from the surrounding flow of water. If both systems were tuned to resonate near the oscillation frequency because of vortex-induced vibration, then the hybrid energy harvester can continue to harvest maximum amounts of voltage through the large displacements. Tuning is an additional parameter that can be introduced to increase the efficiency of the energy harvesting process for the coupled system.

CHAPTER 5: COMPUTATIONAL ANALYSIS

5.1 Computational Fluid Dynamics

5.1.1 Computational Domain Setup

The computational fluid dynamics (CFD) setup in modeling the energy harvester inside of a pipe carrying water used a two-dimensional approach to visualize

the effects of the vortex shedding and wake generation across the different bluff bodies. The computational domain was made up of a velocity inlet of water (temperature: 288.15K) of varying velocities with a width of 20D non-slip boundary walls - where D is the diameter of the circular bluff body - from the center of the circular bluff body and 10D upstream. The downstream length of the domain was modeled in 30D for wake generation and to visualize the vortex shedding over 20 seconds. The computational domain and mesh distribution around the cylindrical bluff body is shown in Figure 16.

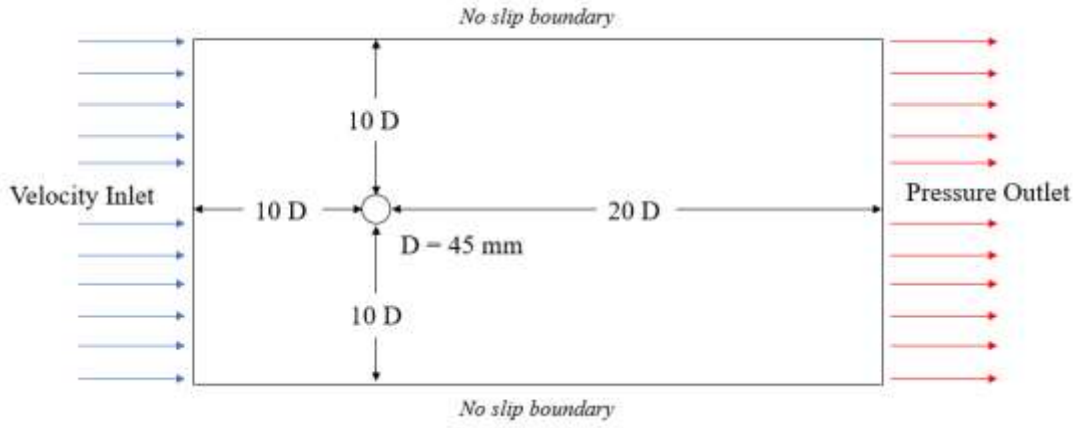

Figure 16 Computational domain setup and parameters [77]

A computational fluid dynamics simulation was conducted to model the viscous and inertial forces of the fluid interaction. The simulation was performed as a two-dimensional approach to visualize the effects of VIV. The computational domain and setup are shown in Figure 16. ANSYS Fluent v.2020R2 CFD software with second-order spatial discretization and implicit transient formulation settings was developed. The computational domain is important in simulating the correct vortex and structure response. Good agreement with literature is seen for domains similar to 40D x 10D sufficiently large enough to avoid disturbance caused by boundary conditions [59,90,91]. In flows around a cylinder, a 5% blockage ratio is sufficient to diminish the impact of boundary conditions in the flow field [92]. The bluff body was placed at a 10

D distance from the inlet where *D* is the diameter, and the outlet is 30*D* downstream. The size was selected to ensure that vortex interaction with the walls would not occur and to provide adequate space behind the bluff body for sufficient vortex generation. The average static reference pressure at the outlet boundary was set at 0 Pa. A no-slip boundary was applied to the top and bottom wall positioned 10D from either side of the cylinder center and for the cylinder wall such that fluid stream velocity is achieved in the far region. The Reynolds number used in the modeling surpassed the laminar and transition boundaries so the $k-\omega$ SST turbulence model was used to solve the inner region of the boundary layer [93]. The flow simulation was resolved using a SIMPLE Algorithm and a 2nd order $k-\omega$ transport equation [94]. The distance between the cylinder wall and the first node, y^+ was kept below unity so that there is adequate resolution of grids near the cylinder in simulation and was maintained throughout all simulations. The mesh generated in the domain was adjusted to be fine around the wall boundary. A time step of 0.002s with 15 iterations per time step over 20 seconds was implemented to adequately show the vortex shedding.

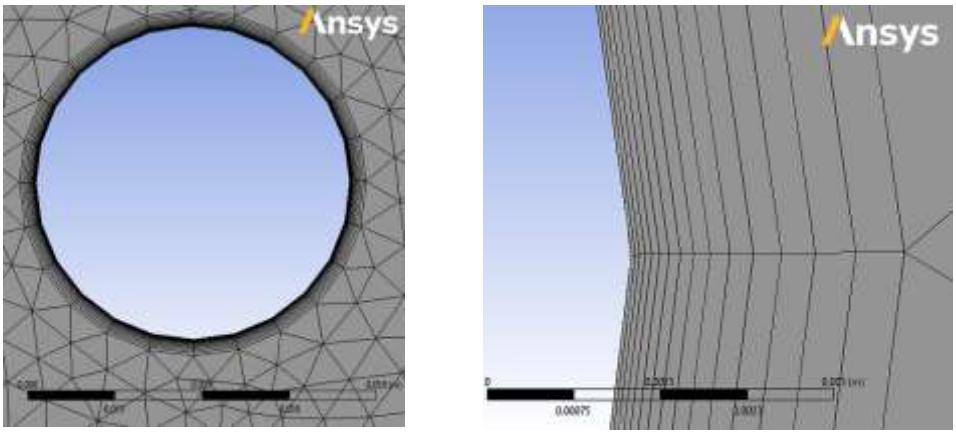

(a) (b)

Figure 17 Preliminary mesh generation; (a) View of mesh around the circular body with triangular generation; (b) Close-up of inflated mesh around the body

ANSYS Fluent v. 2020 R2 [30] solver was used in setting up the CFD simulation, Figure 17 with approximately 93,000 elements of triangular mesh with 15 inflated layers around the bluff body. The unsteady state flow was solved using Unsteady Reynolds-Averaged Navier Stokes (URANS) equations. Since Reynold's number ($Re = \rho vD/\mu$) exceeds the transition interval, a turbulent transport model K-omega SST viscous model developed by Menter [31] was used. The time interval of 0.002s and 15 iterations per time step was selected because it provided adequate values to see the vortex shedding and convergence. A semi-implicit method for pressure-linked equations (SIMPLE) algorithm-based solver was used which balances out the computational expense and convergence rates. Second-order upwind spatial discretization and second-order implicit transient formulation settings were also applied to this simulation. The mesh was refined to keep y^+ around the body below 1. A mesh independence study has been performed to verify the selected mesh resolution using by using the Richardson extrapolation method [32] summarized in Table 2 by comparing the results of the drag coefficient from three different meshes with varying element sizes: 63500 (coarse), 127000 (medium), and 254000 (fine).

Table 2 Mesh independence study

Re	**Mesh Definition**			**Richardson Extrapolation**		
	Coarse	**Medium**	**Fine**	**Re**	**p**	**R**
10000	0.94	1.02	1.18	1.23	0.98	1.97

The results from the fine mesh were found to be accurate and converges well with drag coefficient values in literature varying between 1.1 – 1.2 [46,95]. Therefore, the subsequent mesh techniques were used for further simulations. To achieve a wall

y+ value below unity, an inflation mesh with a first layer thickness of 1E-6 m was applied with a maximum 100 layers and 1.2 growth rate. An edge sizing was applied around the circumference of the circle with a 210-division count. The mesh element size was a minimum of 1.3E-3 m with a minimum element quality of 0.17 and an average quality of 0.94. The fine mesh generation is shown in Figure 18.

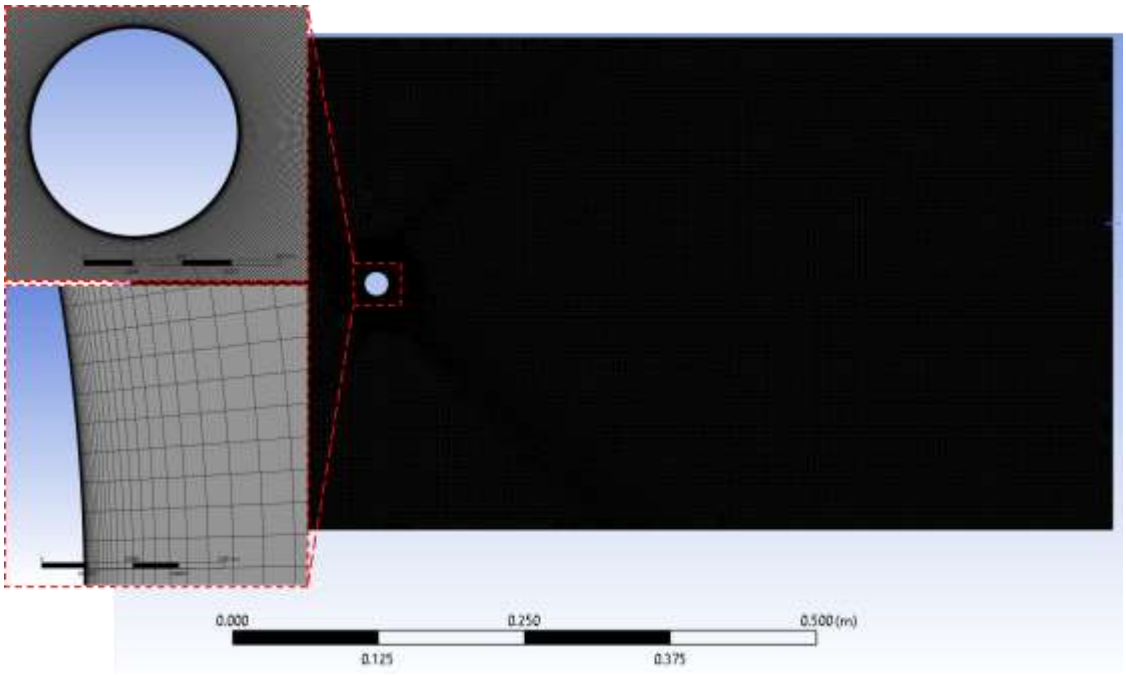

Figure 18 Bluff body vortex-induced vibration mesh generation

A good agreement between the numerical solution and experiments from the literature is summarized in Table 3 by comparing the lift (C_L) and drag (C_D) coefficients [46].

Table 3 Comparison between simulation and experimental results at Re=12,000

Measurement	**Simulation**	**Experiments**
$C_{D,mean}$	1.19	1.10-1.20 [46,95]

A uniform velocity of 0.197 m/s at the inlet corresponding to Re=10,000 (for density=$999kg/m^3$, dynamic viscosity=$0.001137kg/m \cdot s$, diameter=$0.058m$) was used. Computational fluid dynamics simulations were performed for the single and dual-mass configurations. The results of the force coefficients were extracted for the finite element simulations. Mesh sensitivity tests were conducted for varying grid resolutions at cylinder walls and near-field grids and compared to values obtained in the literature. The results are shown for the Reynolds number Re=10,000 in Table 4.

Table 4 Result and Comparison of Fixed Cylinder at Re=10,000

	Norberg [46]	Dong and Karniadakis [95]	Nguyen and Nguyen [96]	Jin et al. [97]	Present Work
Method	Experimental	DNS − B2	DES	SST K − ω	SST K − ω
CL_RMS	0.41	0.50	0.36	0.67	0.42
St	0.20	0.21	0.20	0.20	0.23

The results presented in Table 4 show robust agreement with those found in the literature while being less computationally expensive than the alternatives Direct Numerical Solution and Detached Eddy Simulation [90]. Once the initial setup and verification were done for a single-mass configuration, the simulation was extended to dual-mass configurations [69,70]. The addition of a thin substrate in the U-beam Cascade configuration suppresses the formation of vortices as seen in Figure 19 in comparison to the vertical cascade which only has a disturbed flow in front of the bluff body.

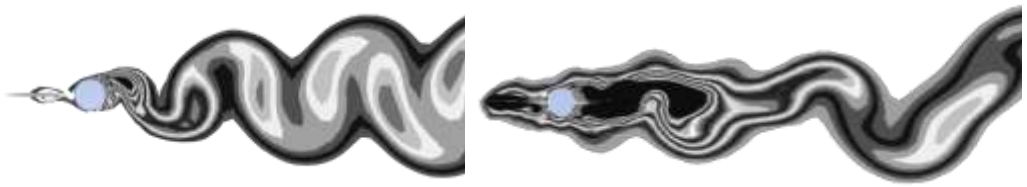

(a) (b)

Figure 19 Instantaneous vorticity formation; (a) VB Cascade; (b) U-Beam Cascade

5.1.2 CFD results with Hybrid Energy Harvester

The bluff body serves a vital role in wake generation and creating turbulence behind the structure that increases power output from the hybrid harvester. Figure 20 shows the observed displaced amplitude modeled for the hybrid energy harvester when subjected to incoming external flow at 1.24 m/s. Vortices created behind a body are responsible for the vibration of the system where vortex shedding leads to transverse oscillations on the structure relative to the water flow. The cylinder was first tested at a speed of 1.24 m/s and lower speeds as well to observe the formation of vortices behind the bluff body shown in Figure 20. The resultant displacement of the beam is transverse deformation to the water flow since the directional stiffness is less in this direction than the direction parallel (in-line deformation) to the water flow.

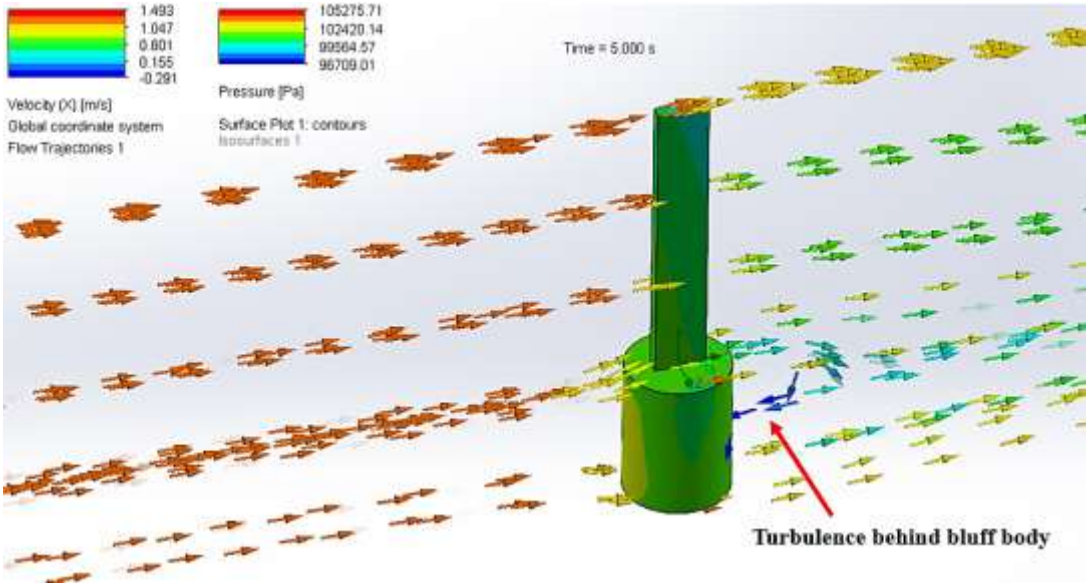

Figure 20 Isometric view of the simulation study on the cylinder bluff body configuration for energy harvesting with Fluid Simulation at 1.24m/s

Since the shape selection affects the formation and intensity of the turbulence disrupting the flow behind the bluff body, a computational fluid dynamics (CFD) study was performed to illustrate the formation of these vortices. Figure 21 shows the motion of the vorticity generated behind the bluff body with surface areas similar to surface areas of 1600 ± 1 mm^2. The finite element comparison of these bluff bodies is discussed in the following section.

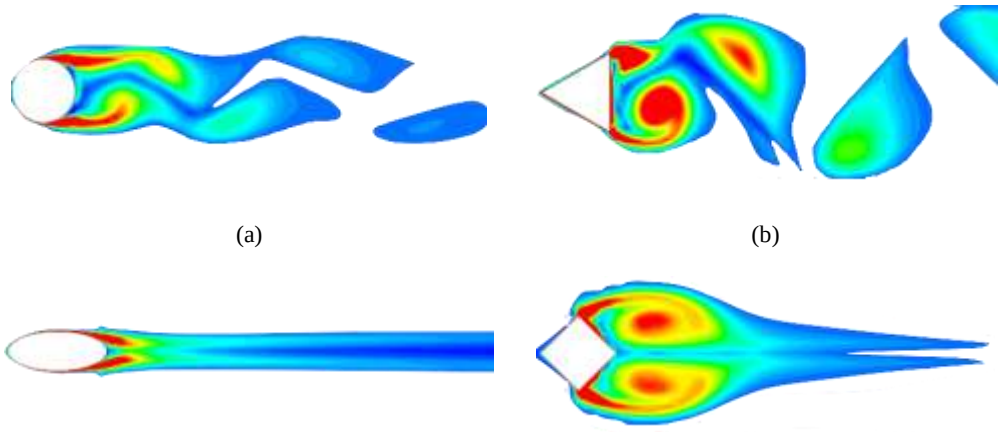

(a) (b)

(c) (d)

Figure 21 Measurable vorticity generated by bluff body; (a) circle; (b) triangle; (c) ellipse; (d) quadrilateral [61]

The addition of sharp edges generated more visible vorticity behind the shape; with the vorticity behind the triangle bluff body generating the most visible turbulence. In contrast, the smooth and thin shape of the ellipse does not generate as much turbulence. The maximum steady-state turbulence kinetic energy (TKE) of the four shapes is summarized in Figure 22. While the triangular and quadrilateral bluff bodies have been shown to generate a significant amount of turbulence, the higher selected speeds could have introduced the effects of galloping past a certain onset water velocity which has been demonstrated in the literature to aid in energy harvesting.

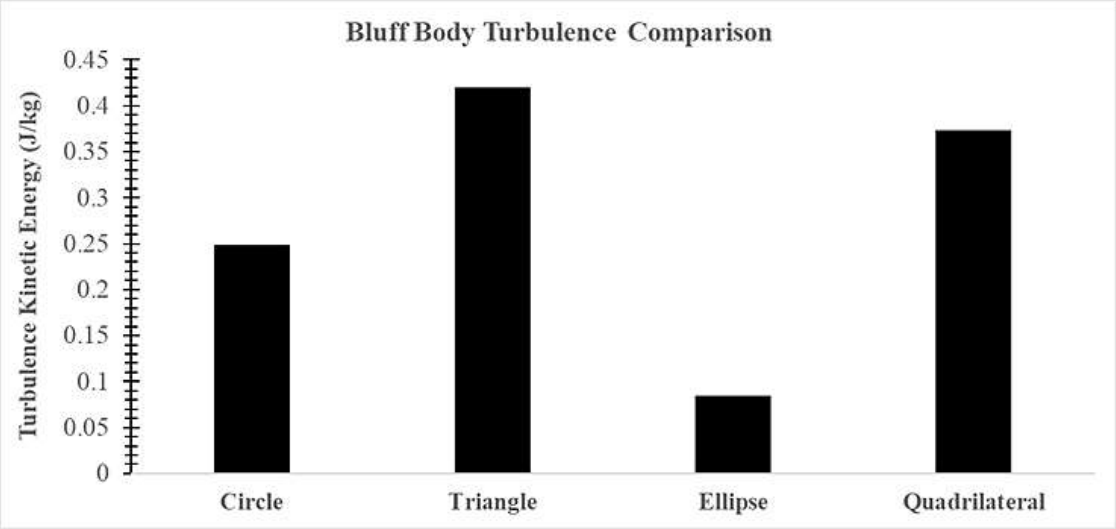

Figure 22 Maximum steady state turbulence kinetic energy created behind bluff body comparison [61]comptes

To investigate the effects of the turbulence formation only and avoid the potential effects of pipe wall interaction harvester, the parameters of the study used are

for external flow over the energy harvester bodies. This parameter study focused on shape performance and did not have any attached piezoelectric materials or bluff body cavities. All iterations of the study were done with the shapes in Figure 22 having the same mass of $304.87 \pm 0.02g$ to ensure that the dynamic study and frequency study is also not affected by the differences in mass. The nonlinear dynamic study used the pressure effects of the fluid interaction with the structure and displays the flow effect on the structural quantities of stress, strain, and deformation during a 1s period. Also, the frequency study looks at the different mode shapes and corresponding resonant frequencies of each configuration. The resultant vibration in each first mode and the corresponding maximum, average, and resultant amplitude can be compared. The simulated resonant frequency for the cylinder bluff body and modeled with the water flow is 25Hz which represents an 8.70% deviation from the derived MATLAB numerical solution. The cylindrical bluff body was selected as a control comparison since it does not have any changes in its geometry.

5.2 Finite Element Analysis

5.2.1 Bluff Body Investigation

After the MATLAB study, the next natural transition to extend the study into the coupled energy harvesting mechanism is through a 3D model and simulation study. Thus, the work was modeled on SolidWorks which has a powerful modeling and finite element analysis tool. SolidWorks was primarily used here to validate the findings of MATLAB simulation and to visualize the motion generated when subjected to a random input of water force; rather than a harmonic one. Figure 23 shows the main transverse mode shape that is observed for the energy harvester performed on

SOLIDWORKS with a fixed-free boundary condition.

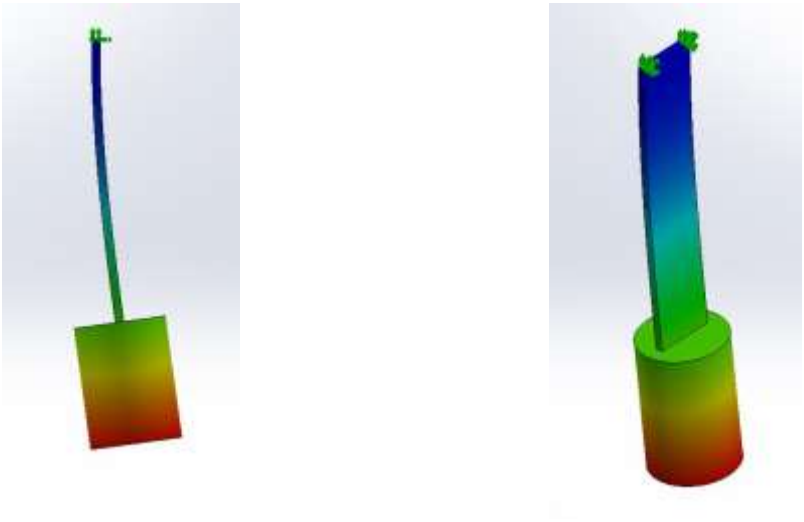

(a) (b)

Figure 23 SolidWorks Model of Energy Harvester During Resonance with Expected Deflection; (a) Front View; (b) Isometric View

After the preliminary studies are completed, the next step of the study was to see which bluff-body shape performs best as an underwater energy harvester. The bluff body serves a significant role in wake generation and causes turbulence within the structure that causes the piezoelectric strain to occur as well as the mass-spring system to oscillate; both of which harvest electricity from the vibration. According to Aramendia et. al., [59] the best output of water flow was seen for a speed of 1.24m/s after testing for other water speeds; thus, this speed was primarily used for the Solidworks model.

By investigating different parameters of the bluff body shape, an external flow simulation was constructed and run. The results of the flow simulation were then exported into simulation models where there were structural studies on the beam to which the piezoelectric patch was attached. The static study looked at the overall

deflection of the harvester after being subjected to the water flow. Next, the non-linear dynamic study used the pressure difference caused by the water flow on the structure ('flow effects') to visualize the change in the stress, strain, and deflection over time; from this, the maximum and average values of the parameters were noted down and compared between each configuration. The frequency study looks at the mode shapes and resonant frequencies of each configuration; from there the probe function was able to measure the resultant amplitudes and compare the maximum, average, and sum values of each node.

The four main bluff-body shapes evaluated are shown in Figure 24. During the Simulation study, there may have been different parameters changed such as the angle of corners[3], angle of rotation along the axis[4] , and size ratios[5] – all parameters maintained the same mass properties. In these orientations, the shape comparison used will have the cylinder bluff body as the control shape since it does not have parameters that can be changed and can be assumed to have the same performance throughout.

[3] An equilateral triangle was converted into an isosceles triangle by varying the angle at the tip while changing the base sizes to meet the mass change uniformity in an attempt to see the difference in the 'angle of attack' or how sharp the edges were when water came into contact with the shape

[4] In the case of the ellipse, triangle and square shaped bases, their axis was rotated along the center to study the effects of object bluntness/sharpness on the performance of the energy harvester as well as attempting to create pressure difference to either side of the water flow

[5] The height and width ratios of the ellipse was varied to investigate the best performance by varying the bluntness/sharpness of the contact with the water flow

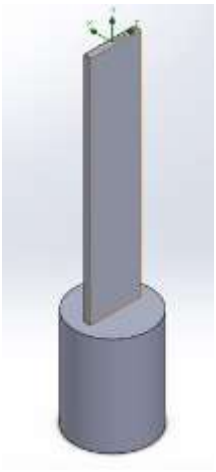

(a)

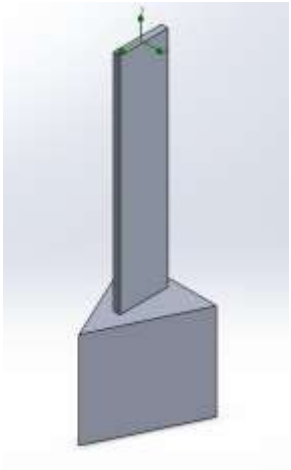

(b)

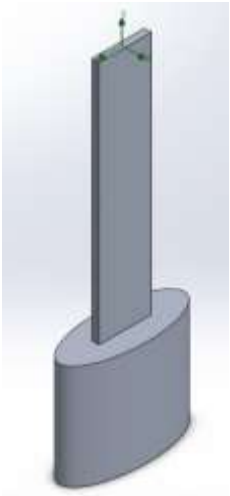

(c)

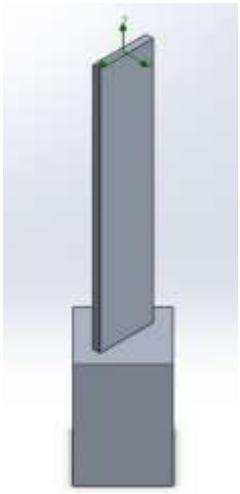

(d)

Figure 24 Bluff Body Shapes Investigated; (a) Cylinder; (b) Triangular; (c) Ellipse; (d) square/cuboid

A preliminary study was conducted before beginning the design modeling and finite element analysis simulations. This was primarily done to provide uniformity during the simulation setups such that extraneous settings and variables do not negatively impact the findings and analysis. The following list below contains the preliminary tests

conducted and their summarized findings:

- The shapes were tested for various flow speeds to ensure that the same mode shape was produced at the ranges between 0.2 to 1.3 m/s of water velocity. All the tested velocities show the same first mode shape where the resultant amplitude transverse oscillation to the water flow.
- During the study of the triangle-shaped bluff-body, the beam placement on the bluff-body at the bonded layer was varied. Specifically, the distance from the front edge of the beam (where the piezoelectric patch would be attached to) to the front tip distance of the triangle was varied between 5mm to 23mm - values were chosen so that the beam was not placed outside of the boundary of the triangle. After running the frequency study on these various positions, the results showed that there wasn't a lot of change from the resultant and maximum resultant amplitude with the highest deviance at 0.5%, which can be attributed to the computing accuracy and error margins.
- The angle of rotation (of the beam and margin) is was varied from 0° to 90° for shapes that have both a sharp edge and a wide surface (i.e. triangle and square) as shown in Figure 25. The results from the frequency study show that the rotation has no visible change to both the maximum and average resultant amplitude.

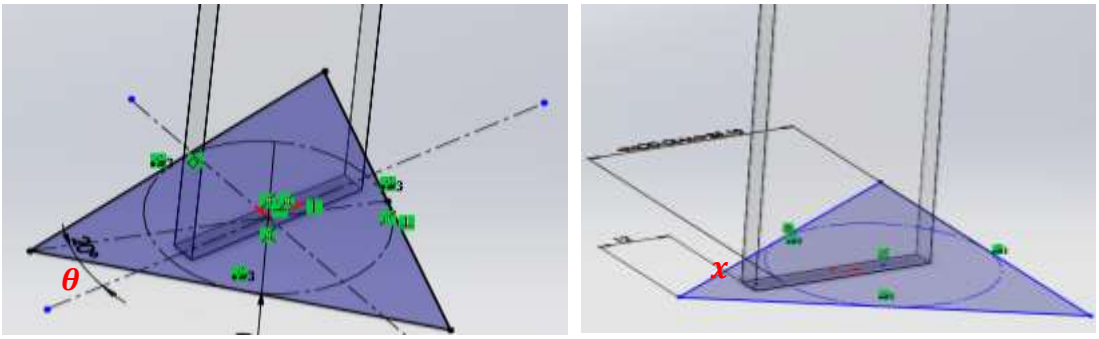

(a) (b)

Figure 25 Preliminary Study of Varying Variables; (a) Changing the Angle of Rotation; (b) Distance from Edge

5.3.2 Optimization of the triangular bluff body

The triangular shape was first made using an equilateral triangle with its position placed in the middle of the axis of the beam. The study in optimizing the geometry of the triangle mainly differed in the angle of rotation from the axis (Figure 26 (a)), placement of the beam on the triangle (Figure 26(b)), and angle of the triangle tip (Figure 26 (c)).

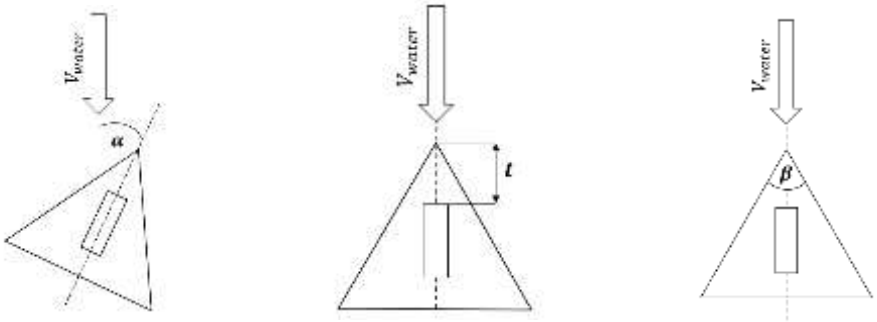

(a) (b) (c)

Figure 26 Parameters of change for optimization study; (a) Rotation about the axis; (b) Distance of beam on bluff-body; (c) Internal angle variation

For the study of the angle of attack through rotation of the beam along the axis the effect of the potential pressure difference between either side of the beam normal to the water flow was studied. During the frequency study comparison at the natural frequency of the harvester, there was no discernable change between the average and maximum resultant amplitude when changing the rotation angle. Moreover, beam

placement on the equilateral triangular bluff-body was studied; the distance was varied between 5mm to 23mm and was constrained so that the beam was not placed outside the boundaries of the bluff-body. However, the results of the frequency study indicated that at resonance, the placement of the beam did not affect the average and maximum resultant amplitude by a difference higher than 1.2%. The final configuration applied to the triangle bluff body varied the internal angle at the tip where the edge impacting fluid is varied from 16 to 75 degrees. This configuration change had the highest impact on the difference in average and maximum resultant amplitude with 4.95% and 8.62%, respectively. The conclusion from this optimization study was that the tip ranges between 40 to 65 degrees were the most optimal internal angle for isosceles triangle bluff-bodies in the parameter change shown in Figure 27. Further optimization studies into the triangular bluff body will require electromechanical coupling parameters by including a resistor across the piezoelectric energy harvester.

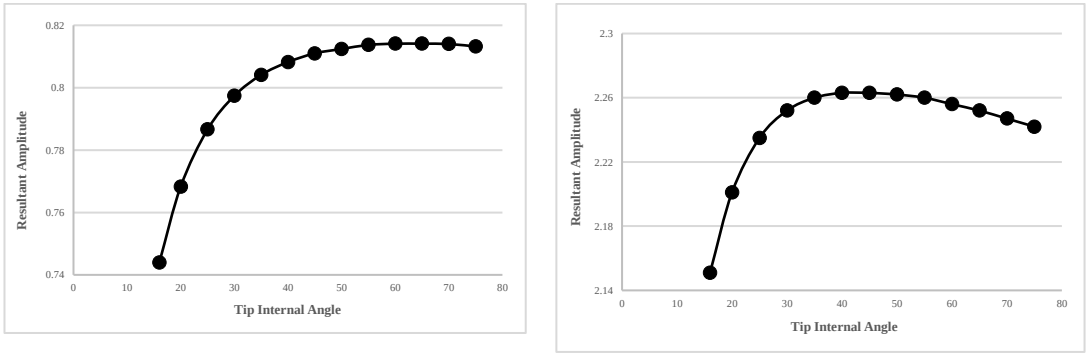

(a) (b)

Figure 27 Resultant Amplitude for Varying Triangular Internal Tip Angle; (a) Average Resultant Amplitude; (b) Maximum Resultant Amplitude

5.2.3 Optimization of elliptical bluff body

After evaluating a cylindrical shape bluff body and not having any parameters

to change, the ellipse shape was used because the ratio of height (a) to width (b) could be varied as well as the rotation around the axis. The following results outline the simulation findings for the ellipse shape for the varying size ratios as shown in Figure 28. The results of the preliminary testing for the ellipse ratio are shown in Figure 29 and Figure 30.

The study of the ellipse looked at the effect the difference in the length and width sizing parameters had on the performance of the bluff-body attached to the energy harvester. The frequency study demonstrated a small difference in varying ellipse sizing with the 1x ratio (circle) performing the worst and 2.5x performing the best at a difference of approximately 0.5% in the resultant amplitude. Also, the 2.5x ellipse sizing provided the highest strain on the beam after only 1 second in the dynamic simulation.

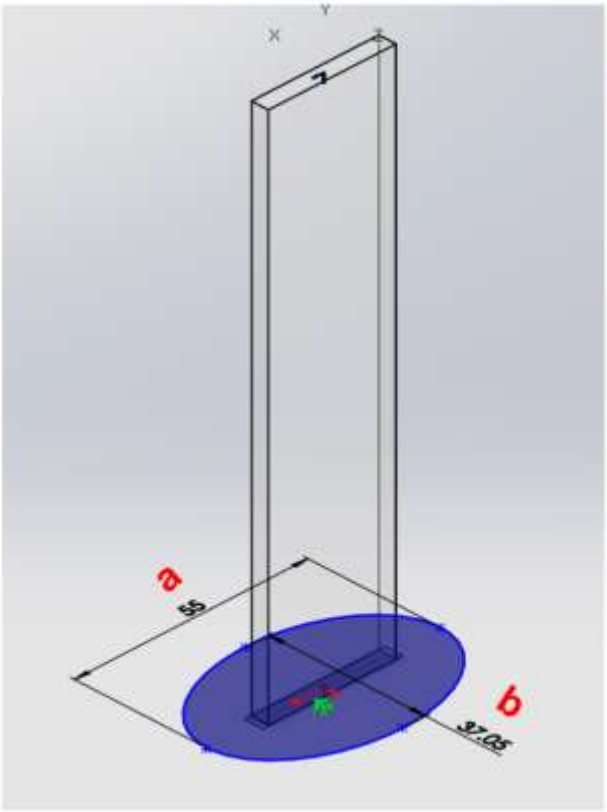

Figure 28 Ellipse Size Ratio Geometry Study Optimization (a/b)

Table 5 Frequency Simulation for Different Ellipse Size Ratios

Shape Ratio Size (a/b)	**Mass Properties (g)**	**Resonant Frequency**	**Sum AMPRES**	**Average AMPRES**	**Maximum AMPRES**	**RMS**
0.5	120.72	25.22	1238.00	0.5125	1.409	0.6719
1	120.71	25.333	1245.00	0.5154	1.416	0.6756
1.5	120.73	25.369	1247.00	0.5164	1.419	0.6768
2	120.70	25.396	1248.00	0.517	1.42	0.6777
2.5	120.72	25.407	1058.00	0.5178	1.421	0.6793
3	120.72	25.413	1061.00	0.5166	1.421	0.6751
3.5	120.72	25.419	1061.00	0.5168	1.421	0.6753
4	120.72	25.426	1061.00	0.517	1.422	0.6756

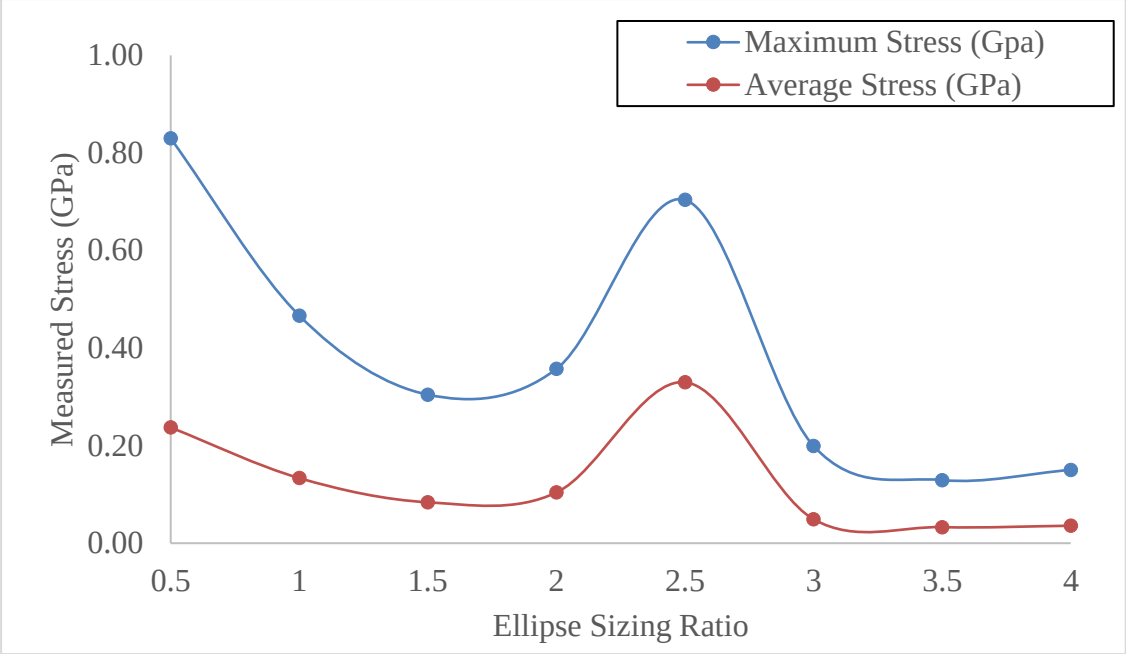

Figure 29 Dynamic Stresses of Different Ellipse Size Ratios during Non-Linear Simulation Study at 1s

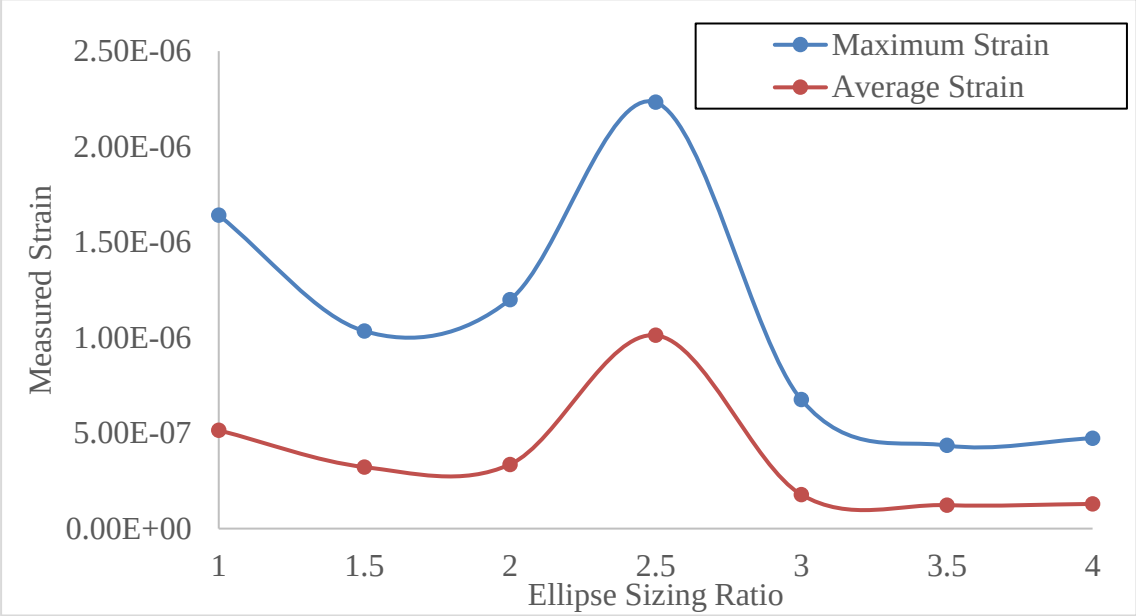

Figure 30 Dynamic Strain of Different Ellipse Size Ratios during Non-Linear Simulation Study at 1s

From Table 5, Figure 29, and Figure 30, it can be seen that the 2.5 ellipse size orientation under the frequency study provided the highest average resultant amplitude

for the first mode and a relatively high maximum resultant amplitude. Moreover, when looking at the non-linear dynamic study, the 2.5 ellipse size ratio also has a high stress and strain output compared to the rest of the sizes. That is to say that the 2.5 size ratio provides the best ellipse performance if the 0.5 ellipse size ratio is neglected, where it is expected to have the higher deflection due to having a wider surface area for contact. Table 7 - Table 8 and Figure 31 - Figure 34 show the summarized results of the study.

While the main objective of such a study is to observe the best performance under resonance (a setting that ideally would net the highest energy harvesting), it is also important to compare that to potential stresses that are exerted on the structure to visualize points of failure or fatigue. A summary of the parameters that were changed and observed during the optimization study is shown in Table 8.

5.2.4 Bluff Body Shape Selection

While the main objective of this study is to investigate several factors that can improve the hybrid energy harvester, it is also important to compare that to potential stresses that are exerted on the structure to visualize potential areas of failure or fatigue, while a strain can be used to correlate piezoelectric performance. ‘Triangle reverse’ refers to a reverse flow direction, ellipse sizes were varied in size and angle of attack by 45 degrees and ‘square’ uses a bluff body in the shape of a square.

Figure 31 and Figure 32 looked at the normalized frequency response of different bluff bodies with identical masses and measured the resultant amplitude at the beam. The results show average nodal values as well as the maximum nodal value along the beam which correlates to the energy harvesting piezoelectric patch that would be attached. The maximum resultant amplitude produced by the shape of the ellipse with the 2.5 size ratio for the average and maximum was visibly higher than the other shapes.

While the ellipse did not generate a significant amount of turbulence based on the CFD study in comparison to the triangle or the cylindrical bluff body, this highlights that the mechanical structure also plays a significant role in the energy harvesting performance under resonance.

The ellipse that was rotated at an orientation of 45 degrees on the axis has the highest measurable stress, this is likely due to the structure that channels the water flow more along one side and generates a higher-pressure difference across both sides which leads to a higher dynamic deflection and forces the formation of vortices and turbulence behind the bluff body. Although the vortex shedding phenomenon for a cylinder bluff body is a well-researched topic, the effects of wake galloping after the onset minimum velocity have shown how triangular bluff bodies can also harvest more energy. Also, the placement of the beam on the bluff body highlights the opportunities for more optimization that enables the elliptical bluff body to produce small turbulence to have the highest average resultant amplitude under resonance.

Overall, the simulation study showed that the bluff-body with a triangle and ellipse shape outperforms the cylinder orientation at 1.24m/s velocity when comparing values that correlate to the potential energy harvested by a piezoelectric beam that the initial model was developed on. Both the fluid and structural interaction because of vortex shedding also plays a significant role in the bluff-body's performance to generate the vibration required to excite the energy harvester. Consequently, the triangle-shaped bluff body has an abrupt change in which the flow of water generates vortices because of the discontinuity in the wake of the edges of the shape. The overall pressure difference around the shape leads to vortex-induced vibration on the structure

Table 6 Parameters changed during the optimization study

Parameters Varied	**Bluff Body Shape**	**Range of Variation**
Rotation about the central axis	Triangle	0° to 90°
	Ellipse	0°, 45°, and 90°
	Quadrilateral	0° (square) and 45°
Beam placement from the edge of the body	Triangle	$5mm$ to $23mm$
The internal angle relative to fluid flow	Triangle	16° to 75°
Size ratio (length/width)	Ellipse	1 to 4

Table 7 Comparison of Frequency Simulation Study for Various Shapes

Shape Type	**Mass Properties (g)**	**Resonant Frequency**	**Sum AMPRES**	**Average AMPRES**	**Maximum AMPRES**	**RMS**
Triangle Edge (50 deg)	120.71	25.314	1006.00	0.5149	1.423	0.6751
Triangle Normal (50 deg)	120.71	25.311	1454.00	0.5147	1.423	0.6745
Cylinder	120.71	25.333	1245.00	0.5154	1.416	0.6756
Ellipse (2.5x point)	120.72	25.407	1058.00	0.5178	1.421	0.6793

Table 7 Comparison of Frequency Simulation Study for Various Shapes

Ellipse (0.5x flat)	120.72	25.22	1238.00	0.5125	1.409	0.6719
Ellipse (45deg rot.)	120.72	25.284	1242.00	0.5141	1.413	0.6739
Diamond	120.70	25.331	1007.00	0.5156	1.416	0.676
Square Normal	120.70	25.336	1007.00	0.5155	1.416	0.67

Table 8 Comparison of Various Bluff Body Shapes after 1s in Nonlinear Dynamic Study

Shape Type	**Mass Properties**	**Max. Stress (Pa)**	**Average Stress (Pa)**	**Max. Strain**	**Average Strain**	**Max. Amplitude (mm)**
Triangle Edge (50 deg)	120.71	5.03E+05	1.43E+05	5.53E-06	1.76E-06	1.84E-03
Triangle Normal (50 deg)	120.71	8.63E+05	2.52E+05	9.86E-06	3.09E-06	5.70E-03
Cylinder	120.71	4.67E+05	1.34E+05	1.64E-06	5.15E-07	1.26E-03
Ellipse (2.5x point)	120.72	7.04E+05	3.299E+05	2.232E-06	1.012E-06	9.602E-03

Table 8 Comparison of Various Bluff Body Shapes after 1s in Nonlinear Dynamic Study

Ellipse (0.5x flat)	120.72	8.30E+05	2.37E+05	2.76E-06	9.16E-07	1.84E-03
Ellipse (45 deg rot.)	120.72	2.766E+06	1.274E+06	8.683E-06	3.911E-06	3.683E-02
Diamond	120.70	7.62E+05	2.172E+05	9.028E-06	2.669E-06	4.980E-03
Square Normal	120.70	6.882E+05	1.739E+05	7.420E-06	2.057E-06	1.048E-02

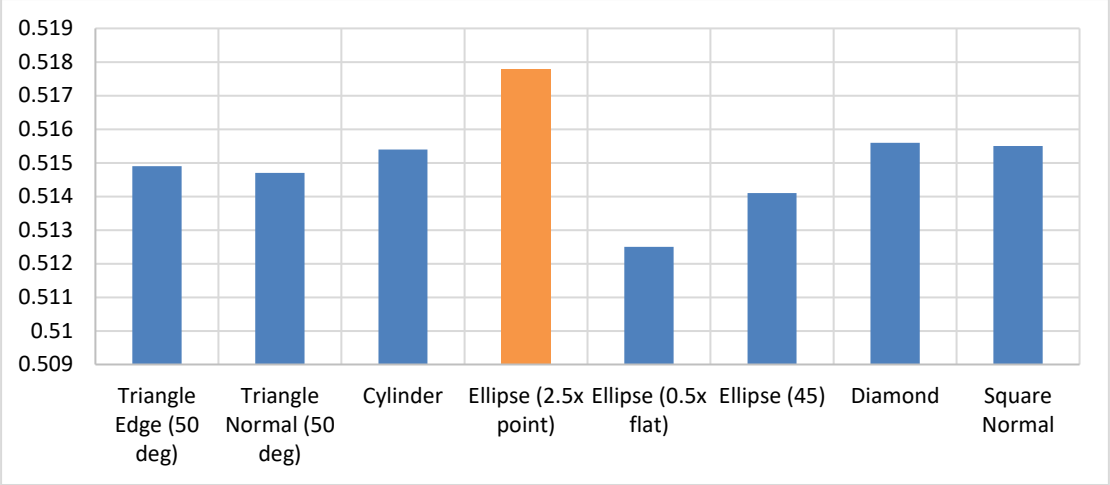

Figure 31 Average Resultant Amplitude of Different Shapes during Frequency Simulation Study

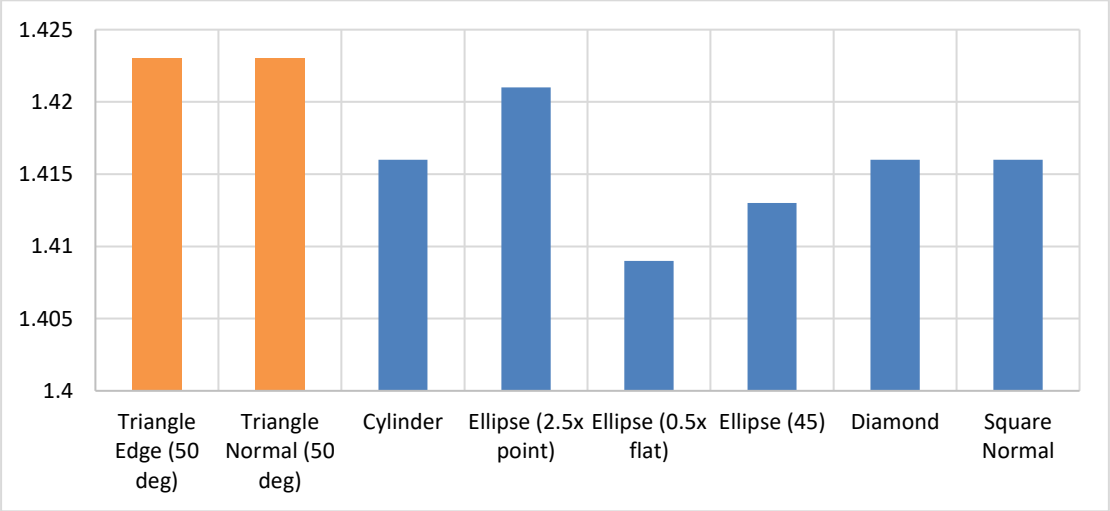

Figure 32 Maximum Resultant Amplitude of Different Shapes during Frequency Simulation Study

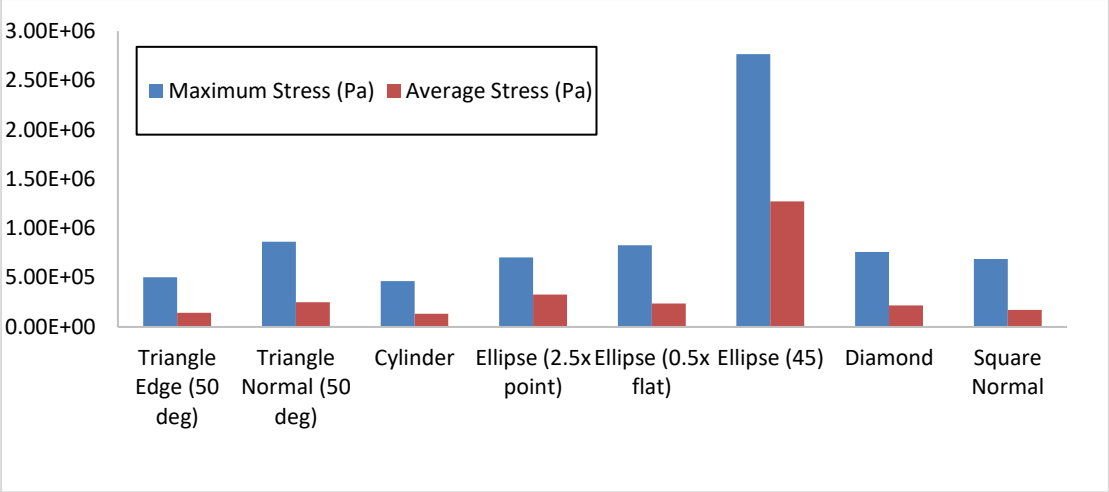

Figure 33 Dynamic Stresses of Different Shapes during Non-Linear Simulation Study at 1s

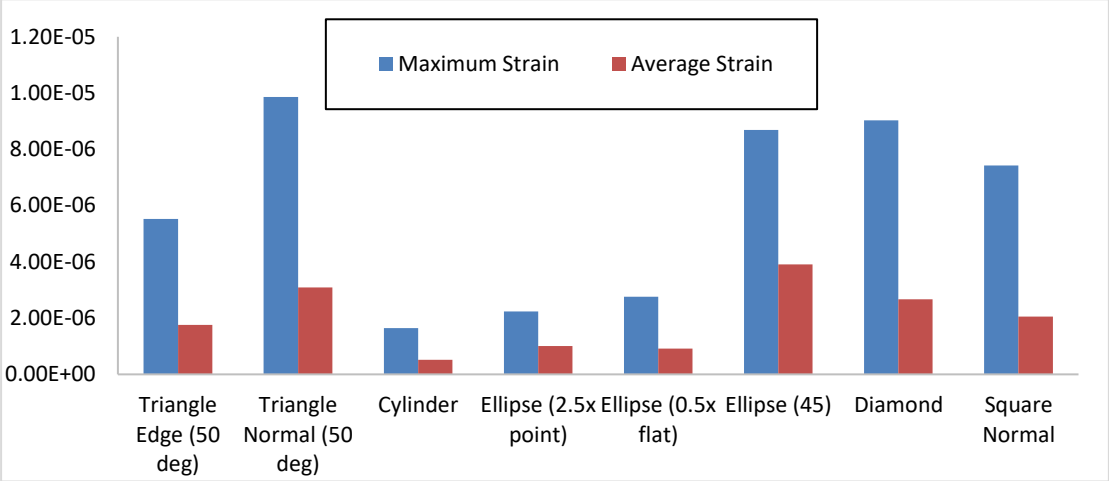

Figure 34 Dynamic Strain of Different Shapes during Non-Linear Simulation Study at 1s

To summarize the different shape types; the triangle edge is where the water flow hits the corner of the triangle; triangle normal is the orientation where water flows in the reverse direction and hits the bluff-body at back (the largest surface area); ellipse describes the ellipse-shaped bluff-body with a ratio of 2.5 (length/width) at the corner; while 0.5 (length/width) is the orientation where the ellipse is oriented such that the largest surface area comes into contact first; diamond orientation is where a

quadrilateral bluff-body orientation has the corner pointing towards the water first, and square normal is where the water comes into contact with the larger surface area of the flat side of the shape. From the frequency study graphs above, the maximum amount produced by the shape of the ellipse with the 2.5 size ratio during average resultant amplitude has a high maximum resultant amplitude when compared to the other shapes (and outperforms the control shape of a cylinder). Also, the ellipse that was oriented to 45-degree shows as having the highest stress, this is likely due to the larger surface area encountering the water flow and causing the water separation that leads to a higher dynamic deflection due to the pressure difference. Moreover, this orientation generates more stress than the larger contact surface area in the 0.5 size ratio; this hints the fluid mechanics' properties play a more significant role than the mechanical shape – this is despite the wider ratio exhibiting poor performance in the frequency study. That is to say that the fluid properties of the turbulence and wake formation also play a major role in the oscillator's configuration to generate the vibration required to excite the energy harvester. From the above study, it seems that despite the normal water flow (where water is hitting the largest surface area) for the orientation of the triangle and square, the performance of these oscillators does not change under resonance.

Overall, the progress thus far on the piezoelectric and electromagnet coupled energy harvester has shown acceptable results and findings for optimizations. The MATLAB code has been used to observe the expected response of both methods of generating electricity which was drawn from the derived equations. Afterward, the SolidWorks platform was used to visualize the oscillations and estimate structural properties that are exerted from the water flow. After completing the preliminary study, variables were fixed and controlled since the findings for changing some variables did not significantly impact the findings and would not need to be optimized. All the shapes

exhibit the same first mode shape for a fixed range of water flow exiting the oscillator; that is, having a transverse amplitude that resonates with the water flow. By running an optimization study, the different oscillator shapes showed that the performance of the ellipse with a size ratio of 2.5 performed the best during resonance with the frequency study as well as the strain experienced from the non-linear dynamic study.

5.2.2 Voltage Output FEA Simulation of Hybrid Energy Harvester

The structural response of the vortex-induced vibration on the structure was modeled by ANSYS Academic 2020R2. Force coefficients from the CFD simulation were coupled afterward to the Finite Element Simulation with the same timestep and direction. Blevins [47] highlighted that the structural response can be modeled as forced response inputs with generally good accuracy. The values for voltage and velocity were recorded for the piezoelectric and electromagnetic systems.

The piezoelectric modeling was performed with a piezoelectric solver extension using two 2814-P2 and one 0714-P2. The results of the simulation were compared to previous work with good convergence [17,98,99]. The constitutive equation of piezoelectric materials expressed in stress-charge form is expressed as [84]:

$$\begin{Bmatrix}\{T\}\\ \{D\}\end{Bmatrix} = \begin{bmatrix}[c^E] & [e]\\ [e]^T & -[\varepsilon^S]\end{bmatrix}\begin{Bmatrix}\{S\}\\ \{E\}\end{Bmatrix} \quad \text{Eq. 44}$$

Where $\{T\}$ represents the stress, $\{D\}$ the electric flux density, $[c^E]$ elasticity at a constant electric field, $[e]$ piezoelectric stress, $[\varepsilon^S]$ dielectric matrix at constant mechanical strain, $\{S\}$ elastic strain vector and $\{E\}$ electric field intensity vector.

The material properties of the isotropic aluminum alloy substrate and the piezoelectric macro-fiber composite modeled after Smart Materials P2 (d_{31} effect) are shown in Table 9.

Table 9 Modeled Properties of MFC-P2

Material Property	Coefficient	Value
Stiffness (10^9 Pa)	$\bar{c}_{11}^E = \bar{c}_{22}^E$	*168*
	$\bar{c}_{21}^E$	*110*
	$\bar{c}_{31}^E = \bar{c}_{32}^E$	*99.9*
	$\bar{c}_{33}^E$	*123*
	$\bar{c}_{44}^E$	*28.8*
	$\bar{c}_{55}^E = \bar{c}_{66}^E$	*30.1*
Relative	$\varepsilon_{11} = \varepsilon_{22}$	*1902*
Permittivity	ε_{33}^S	*1850*
Piezoelectric	e_{31}	*-10*
constants	e_{33}	*2.59*
	e_{15}	*0.1*

5.2.3 Dual-Mass Frequency Tuning

A piezoelectric-electromagnetic energy harvester is more efficient when harvesting energy near the natural frequency of the system because of the large amplitude displacements. Modal analysis of the proposed hybrid energy harvesters was performed where ω_1 and ω_2 depicts the first mode shape for the primary and secondary systems, respectively. The resonance frequency values of the first mode shape for all configurations are shown in Table 10, and the mode shape, when submerged in water, is calculated using the synchronization equation. The piezoelectric volume and mass in

the dual-mass configuration were maintained by using the same dimensions of bluff bodies, substrate beams, piezoelectric patches, and magnet. To save computational time, the viscous effects of the submerged structures were simplified by adding extra mass on the bluff body so that its natural frequency can be reduced to match the vortex shedding frequency, which can be modeled with a low mass-damping ratio.

Table 10 Energy Harvester Structural Natural Frequency for Dual-Mass Systems

Configuration	Primary System		Secondary System	
	$f_{n,1}$ [Hz]	$f_{n,w1}$ $[Hz]$	$f_{n,2}$ [Hz]	$f_{n,w2}$ [Hz]
SDOF (Figure 5)	1.85	1.64	–	–
U-Beam Dual Mass (Figure 8a)	1.83	1.62	21.2	18.8
VB (Figure 9a)	1.84	1.63	27.6	24.5
LV-HB (Figure 9b)	1.86	1.65	27.7	24.6
LV-VB (Figure 9c)	1.85	1.64	27.6	24.5
LH-VB (Figure 9d)	1.87	1.66	22.1	19.6
LH-HB (Figure 9e)	1.86	1.65	29.0	25.8
Main Oscillator System			21.2	
Secondary Oscillator System			29.9	

The shedding frequency generated by vortex-induced vibration has been shown

to come with two distinct frequencies: one transverse and one inline. It has also been well-documented that the inline frequency is double the transverse frequency. While the inline frequency and magnitude are not big enough to overcome the substrate beam stiffness, tuning the structural natural frequency to operate in this region can increase the performance of the energy harvester. The dual-mass harvester can maximize the energy harvested by targeting the transverse frequency for the main system and the inline frequency for the secondary system. The L-vertical cascade system was selected for this orientation to target the dual channel frequency, as shown in Figure 35 (a). The secondary beam had to be optimized to match ω_2 with f_{inline}. To achieve the inline frequency presented in low-velocity flow, the material was changed from aluminum to high-impact ABS for a tuned secondary beam. The tuned beam was applied for the LV-VB, LH-VB, and LH-HB configurations shown in Figure 35 (b), Figure 35 (c), and Figure 35 (d), respectively.

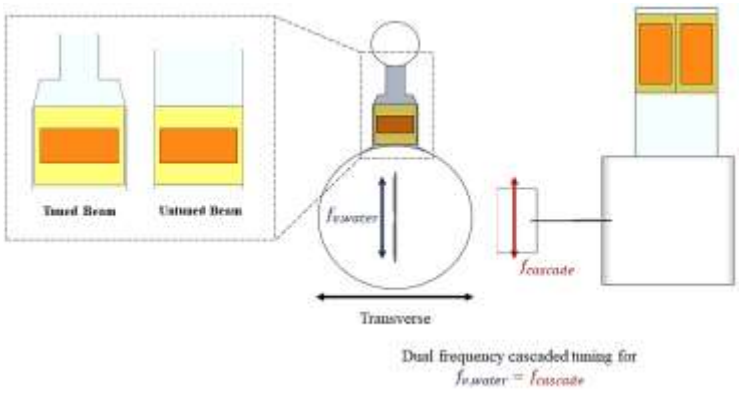

(a)

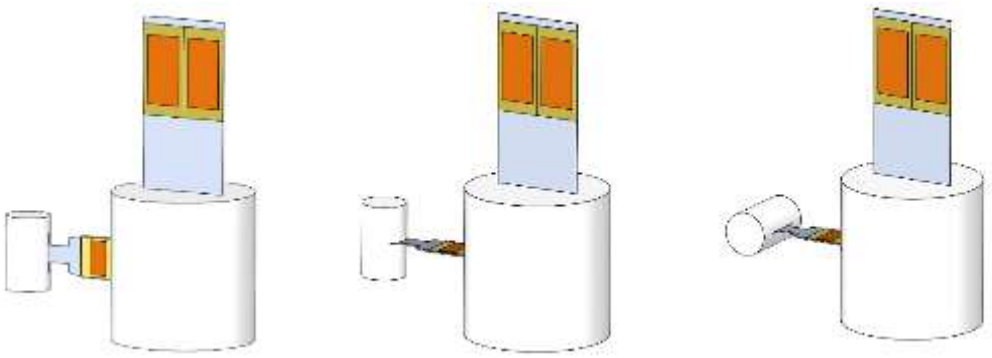

(b) (c) (d)

Figure 35 Dual Frequency Tuning; (a) In-Line Frequency Schematic; (b) Configuration LV-VB; (c) Configuration LH-VB; (d) Configuration LH-HB

Varying the beam shape also affects the voltage output during piezoelectric energy harvesting [8]. The target parameters for dual frequency optimization for this structure are shown in Table 11.

Table 11 Dual frequency design target for tuning cascaded configuration

Parameter		Main (f_1)	Secondary (f_2)
f_n		1.87 Hz	3.74 Hz
$f_{n,w}$		1.76 Hz	3.52 Hz
Onset Synchronization	U^*_{Sync}	5	2.5
	U_{Sync}	0.510 m/s	0.255 m/s
f_{vortex}		1.76 Hz	3.52 Hz

CHAPTER 6: EXPERIMENTAL WORK

6.1 Experimental Setup

The water channel experiment is performed to investigate the hydrodynamic effects on the hybrid energy harvester performance. The experimental setup was performed on an Armstead's open channel water tank setup with an adjustable gate and valve to control both the water velocity and height. The experimental measurements were placed away from the tank's inlet to allow for a fully developed flow in the channel. The measurements were secured by a T-beam clamped to the top of the setup. The experimental setup is shown in Figure 36 and Figure 37.

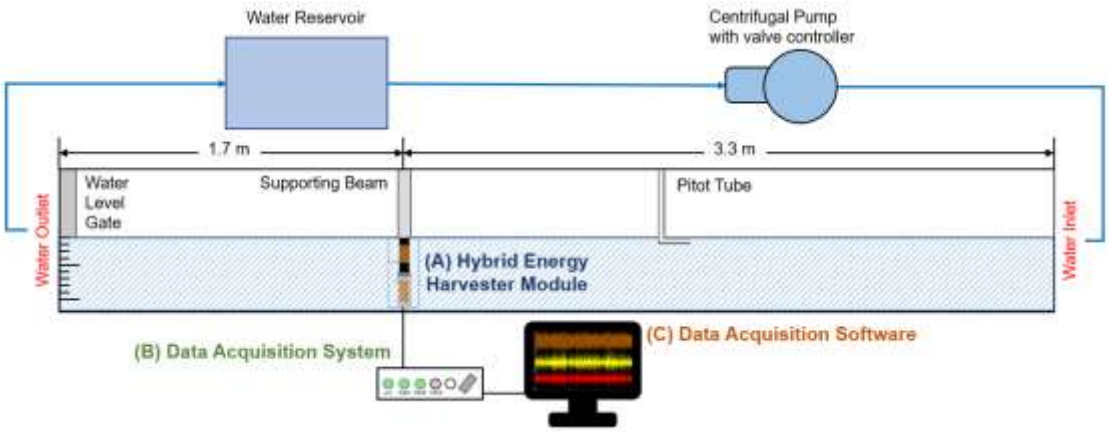

Figure 36 Open Channel Water Tank Schematic

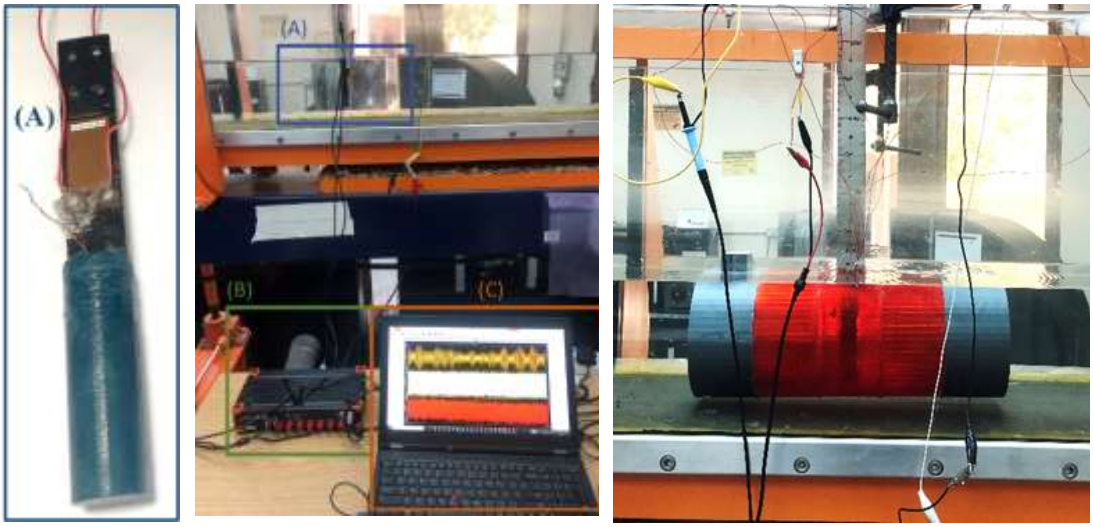

(a) (b) (c)

Figure 37 Experimental setup: (a) energy harvester module (b) fully submerged energy harvester with data acquisition (c) pipe-submerged energy harvester

The data collection and analysis data flow are shown by the signal block diagram highlighted in Figure 38.

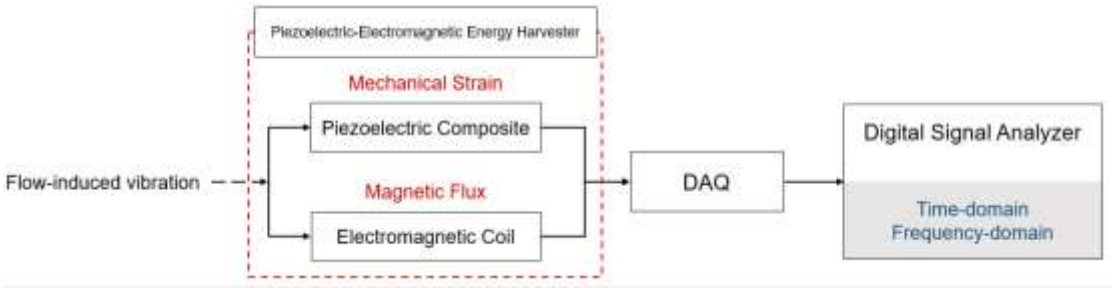

Figure 38 Experimental setup signal block diagram

The experiment was carried out on an open channel research flume developed by Armfield, the setup and details are attached in Figure 39. Water is pumped into the channel, and velocity is adjusted through a shunt on the motor. Water level can also be varied through a gate just before the outlet and can be used to adjust the adequate water

level to reach the bluff body.

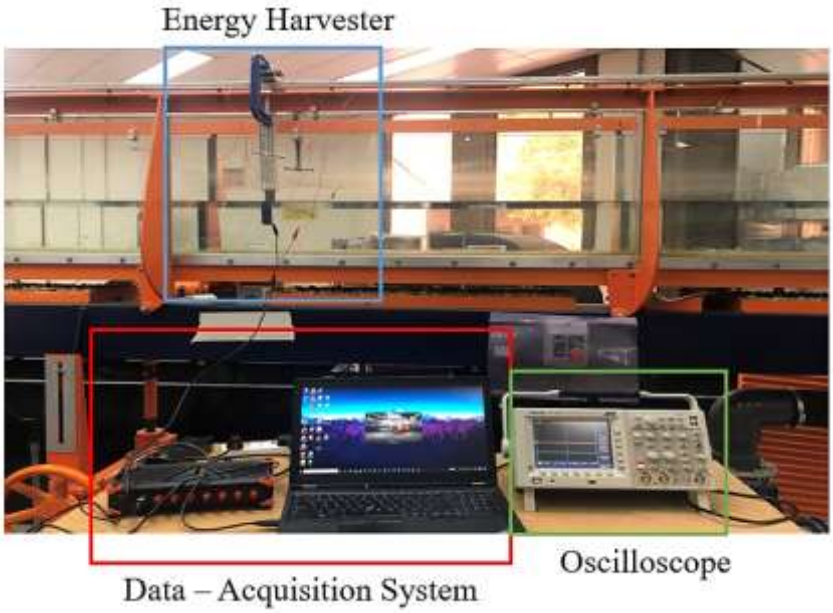

Figure 39 Experimental setup schematic of DAQ

6.2 Tandem Magnetically Coupled Experiment

The tandem magnetically coupled vibration-based energy harvester is shown in Figure 40.

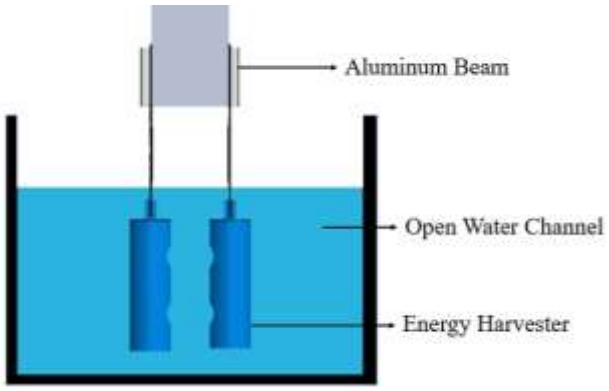

Figure 40 Assembly Tandem Energy Harvester

The performance can be enhanced by harvesting near the natural frequency (ω_n)

of the system. At this point, the bluff body oscillations reach a maximum and piezoelectric strain can be converted to voltage in large magnitudes. Table 12 shows the measured natural frequencies of the energy harvester in air and still water. The expected natural frequency in still water is calculated by taking the hydrodynamic effects of the water into account [61]. For the non-magnetically coupled normal tandem harvester, $\omega_{nw,theoretical}$ was about 6% to 13% higher than the value of $\omega_{nw,experimental}$.

Table 12 Natural frequency of tandem energy harvesters

	Normal Tandem Harvester	Magnet Tandem Harvester
Measured natural frequency in air ($\omega_{n,air}$)	8 Hz	9 Hz
Expected natural frequency in still water ($\omega_{nw,theoretical}$)	5.66 Hz	6.37 Hz
Measured natural frequency in still water ($\omega_{nw,experimental}$)	5 Hz	6 Hz
Water velocity corresponding to natural frequency ($U_{\omega nw}$)	0.53 m/s	0.63 m/s

The experiment first measured the response of a single piezoelectric system, the Fast Fourier Transform analysis is shown in Figure 41. The harvester operates at a low frequency, this is advantageous because a lower mass ratio can help with VIV oscillations [72]. Since the energy harvester was designed for low frequency and first resonance point, the analysis only looked at a maximum of 12Hz.

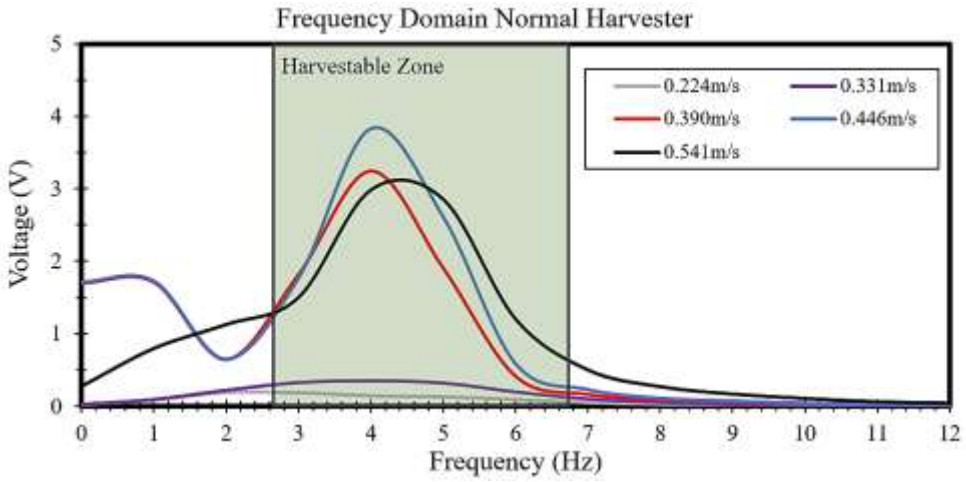

Figure 41 Frequency Response of Normal Tandem Mass Energy Harvester

Afterward, the tandem magnetically coupled system is inserted into the water tank and the voltage output is recorded via DeweSoft Data Acquisition System, and the water velocity is also recorded at each reading. Table 13 represents the root mean square voltage output over the measuring range for a single energy harvester (SEH) and DEH. Only one value of SEH was taken for reference and the remaining study was performed on DEH configuration.

Table 13 Comparison between single and double energy harvesters

Water Velocity (m/s)	Maximum Voltage Output (V)			Magnet Enhancement (%)
	SEH	Normal DEH	Magnet DEH	
0.200	0.170			
0.224		0.161	0.578	259% *
0.331		0.367	0.247	-32.7%
0.390		0.56	3.92	600% *

0.446		8.07	3.60	-55.4%
0.541		2.33	1.75	-24.9%

∗ Visible broadband enhancement out of synchronization area

Table 13 shows that as the velocity increases, the amount of vibration also increases as more vortices as formed and is high when close to the natural frequency. The main drawback of a narrowband energy harvester can be seen when comparing a single harvester to a tandem harvester where the performance is extremely limited. The importance of synchronization is clear when the peak output of the normal DEH in linear resonance is equal to 8.07V. The reason for the lower RMS voltage in DEH compared to SEH at lower velocities is due to vortex formation suppression but also as a result of the "added stiffness" nonlinear effect the magnets exerted. This added nonlinearity from the magnets helped improve the broadband response but shifted the natural frequency of the system such that the original vortex shedding frequency no longer experiences resonance at 0.446 m/s velocity flow. The addition of the magnet has improved the RMS voltage performance, even at lower water velocities, by 259% and 600% for 0.224 m/s and 0.39 m/s. Despite this, the normal tandem harvester outperformed the magnetically coupled harvesters at 25-55% when close to resonance. The frequency performance is shown in Figure 4 through a Fast Fourier Transform (FFT). Here, the outlined harvestable zone is the area where efficiency for the energy harvester configuration is near to maximum. The normal harvester shown in Figure 41 has a narrow window for enhancing performance whereas the magnetic harvester in Figure 42 has a wider window and can be used for the design of variable flow velocities. The synchronization region of the energy harvester has been increased by 35% with the use of magnets placed 20mm apart.

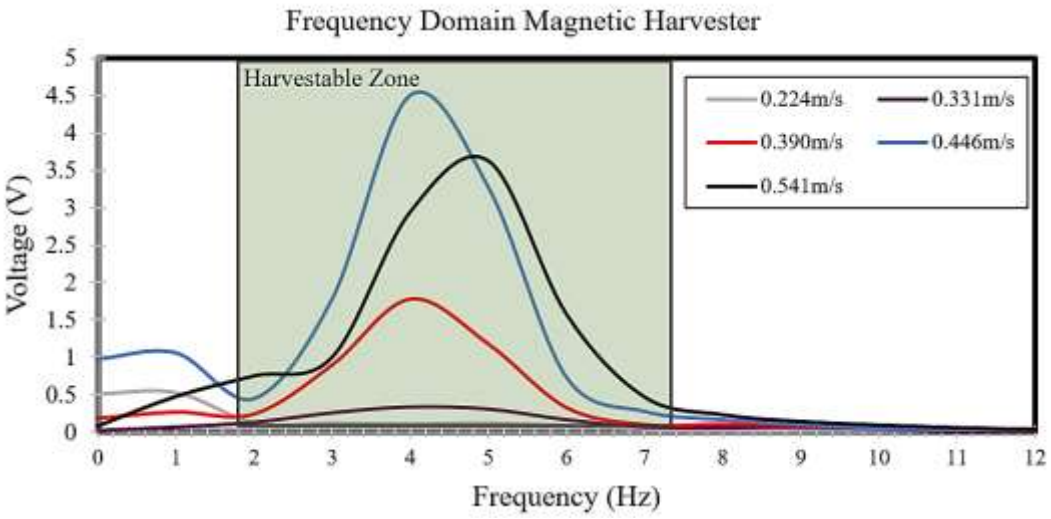

Figure 42 Frequency Response of Magnetically Coupled Tandem Mass Energy Harvester

6.3 Hybrid Energy Harvester

6.3.1 Setup

The maximum field strength is reached in the middle of the total wire coils when implementing an electromagnetic core. By implementing multiple stages, the proposed cores will have multiple concentration points of maximum strength and, therefore, can help enhance the hybrid harvester's performance. In total, 204 coils were used in the core and were kept constant throughout the different configurations, as shown in Figure 43, and the hybrid energy harvester is shown in Figure 5.

(a) (b) (c)

Figure 43 Internal electromagnetic core configurations: (a) 1-stage; (b) 2-stage; (c) 3-stage

As shown in Figure 43, the various stages of the electromagnet allow for multiple local maximum magnetic fields at the coil center. Maximizing the performance of the electromagnetic oscillator is possible by comparing the voltage output between the different multiple stages. Multiple-stage electromagnetic coils can create a larger flux change rate, leading to a higher output voltage [67,100,101].

To display the full implementation of the hybrid energy harvester in internal fluid flow, a second experiment was conducted to test and compare the performance underwater. The macro fiber composite plates were insulated from the water inside the pipe to protect them from erroneous readings. A transparent pipe setup was used to observe the oscillations of the bluff body as shown in Figure 37. The circular pipe and measurements were placed far from the inlet of the water tank to allow for the fully developed flow shown in Figure 44. Because of the transition from an open channel to a pipe configuration, more turbulence is caused at the pipe's inlet. The entrance length for the circular pipe was shorter than the recommended entrance length to develop the new velocity profile due to limitations in the experimental setup. Nevertheless, the actual velocity profile will influence the open channel and tend to be faster near the

surface level than in the middle where the bluff body lies. Figure 44 shows the transition of a velocity profile for a fully developed flow transitioning from an open channel to a circular pipe.

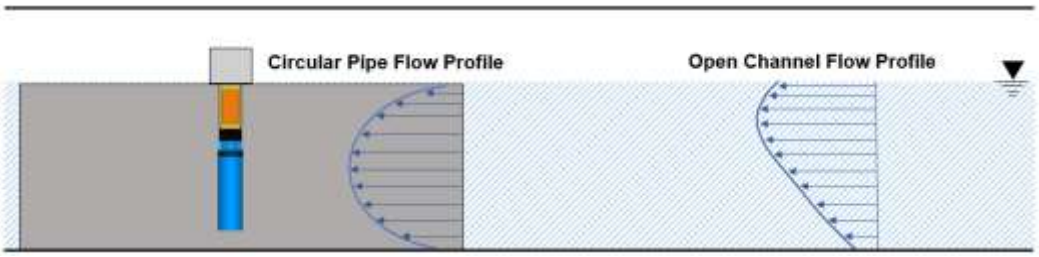

Figure 44 Velocity profile in a fully submerged experimental setup

6.3.2 Synchronization and Natural Frequency

Based on the equations, the added components of submergence in water can shift the natural frequency of the hybrid harvester. Since the geometry of the energy harvester is small, the hydrodynamic effects on the natural frequency may be limited and might be approximated using a correction factor. Because the harvester is modular and allows for easy swapping of the electromagnetic coils, they are assumed to have the same natural frequency due to a small deviation in mass for each configuration. The measurements shown in Table 14 were taken using a 2-Stage EM. Measurements were taken over an average of 10 readings using 0.1 Hz sensitivity, for the frequencies involved in this study, this makes up 2% of the expected value.

Table 14 The natural frequency of energy harvester at different submergence depths (pipe)

Dry Air		Partially Submerged			Fully Submerged			Pipe Submerged	
ω_{exp}	ζ_{exp}	$\omega_{ps,theo}$	$\omega_{ps,exp}$	$\zeta_{ps,exp}$	$\omega_{fs,theo}$	$\omega_{fs,exp}$	$\zeta_{fs,exp}$	$\omega_{pp,exp}$	$\zeta_{pp,exp}$
4.5 Hz	0.1	3.4 Hz	3.3 Hz	0.135	3.4 Hz	3.2 Hz	0.12	3.9 Hz	0.18

The results highlighted that the theoretical equations and discrete system modeling could predict the system's natural frequencies. While the entire system is underdamped, the added hydrodynamic effects reduce the natural frequency for the partially and fully submerged system compared to the dry natural frequency that arises from the added mass. Also, the added damping effect is seen. The added boundary effects are seen for a pipe-submerged system as the wet natural frequency is higher than the submerged system with a wider boundary. The results indicate an added stiffness and damping coming from the pipe boundary that is not present when observing the partially and fully submerged systems. The effects of synchronization significantly affect the overall energy harvesting performance of the hybrid energy harvester. Once the vortex shedding frequency matches the structural natural frequency in still water, there is a 'lock-in' region whereby the amplitude of the oscillations increases to a maximum and is advantageous for vibration-based energy harvesting.

The vibration difference comparison is highlighted in Figure 45 (a) and (b), which showed an overall difference of before, during, and after synchronization in the time-domain and frequency-domain, respectively. Under synchronization, the vortex-shedding frequency is close to or at the structural natural frequency in still air and results in a significant increase in vibration amplitude like that seen in resonance for a

vibration-based energy harvester [102]. Unlike pre-synchronization, where the output voltage is less overall and post-synchronization, where there is a period of low voltage output, 'lock-in' region oscillations have more energy, and the feedback results in consistently high voltage output.

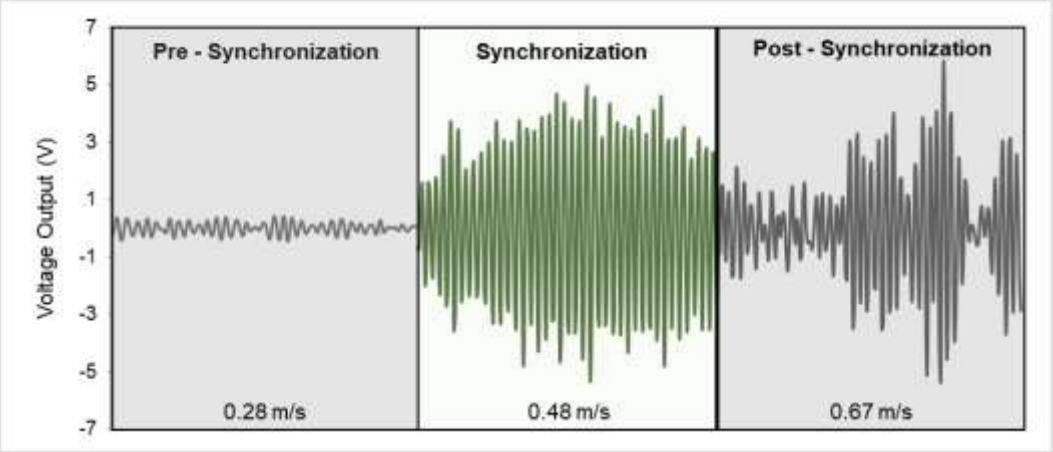

(a)

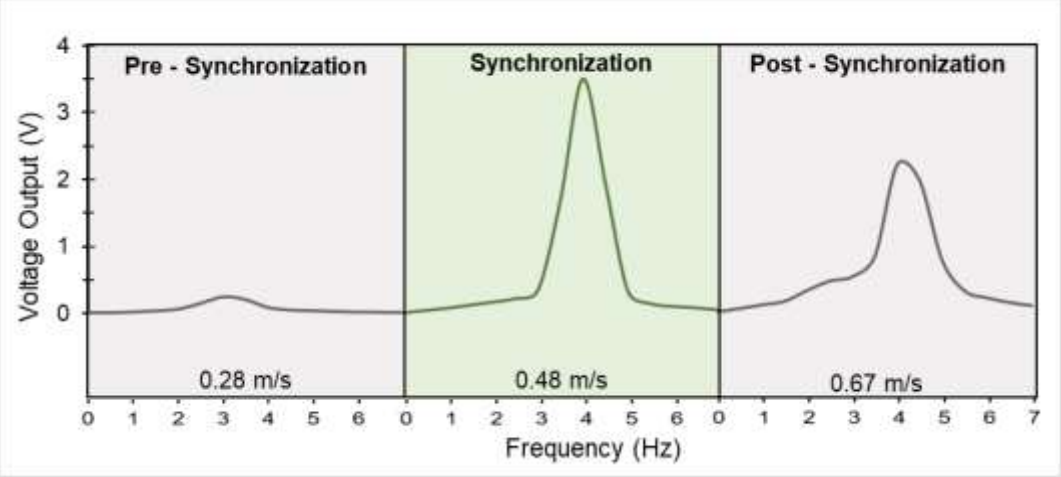

(b)

Figure 45 Synchronization effects for piezoelectric only energy harvester; (a) time-domain; (b) frequency-domain

The connection of the BNC channels to the 2-stage and 3-stage of the electromagnet affects the voltage output as shown in Figure 46. Parallel connections gave the lowest output, while separate and series channel connections had a higher

output. For this experiment, each electromagnet stage is connected to a separate BNC channel so that the effects at each channel can be monitored and compared. The time history for both the piezoelectric and electromagnet harvesting system at resonance is shown in synchronization. The effects of multiple stages are seen to increase the overall energy harvesting property positively.

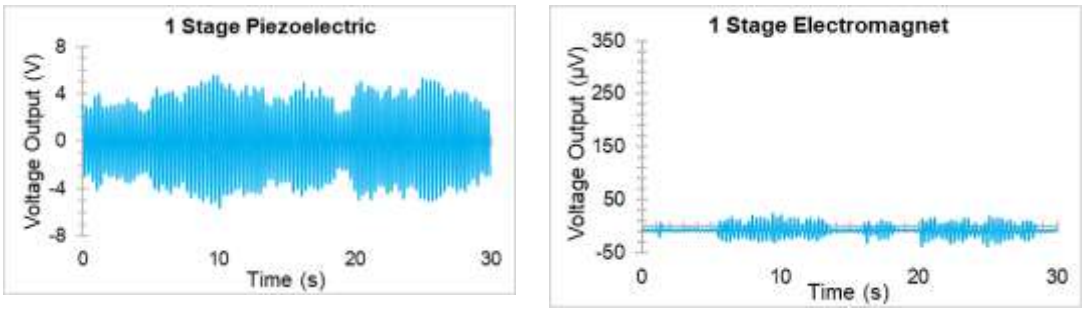

(a)

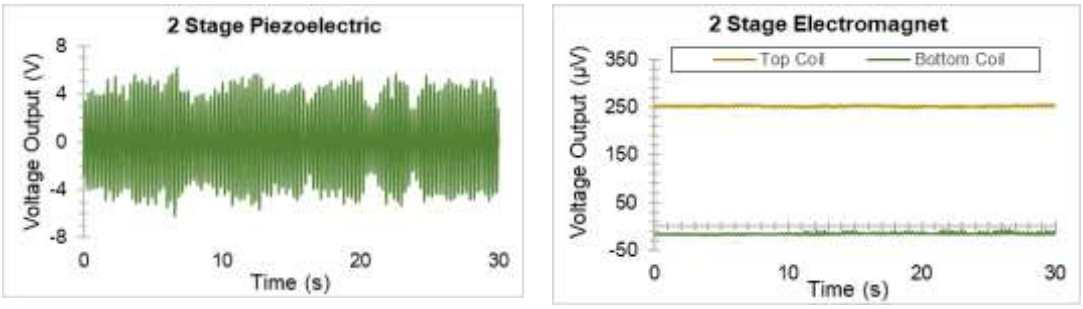

(b)

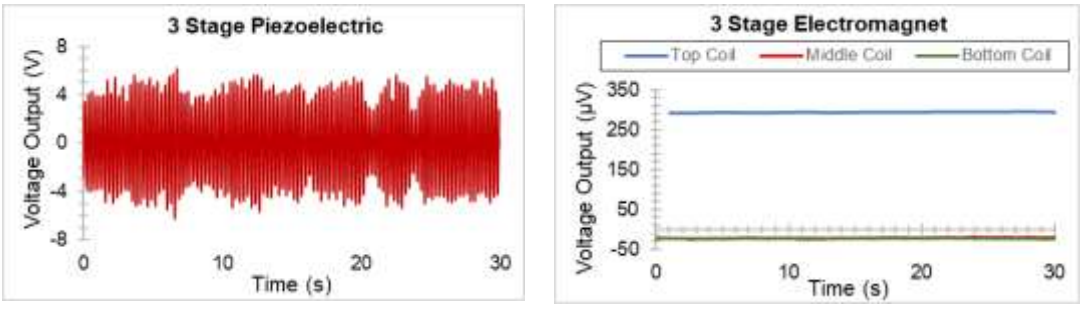

(c)

Figure 46 Time-history plots of different hybrid energy harvester stages at resonances: (a) 1-Stage Hybrid; (2)-Stage Hybrid; (c) 3-Stage Hybrid

The performance analysis for a partially submerged hybrid energy harvester is shown in Figure 47 for piezoelectric only (without an internal electromagnetic system) and different electromagnetic system stages are shown in Figure 48 for RMS Voltage values for a partially submerged setup (up to the top of the bluff body). The impact of the synchronization region is seen where maximum voltage output occurs near the structure's natural frequency. The hybrid energy harvester output is 18%-23% more than the conventional piezoelectric-only harvester when submerged only in the bluff body. Furthermore, the synchronization for the hybrid system starts at a lower velocity compared to the piezoelectric-only configuration. While the mass presented in the EMH system did improve the overall performance, the added mass shifted the 'lock-in' region to a lower velocity. At higher velocities, the performance of the hybrid energy harvester fluctuated because the effects of the boundary condition with the tank at higher velocities started to influence the vortex-shedding. This is seen for velocities above 0.55 m/s, where the declining trend jumps slightly. The effect of the boundary leads to different interactions between vortex-induced vibration and even suppression of vortex development.

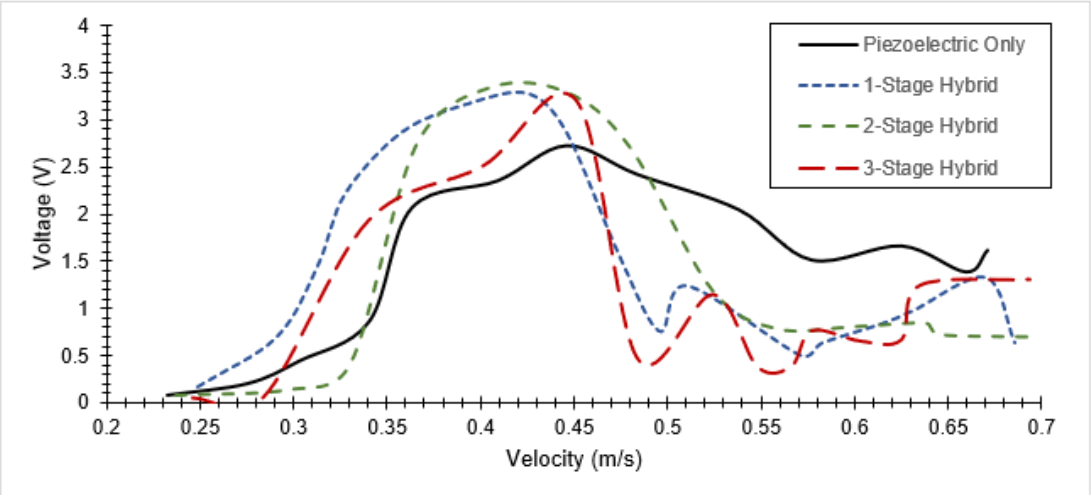

Figure 47 Performance analysis for partially submerged hybrid energy harvester

The best-performing one can be selected for further design considerations by comparing the different electromagnetic configurations. The electromagnetic performance analysis was compared between the three applicable stages and is highlighted in Figure 48. There is a performance difference in coiling configurations, notably for the increase between 1 stage to 2 stages where there was a noticeable increase. However, the difference between 2-stage and 3-stage electromagnetic cores only increased by 34%. The smaller performance increase could be because the spacing (2mm) and the reduced number of coils limit each stage's output voltage. The use of dual magnets with a staged electromagnet system further helps the change in magnetic flux.

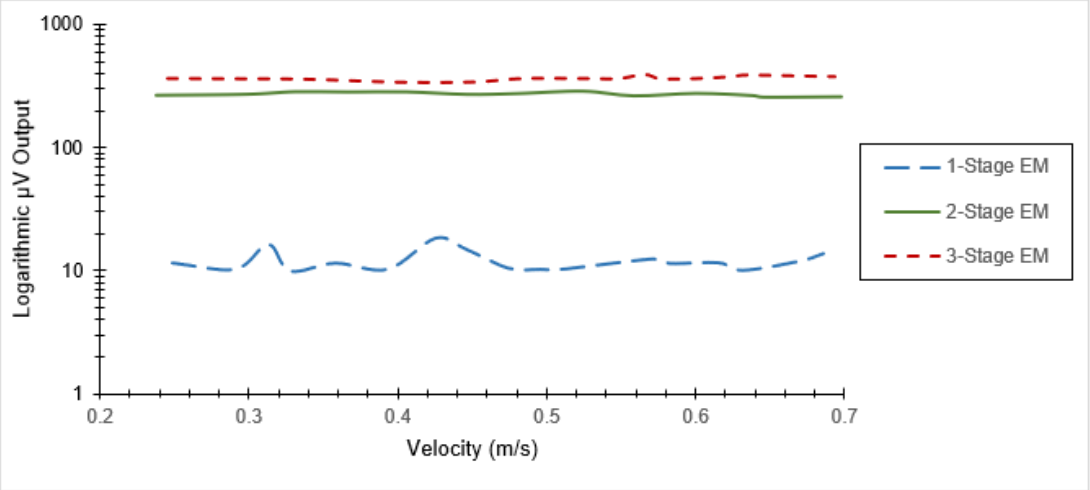

Figure 48 Electromagnetic configuration performance analysis for partially submerged hybrid energy harvester

The performance analysis of the hybrid harvester can further be compared in the frequency domain shown in Figure 49. A distinct peak can be seen for all the configurations at resonance corresponding to the system's natural frequency. The peaks agree with Table 14, which shows that the discrete model approximation for natural-

frequency tuning is applicable in this application. The harvestable zone is characterized as the 'lock-in' region for an elastically mounted cylinder oscillating with vortex-induced vibrations for the velocity range of 0.2 m/s – 0.7 m/s. The narrowband performance is visible for a beam-coupled system with its distinct natural mode shape. Compared to a piezoelectric-only measurement, the added mass of the electromagnetic system has shifted to a lower natural frequency. It allows for potential energy harvesting from low-velocity fluid flow applications. In comparison, the addition of the electromagnet has given the hybrid energy harvester a higher performance than the conventional piezoelectric-only system.

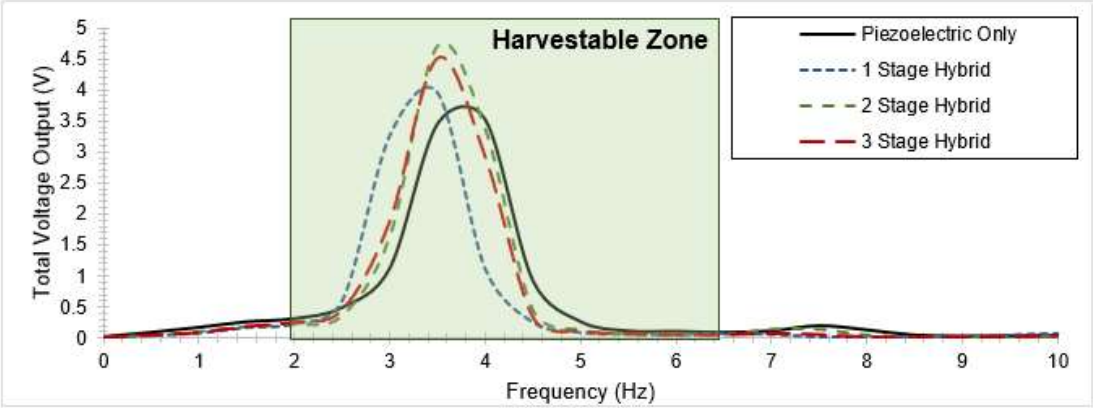

Figure 49 Frequency response of partially submerged hybrid energy harvester

6.3.3 Effects of Submergence Depth on Energy Harvesting

In this section, the results of different boundary conditions are compared. The results for a partially submerged system were taken from the previous section. All measurements used a 2-stage internal electromagnet energy harvesting system as it performed the best in the partially submerged experiments. The results of the RMS voltage output at different measurable velocities were compared for the hybrid output in Figure 50. The damping effect is seen where the pipe-submerged system presented

the lowest overall hybrid performance system while the partially submerged presented the best. The performance output between partially submerged and fully submerged systems dropped by about 71%. This highlights the importance of hydrodynamic effects on the PZT patch.

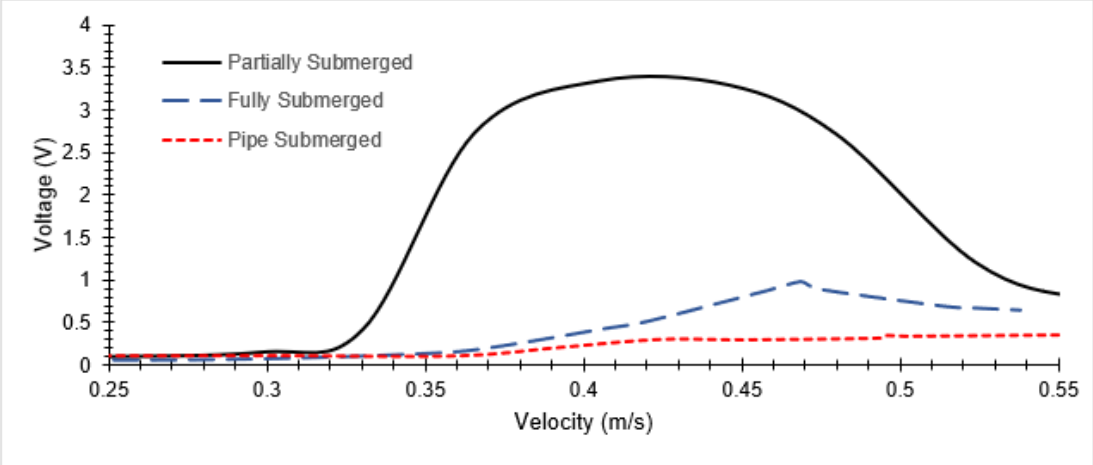

Figure 50 Hybrid energy harvester performance at different boundary conditions

However, fully, and pipe-submerged energy harvesters had a higher voltage output at higher velocities than the partially submerged output and were more sensitive to synchronization effects. On a logarithmic scale, the partially submerged EMH did not present a notable change when under resonance as shown in Figure 51. These results suggest that the energy harvesting properties inside the bluff body performed more favorably with the hydrodynamic effects acting on the substrate beam.

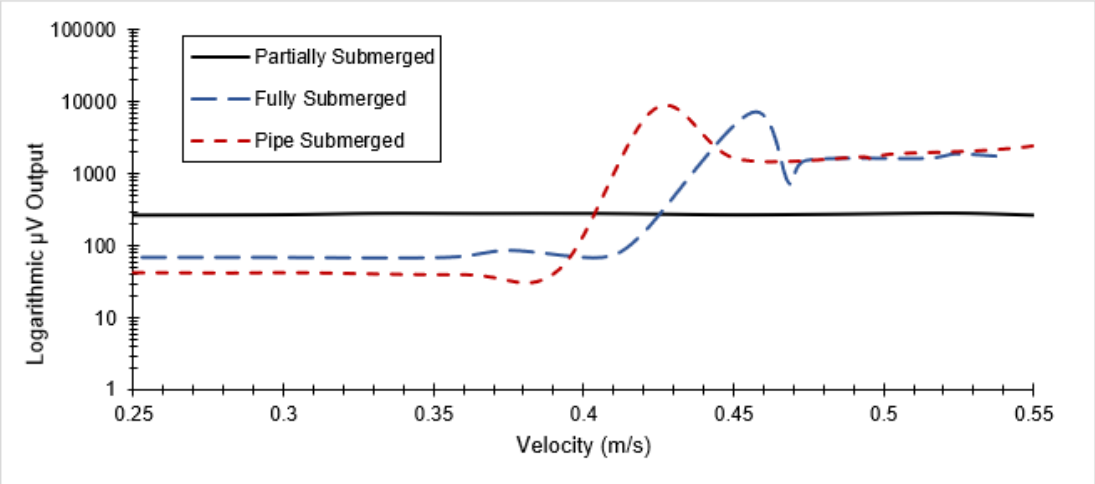

Figure 51 Performance of electromagnetic energy harvester at different boundary conditions

Figure 52 shows the frequency-domain plot of the HEH and supports the values in still water presented in Table 14. The higher damping ratio effects are seen for the fully submerged system and the pipe submerged. Furthermore, the differences in the added stiffness and damping represent the natural frequency shift. However, the peak natural frequency for the pipe-submerged system was slightly higher than the reported value, suggesting that the pipe boundary condition has a more significant impact in flowing water than it does in still water. This can be considered when tuning an energy harvester for pipe applications. A 3D plot showing the effects of synchronization in the frequency domain for the different boundary conditions is shown in Figure 53.

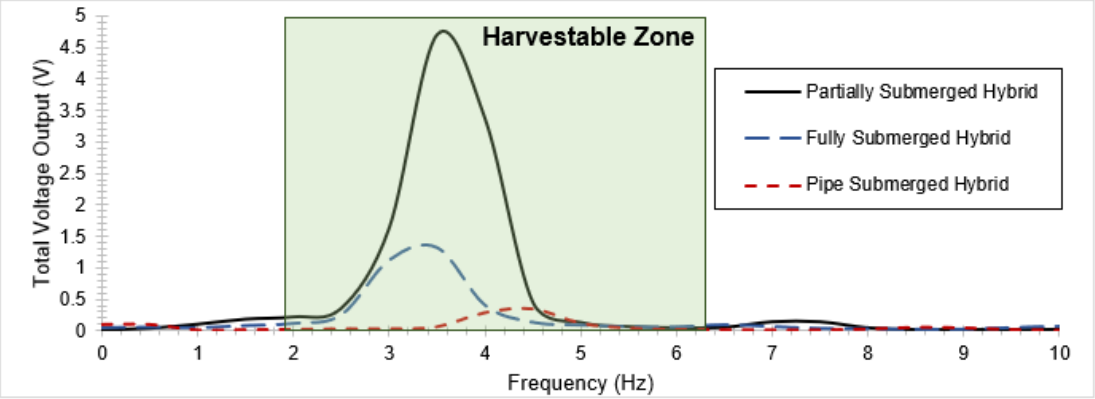

Figure 52 Velocity-averaged voltage output frequency domain for hybrid energy harvesters at different boundary conditions

Figure 53 represents the discretized frequency spectrum and can be seen as a performance output summary of the different submergence boundary conditions at different velocities.

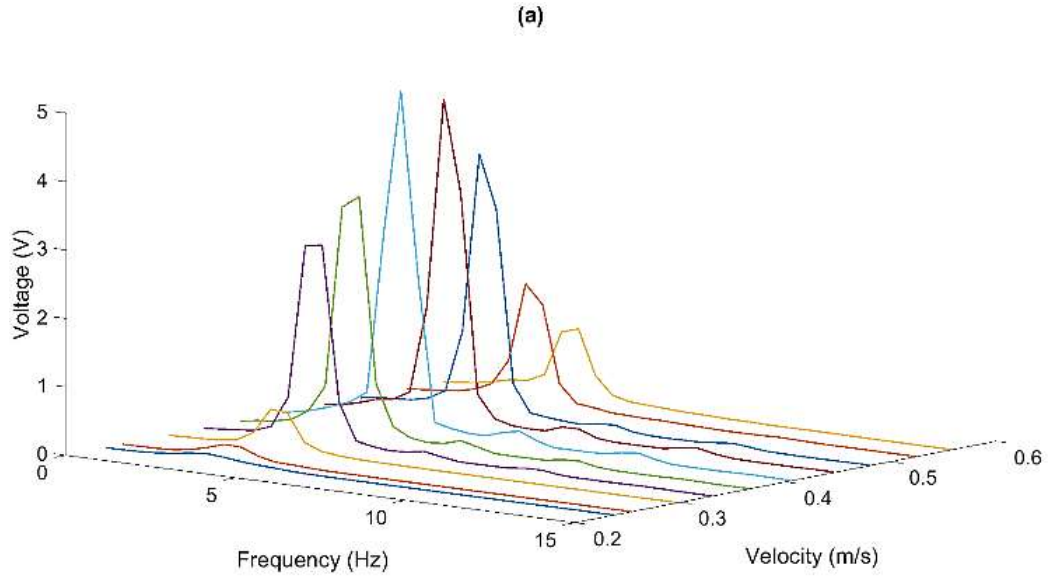

(b)

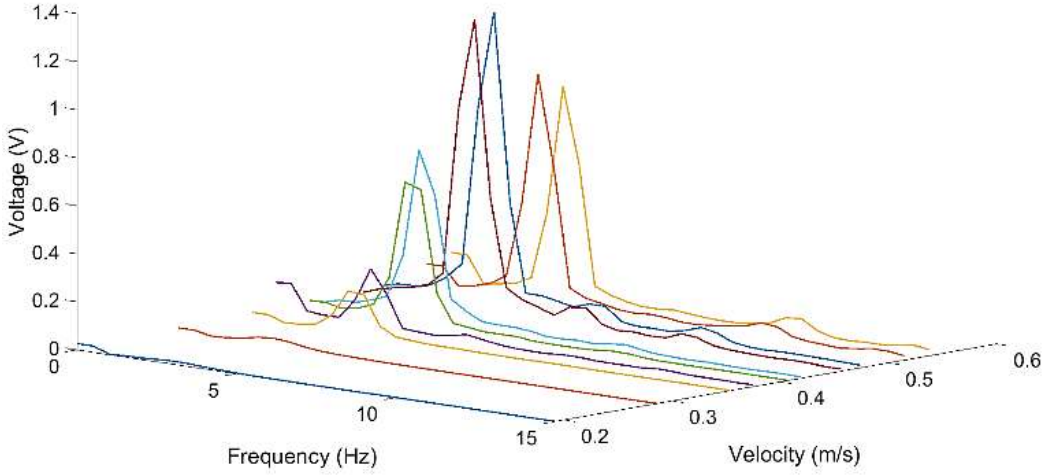
Voltage (V)
1.4
1.2
1
0.8
0.6
0.4
0.2
0
0
5
10
15
Frequency (Hz)
0.2
0.3
0.4
0.5
0.6
Velocity (m/s)

(c)

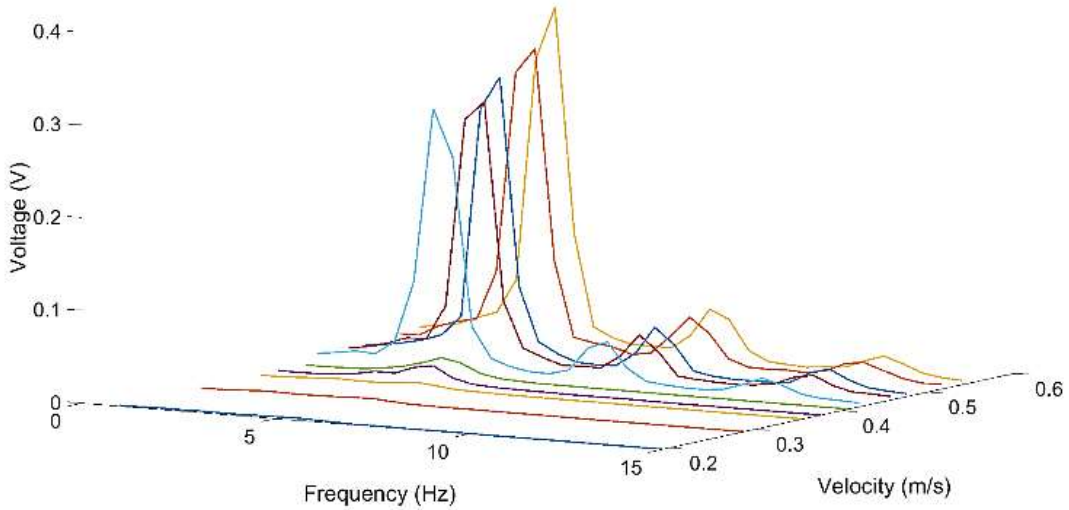
Voltage (V)
0.4
0.3
0.2
0.1
0
0
5
10
15
Frequency (Hz)
0.2
0.3
0.4
0.5
0.6
Velocity (m/s)

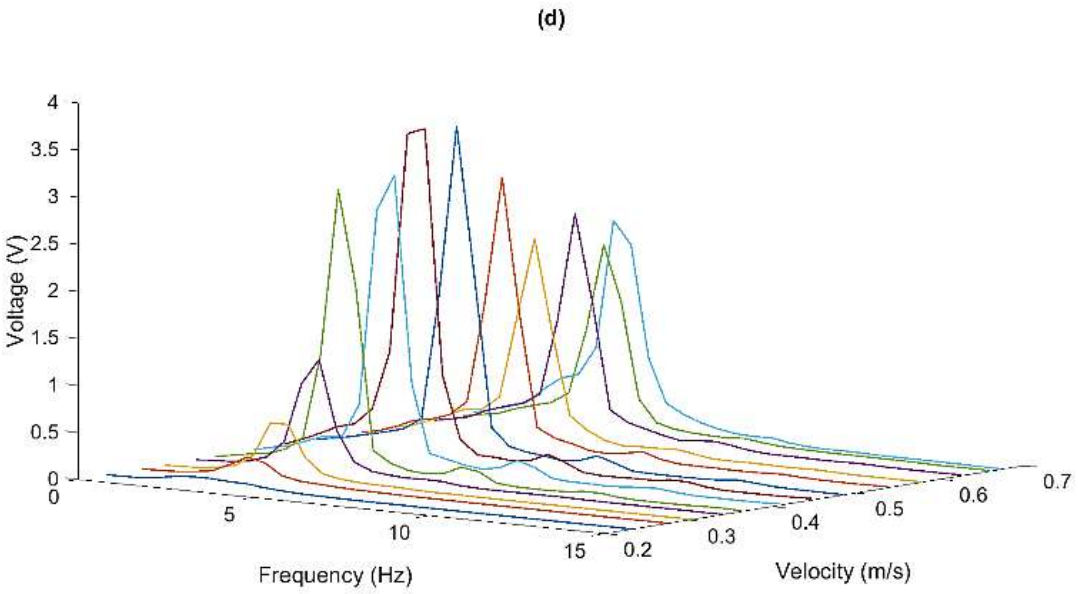

Figure 53 Frequency Response of Energy Harvester Configurations: (a) Partially Submerged Hybrid, (b) Fully Submerged Hybrid; (c) Pipe Submerged Hybrid; (d) Partially Submerged Piezoelectric Only.

Figure 53 (a) and Figure 53 (d) represent the partially (bluff body only) submerged plots where the voltage output was much higher than the other boundary conditions. The addition of the electromagnetic system has shown an overall increase in the peak amplitude at synchronization and can enter the region at a lower water velocity which is ideal for low-velocity applications. The literature has also reported the reduced onset velocity of higher tip masses for VIV applications [14,32,77]. Alternatively, removing an internal system and only utilizing the conventional piezoelectric can improve the system's overall bandwidth at the cost of synchronization peak amplitude. This tradeoff between the bandwidth and the peak amplitude is often used as an optimization parameter for energy harvesting of piezoelectric systems [16,66]. Figure 53 (b) shows the fully submerged hybrid configuration results. It demonstrated the shift in onset velocity to enter the synchronization region and the reduced voltage output because of the added-mass hydrodynamic effects. This effect

becomes more pronounced when observing a pipe-submerged hybrid energy harvester due to damping from the wall interaction suppressing the ongoing vortex-induced oscillations of the bluff body.

CHAPTER 7: CONCLUSIONS AND FUTURE WORK

In the present study, a new compact design of a hybrid energy harvester that uses a piezoelectric and electromagnetic system was developed for use in submerged pipe flow applications. The addition of a tip mass provides a housing for the electromagnetic oscillator but also generates turbulence that is used to generate power. Firstly, a mathematical model was developed for the coupled systems that also includes an electromechanical coupling when the harvester was subjected to transverse oscillations because of vortex-induced vibration. Afterward, a numerical solver was able to get the time and frequency response of the hybrid harvester. From these results, it was shown that by tuning the systems to resonate close to each other, the voltage harvested can be increased. If the resonant point of both systems is tuned to the oscillation frequency of the water flow, then the energy harvested will also be maximized. Then, a computational simulation was performed to observe the vortex shedding behind a cylindrical body by using an unsteady $k-\omega$ SST model over 20s. After validating the convergence of CFD results, the simulation was then expanded for triangular, elliptical, and quadrilateral bluff body shapes. At 1.24 m/s the first mode shape of the energy harvester is the transverse deformation to the direction of the water flow because of the beam orientation having different area moment of inertia. An optimization study was done across the different bluff body shapes and the performance of the bluff body alone as well as the harvester structure was compared. The tip triangle angle presented the highest amplitude oscillations when $40^o < \beta < 65^o$. The isosceles size ratio was also compared, and found that the 2.5x ratio experienced the greatest strain along the beam where the piezoelectric material is to be attached to. While the ellipse generated the least turbulence, the performance of the 2.5x ratio ellipse (average

resultant amplitude) and isosceles triangles (maximum resultant amplitude performed the best during resonance with the frequency study. This suggests the importance of the fluid-structure interaction on the beam as well as the galloping and vortex-induced vibration effects for non-cylindrical bodies. Overall, a magnetically coupled nonlinear vibration energy harvester was investigated with the following conclusions:

- The addition of magnetic nonlinear forces can enhance the energy harvesting properties at lower velocities by 600% and broaden the synchronization range by up to 35%.
- Narrowband piezoelectric energy harvesting is superior for applications of fixed flow and is designed to oscillate near the structural natural frequency.

Afterward, this thesis investigated a hybrid piezoelectric-electromagnetic energy harvester developed for remote sensing applications and low-power devices. A bluff body internally housing an elastically mounted permanent magnet oscillates around a coil to generate voltage through magnetic flux changes. Additionally, a piezoelectric macro-fiber composite attached to a beam substrate generates electricity through mechanical strain. Both hybrid systems were fabricated to be included in a compact form factor for pipeline applications. An analytical model was developed for vortex-induced vibrations of the bluff body in water, where the dynamic model was used with the energy harvesting properties using transverse oscillations. The theoretical model was developed for resonance synchronization at different boundary conditions by considering the hydrodynamic effects of submerged structures for the parameters of effective mass, stiffness, and damping. Afterward, the energy harvesting performance was experimentally studied in an open water channel tank corresponding to different water velocities in an open-channel testing setup. Furthermore, the study expands to the influences of a multi-staged electromagnetic system in enhancing the performance of a

hybrid piezoelectric-electromagnetic energy harvester. Next, the synchronization energy harvesting at different boundary conditions by taking the ratios of damped natural frequency and damping. The experimental findings of this energy harvesting study highlighted that:

- A hybrid piezoelectric-electromagnetic system can harvest energy from water flow and can be tuned for low-velocity use in open-channel or pipeline applications.
- The proposed hybrid energy harvester increased performance by up to 23% compared to conventional piezoelectric-only systems.
- The natural frequency of a discrete model with a bluff body and substrate beam can be predicted with good accuracy for boundless and bounded boundary conditions.
- Electromagnetic harvester performance can be enhanced by implementing a multiple-stage coil winding to have a greater magnetic flux change, with the greatest change from 1-stage to 2-stage.
- Hybrid energy harvesting performance decreased by up to 71% with submergence due to added mass and damping. Pipe boundaries limit the vibration amplitude and require revisions to enable frequency-matching with the added damping and stiffness parameter.

7.1. Recommendation

Future work into the different configurations, magnets, and rectifier systems can further enhance the energy-harvesting properties of the system. Enhancing the broadband properties by varying the magnet strength and orientation would also be part of the additional work. The findings in this work have demonstrated the effectiveness of a hybrid energy harvesting solution in a compact form factor and can be tuned for

narrowband synchronization applications. The performance comparison explored for different fluid boundaries in this thesis can further improve the practicability of self-sustaining wireless sensors. Furthermore, low-velocity energy harvesting is possible with low-cost and scalable technologies using additive manufacturing technologies with engineering materials. Optimization studies on the restricted and free rotation of the bearing-mounted energy harvester can enhance the energy harvested from the composite. In the absence of a bearing mount, misalignment in the beam direction can severely decrease the efficiency of energy conversion.

RELEVANT PUBLICATIONS

Patents

i) Muthalif, Asan G.A, Muhammad Hafizh, Jamil Renno, and Mohammad R. Paurobally. 2022. "Self-Adjusting Rotating Airfoil Piezoelectric Energy Harvester for Fluid-Flow Applications."

Innovation Awards

i) 1st Place Winner for Postgraduate Category, Gulf Petrochemical and Chemicals Association (GPCA) hosted at the 2nd Research and Innovation Conference. *Address Skyview, Dubai, UAE*

ii) 3rd Place Winner, Innovation and Entrepreneurship Annual Contest. *Qatar University, Qatar.*

Web of Science (Clarivate)

Published Work		
S. I	Title	Clarivate Analytics
1	G.A Muthalif, Asan, Muhammad Hafizh, Jamil Renno, and M. R. Paurobally. 2022. "A Hybrid Piezoelectric-Electromagnetic Energy Harvester from Vortex-Induced Vibrations in Fluid-Flow; the Influence of Boundary Condition in Tuning the Harvester." Energy Conversion and Management 256(January): 115371. https://doi.org/10.1016/j.enconman.2022.115371.	Q1, IF: 11.533

2	Hafizh, Muhammad et al. 2023. “Vortex induced vibration energy harvesting using magnetically coupled broadband circular-array piezoelectric patch: modelling, parametric study, and experiments” Energy Conversion and Management, 276, 116559. https://doi.org/10.1016/j.enconman.2022.116559	Q1, IF: 11.533
3	Hafizh, Muhammad et al. 2023. “Vortex-Induced Vibration-Based Self-Tunable Airfoil-Shaped Piezoelectric Energy Harvester for Remote Sensing Applications in Water” Ocean Engineering, 269, 113467, https://doi.org/10.1016/j.oceaneng.2022.113467	
4	Muthalif, Asan G.A., Muhammad Hafizh, Jamil Renno, and Mohammad R. Paurobally. 2021. “An Enhanced Hybrid Piezoelectric–Electromagnetic Energy Harvester Using Dual-Mass System for Vortex-Induced Vibrations.” JVC/Journal of Vibration and Control 27(23–24):2848–61. https://journals.sagepub.com/eprint/CXBFFKWZ2IRZVQHZMBDY/full	Q1, IF: 2.633
5	Hafizh, Muhammad et al. 2021. “A Hybrid Piezoelectric-Electromagnetic Nonlinear Vibration Energy Harvester Excited by Fluid Flow.” Comptes Rendus Mécanique 349(1): 65–81. Doi: 10.5802/crmeca.74	Q3, IF: 2.086

Conference Proceedings

i) Muhammad Hafizh, and Asan GA Muthalif. 2021. “Towards Developing a Hybrid Nonlinear Vibration Energy Harvester for Remote Sensing Applications: A Design and Optimization Study.” In Building Resilience at Universities: Role of Innovation and Entrepreneurship, Qatar: Qatar University Press, 55–55.

ii) Muhammad Hafizh, Asan G.A Muthalif, Jamil Renno, and M.R Paurobally. 2022. “Airfoil-Based Self-Adjustable Piezoelectric Energy Harvester in Fluid-Flow Applications for Performance Optimization.” In Proceedings of the 28th International Congress on Sound and Vibration, Singapore.

iii) Muhammad Hafizh, Asan G.A. Muthalif, Jamil Renno, and M.R. Paurobally. 2021. “A Nonlinear Vibration Energy Harvester with Bandwidth Enhancement Excited by Fluid Flow.” In International Conference on Electronics, Instrumentation and Devices (ICEID 2021), Malaysia, 49–53.

Industrial Conferences

i) Muhammad Hafizh, Asan G.A Muthalif, 17th Qatargas Engineering Forum, December 2021.

ii) Muhammad Hafizh, Asan G.A Muthalif, 2nd Research and Innovation Competition, Gulf Petrochemical and Chemical Association, September 2022.

REFERENCES

[1] M.R. Maghami, H. Hizam, C. Gomes, M.A. Radzi, M.I. Rezadad, S. Hajighorbani, Power loss due to soiling on solar panel: A review, Renew. Sustain. Energy Rev. 59 (2016) 1307–1316. https://doi.org/10.1016/j.rser.2016.01.044.

[2] N.E. Dutoit, B.L. Wardle, S.-G. Kim, Desin considerations for MEMS-scale piezoelectric mechanical vibration energy harvesters, Integr. Ferroelectr. 71 (2005) 121–160. https://doi.org/10.1080/10584580590964574.

[3] T.H. Ng, W.H. Liao, Sensitivity analysis and energy harvesting for a self-powered piezoelectric sensor, J. Intell. Mater. Syst. Struct. 16 (2005) 785–797. https://doi.org/10.1177/1045389X05053151.

[4] M. Safaei, H.A. Sodano, S.R. Anton, A review of energy harvesting using piezoelectric materials: State-of-the-art a decade later (2008-2018), Smart Mater. Struct. 28 (2019) 113001. https://doi.org/10.1088/1361-665X/ab36e4.

[5] H.A. Sodano, D.J. Inman, G. Park, Comparison of Piezoelectric Energy Harvesting Devices for Recharging Batteries, J. Intell. Mater. Syst. Struct. 16 (2005) 799–807. https://doi.org/10.1177/1045389X05056681.

[6] H. Elahi, M. Eugeni, P. Gaudenzi, A Review on Mechanisms for Piezoelectric-Based Energy Harvesters, Energies. 11 (2018). https://doi.org/10.3390/en11071850.

[7] S. Roundy, P.K. Wright, A piezoelectric vibration based generator for wireless electronics, Smart Mater. Struct. 13 (2004) 1131–1142. https://doi.org/10.1088/0964-1726/13/5/018.

[8] A.G.A. Muthalif, N.H.D. Nordin, Optimal piezoelectric beam shape for single and broadband vibration energy harvesting: Modeling, simulation and experimental results, Mech. Syst. Signal Process. 54 (2015) 417–426. https://doi.org/10.1016/j.ymssp.2014.07.014.

[9] M. Ferrari, D. Alghisi, M. Baù, V. Ferrari, Nonlinear multi-frequency converter array for vibration energy harvesting in autonomous sensors, in: Procedia Eng., Elsevier Ltd, 2012: pp. 410–413. https://doi.org/10.1016/j.proeng.2012.09.171.

[10] M.F. Lumentut, L.A. Francis, I.M. Howard, Analytical techniques for broadband multielectromechanical piezoelectric bimorph beams with multifrequency power harvesting, IEEE Trans. Ultrason. Ferroelectr. Freq. Control. 59 (2012)

2555–2568. https://doi.org/10.1109/TUFFC.2012.2489.

[11] D. Maurath, P.F. Becker, D. Spreemann, Y. Manoli, Efficient Energy Harvesting With Electromagnetic Energy Transducers Using Active Low-Voltage Rectification and Maximum Power Point Tracking, IEEE J. Solid-State Circuits. 47 (2012) 1369–1380. https://doi.org/10.1109/JSSC.2012.2188562.

[12] S.P. Beeby, M.J. Tudor, N.M. White, Energy harvesting vibration sources for microsystems applications, Meas. Sci. Technol. 17 (2006) R175–R195. https://doi.org/10.1088/0957-0233/17/12/r01.

[13] J. Zhao, H. Zhang, F. Su, Z. Yin, A novel model of piezoelectric-electromagnetic hybrid energy harvester based on vortex-induced vibration, in: 2017 Int. Conf. Green Energy Appl., 2017: pp. 105–108. https://doi.org/10.1109/ICGEA.2017.7925464.

[14] Z. Lai, S. Wang, L. Zhu, G. Zhang, J. Wang, K. Yang, D. Yurchenko, A hybrid piezo-dielectric wind energy harvester for high-performance vortex-induced vibration energy harvesting, Mech. Syst. Signal Process. 150 (2021). https://doi.org/10.1016/j.ymssp.2020.107212.

[15] V.R. Challa, M.G. Prasad, F.T. Fisher, A coupled piezoelectric-electromagnetic energy harvesting technique for achieving increased power output through damping matching, Smart Mater. Struct. 18 (2009) 095029. https://doi.org/10.1088/0964-1726/18/9/095029.

[16] D.S. Ibrahim, A.G.A. Muthalif, N.H.D. Nordin, T. Saleh, Comparative study of conventional and magnetically coupled piezoelectric energy harvester to optimize output voltage and bandwidth, Microsyst. Technol. 23 (2017) 2663–2674. https://doi.org/10.1007/s00542-016-3066-1.

[17] A. Ali, A.G.A. Muthalif, J. Renno, Broadband vibration energy harvesting from a non-deterministic system: Performance of different piezoelectric patch shapes, Mater. Res. Express. 8 (2021) 25702. https://doi.org/10.1088/2053-1591/abe063.

[18] J. Wang, L. Geng, L. Ding, H. Zhu, D. Yurchenko, The state-of-the-art review on energy harvesting from flow-induced vibrations, Appl. Energy. 267 (2020) 114902. https://doi.org/10.1016/j.apenergy.2020.114902.

[19] R. Song, X. Shan, F. Lv, T. Xie, A study of vortex-induced energy harvesting from water using PZT piezoelectric cantilever with cylindrical extension, in: Ceram. Int., Elsevier Ltd, 2015: pp. S768–S773.

https://doi.org/10.1016/j.ceramint.2015.03.262.

[20] R. Song, X. Shan, J. Li, T. Xie, Q. Sun, A piezoelectric energy harvester with vortex induced vibration, in: 2015 Symp. Piezoelectricity, Acoust. Waves, Device Appl., 2015: pp. 322–325. https://doi.org/10.1109/SPAWDA.2015.7364499.

[21] R.D. Gabbai, H. Benaroya, An overview of modeling and experiments of vortex-induced vibration of circular cylinders, J. Sound Vib. 282 (2005) 575–616. https://doi.org/https://doi.org/10.1016/j.jsv.2004.04.017.

[22] B. Han, S. Vassilaras, C.B. Papadias, R. Soman, M.A. Kyriakides, T. Onoufriou, R.H. Nielsen, R. Prasad, Harvesting energy from vibrations of the underlying structure, J. Vib. Control. 19 (2013) 2255–2269. https://doi.org/10.1177/1077546313501537.

[23] M.E. Kiziroglou, D.E. Boyle, S.W. Wright, E.M. Yeatman, Acoustic power delivery to pipeline monitoring wireless sensors, Ultrasonics. 77 (2017) 54–60. https://doi.org/10.1016/j.ultras.2017.01.017.

[24] M.I. Mohamed, W.Y. Wu, M. Moniri, Power harvesting for smart sensor networks in monitoring water distribution system, 2011 Int. Conf. Networking, Sens. Control. ICNSC 2011. (2011) 393–398. https://doi.org/10.1109/ICNSC.2011.5874897.

[25] M.E. Kiziroglou, E.M. Yeatman, Micromechanics for energy generation, J. Micromechanics Microengineering. 31 (2021) 114003. https://doi.org/10.1088/1361-6439/AC2A52.

[26] W. Cai, R.L. Harne, Investigations on energy harvesting systems incorporating mechanical and electrical nonlinearities to charge reusable batteries, Energy Convers. Manag. 252 (2022) 115045. https://doi.org/10.1016/j.enconman.2021.115045.

[27] H. Wang, Q. Meng, Analytical modeling and experimental verification of vibration-based piezoelectric bimorph beam with a tip-mass for power harvesting, Mech. Syst. Signal Process. 36 (2013) 193–209. https://doi.org/10.1016/j.ymssp.2012.10.015.

[28] S. Hurlebaus, L. Gaul, Smart structure dynamics, Mech. Syst. Signal Process. 20 (2006) 255–281. https://doi.org/10.1016/j.ymssp.2005.08.025.

[29] K. Fan, S. Liu, H. Liu, Y. Zhu, W. Wang, D. Zhang, Scavenging energy from ultra-low frequency mechanical excitations through a bi-directional hybrid

energy harvester, Appl. Energy. 216 (2018) 8–20. https://doi.org/10.1016/j.apenergy.2018.02.086.

[30] Z. Yang, S. Zhou, J. Zu, D. Inman, High-Performance Piezoelectric Energy Harvesters and Their Applications, Joule. 2 (2018) 642–697. https://doi.org/10.1016/J.JOULE.2018.03.011.

[31] D. Teso-Fz-Betoño, I. Aramendia, J. Martinez-Rico, U. Fernandez-Gamiz, E. Zulueta, Piezoelectric Energy Harvesting Controlled with an IGBT H-Bridge and Bidirectional Buck–Boost for Low-Cost 4G Devices, Sensors. 20 (2020). https://doi.org/10.3390/s20247039.

[32] W. Sun, D. Zhao, T. Tan, Z. Yan, P. Guo, X. Luo, Low velocity water flow energy harvesting using vortex induced vibration and galloping, Appl. Energy. 251 (2019) 113392. https://doi.org/10.1016/j.apenergy.2019.113392.

[33] A. Abdelkefi, Z. Yan, M.R. Hajj, Performance analysis of galloping-based piezoaeroelastic energy harvesters with different cross-section geometries, J. Intell. Mater. Syst. Struct. 25 (2014) 246–256. https://doi.org/10.1177/1045389X13491019.

[34] Y. Cao, D. Cao, G. He, X. Ge, Y. Hao, Vibration analysis and distributed piezoelectric energy harvester design for the L-shaped beam, Eur. J. Mech. A/Solids. 87 (2021) 104214. https://doi.org/10.1016/j.euromechsol.2021.104214.

[35] B.C. Jung, H. Yoon, H. Oh, G. Lee, M. Yoo, B.D. Youn, Y.C. Huh, Hierarchical model calibration for designing piezoelectric energy harvester in the presence of variability in material properties and geometry, Struct. Multidiscip. Optim. 53 (2016) 161–173. https://doi.org/10.1007/s00158-015-1310-4.

[36] J. Zhang, C. Shu, Z. Fang, Optimal piezoelectric energy harvesting from wind-induced vibration, Ferroelectrics. 506 (2017) 10–23. https://doi.org/10.1080/00150193.2017.1281684.

[37] M. Hafizh, A.G. Muthalif, J. Renno, M.. Paurobally, Airfoil-Based Self-Adjustable Piezoelectric Energy Harvester in Fluid-Flow Applications for Performance Optimization, in: Proc. 28th Int. Congr. Sound Vib., Singapore, 2022.

[38] W. Xu, M. Yang, E. Wang, H. Sun, Performance of single-cylinder VIVACE converter for hydrokinetic energy harvesting from flow-induced vibration near a free surface, Ocean Eng. 218 (2020) 108168.

https://doi.org/10.1016/j.oceaneng.2020.108168.

[39] F. Pan, Z. Xu, L. Jin, P. Pan, X. Gao, Designed Simulation and Experiment of a Piezoelectric Energy Harvesting System Based on Vortex-Induced Vibration, IEEE Trans. Ind. Appl. 53 (2017) 3890–3897. https://doi.org/10.1109/TIA.2017.2687401.

[40] R.D. Blevins, C.S. Coughran, Experimental investigation of vortex-induced vibration in one and two dimensions with variable mass, damping, and reynolds number, J. Fluids Eng. Trans. ASME. 131 (2009) 1012021–1012027. https://doi.org/10.1115/1.3222904.

[41] J.K. Vandiver, J.-Y. Jong, The relationship between in-line and cross-flow vortex-induced vibration of cylinders, J. Fluids Struct. 1 (1987) 381–399. https://doi.org/https://doi.org/10.1016/S0889-9746(87)90279-9.

[42] A. Khalak, C.H.K. Williamson, Motions, forces and mode transitions in vortex-induced vibration at low mass damping, J. Fluids Struct. 13 (1999) 813–851. https://doi.org/10.1006/jfls.1999.0236.

[43] C.H.K. Williamson, R. Govardhan, VORTEX-INDUCED VIBRATIONS, Annu. Rev. Fluid Mech. 36 (2004) 413–455. https://doi.org/10.1146/annurev.fluid.36.050802.122128.

[44] T. Sarpkaya, A critical review of the intrinsic nature of vortex-induced vibrations, J. Fluids Struct. 19 (2004) 389–447. https://doi.org/10.1016/j.jfluidstructs.2004.02.005.

[45] P.W. Bearman, Circular cylinder wakes and vortex-induced vibrations, J. Fluids Struct. 27 (2011) 648–658. https://doi.org/10.1016/j.jfluidstructs.2011.03.021.

[46] C. Norberg, Fluctuating lift on a circular cylinder: Review and new measurements, J. Fluids Struct. 17 (2003) 57–96. https://doi.org/10.1016/S0889-9746(02)00099-3.

[47] R.D. Blevins, Models for Vortex-Induced Vibration of Cylinders Based on Measured Forces, J. Fluids Eng. 131 (2009). https://doi.org/10.1115/1.3222906.

[48] E. Konstantinidis, D. Dorogi, L. Baranyi, Resonance in vortex-induced in-line vibration at low Reynolds numbers, J. Fluid Mech. 907 (2020) 34. https://doi.org/10.1017/jfm.2020.850.

[49] A.M.G. de Lima, B.S.C. da Cunha, A.R. da Silva, L.F.F. Rodovalho, Vortex-induced vibration analysis of viscoelastically mounted rigid circular cylinders in cross-flow at a moderate Reynolds number, J. Vib. Control. 24 (2018) 2688–

2700. https://doi.org/10.1177/1077546317733656.

[50] C.H.K. Williamson, R. Govardhan, A brief review of recent results in vortex-induced vibrations, J. Wind Eng. Ind. Aerodyn. 96 (2008) 713–735. https://doi.org/10.1016/j.jweia.2007.06.019.

[51] J. Wang, J. Ran, Z. Zhang, Energy harvester based on the synchronization phenomenon of a circular cylinder, Math. Probl. Eng. 2014 (2014). https://doi.org/10.1155/2014/567357.

[52] A. Mehmood, A. Abdelkefi, M.R. Hajj, A.H. Nayfeh, I. Akhtar, A.O. Nuhait, Piezoelectric energy harvesting from vortex-induced vibrations of circular cylinder, J. Sound Vib. 332 (2013) 4656–4667. https://doi.org/10.1016/j.jsv.2013.03.033.

[53] J.A.B. Gripp, D.A. Rade, Vibration and noise control using shunted piezoelectric transducers: A review, Mech. Syst. Signal Process. 112 (2018) 359–383. https://doi.org/10.1016/j.ymssp.2018.04.041.

[54] A.G.A. Muthalif, A.N. Wahid, Optimal piezoelectric shunt dampers for non - deterministic substructure vibration control : estimation and parametric investigation, Sci. Rep. (2021) 1–15. https://doi.org/10.1038/s41598-021-84097-w.

[55] D. Maurath, P.F. Becker, D. Spreemann, Y. Manoli, Efficient energy harvesting with electromagnetic energy transducers using active low-voltage rectification and maximum power point tracking, IEEE J. Solid-State Circuits. 47 (2012) 1369–1380. https://doi.org/10.1109/JSSC.2012.2188562.

[56] Z. Yan, G. Shi, J. Zhou, L. Wang, L. Zuo, T. Tan, Wind piezoelectric energy harvesting enhanced by elastic-interfered wake-induced vibration, Energy Convers. Manag. 249 (2021) 114820. https://doi.org/10.1016/j.enconman.2021.114820.

[57] Z. Chen, M.M. Alam, B. Qin, Y. Zhou, Energy harvesting from and vibration response of different diameter cylinders, Appl. Energy. 278 (2020) 115737. https://doi.org/10.1016/J.APENERGY.2020.115737.

[58] I. Aramendia, A. Saenz-Aguirre, A. Boyano, U. Fernandez-Gamiz, E. Zulueta, Oscillating U-Shaped Body for Underwater Piezoelectric Energy Harvester Power Optimization, Micromachines. 10 (2019). https://doi.org/10.3390/mi10110737.

[59] I. Aramendia, U. Fernandez-Gamiz, E.Z. Guerrero, J.M. Lopez-Guede, J.

Sancho, Power control optimization of an underwater piezoelectric energy harvester, Appl. Sci. 8 (2018). https://doi.org/10.3390/app8030389.

[60] H.D. Akaydin, N. Elvin, Y. Andreopoulos, The performance of a self-excited fluidic energy harvester, Smart Mater. Struct. 21 (2012) 025007. https://doi.org/10.1088/0964-1726/21/2/025007.

[61] M. Hafizh, A.G.A. Muthalif, J. Renno, M.R. Paurobally, M.A. Arab, I. Bahadur, H. Ouakad, A hybrid piezoelectric-electromagnetic nonlinear vibration energy harvester excited by fluid flow, Comptes Rendus Mécanique. 349 (2021) 65–81. https://doi.org/10.5802/crmeca.74.

[62] A.G.. Muthalif, M. Hafizh, J. Renno, M.R. Paurobally, A hybrid piezoelectric-electromagnetic energy harvester from vortex-induced vibrations in fluid-flow; the influence of boundary condition in tuning the harvester, Energy Convers. Manag. 256 (2022) 115371. https://doi.org/10.1016/j.enconman.2022.115371.

[63] M. Al-Riyami, I. Bahadur, H. Ouakad, There Is Plenty of Room inside a Bluff Body: A Hybrid Piezoelectric and Electromagnetic Wind Energy Harvester, Energies. 15 (2022). https://doi.org/10.3390/en15166097.

[64] H. Mirab, R. Fathi, V. Jahangiri, M.M. Ettefagh, R. Hassannejad, Energy harvesting from sea waves with consideration of airy and JONSWAP theory and optimization of energy harvester parameters, J. Mar. Sci. Appl. 14 (2015) 440–449. https://doi.org/10.1007/s11804-015-1327-5.

[65] D. Yadav, J. Yadav, R. Vashistha, D.P. Goyal, D. Chhabra, Modeling and simulation of an open channel PEHF system for efficient PVDF energy harvesting, Mech. Adv. Mater. Struct. 28 (2021) 812–826. https://doi.org/10.1080/15376494.2019.1601307.

[66] L.B. Zhang, A. Abdelkefi, H.L. Dai, R. Naseer, L. Wang, Design and experimental analysis of broadband energy harvesting from vortex-induced vibrations, J. Sound Vib. 408 (2017) 210–219. https://doi.org/10.1016/j.jsv.2017.07.029.

[67] J. Jianan, B. Liang, L. Yuren, G. Yingsong, H. Pengju, Design and analysis of the energy conversion device in the electromagnetic aeroelastic energy harvesting system, in: IECON 2017 - 43rd Annu. Conf. IEEE Ind. Electron. Soc., 2017: pp. 4130–4136. https://doi.org/10.1109/IECON.2017.8216708.

[68] X. Tang, L. Zuo, Enhanced vibration energy harvesting using dual-mass systems, J. Sound Vib. 330 (2011) 5199–5209.

https://doi.org/10.1016/j.jsv.2011.05.019.

[69] Y. Nishi, Power extraction from vortex-induced vibration of dual mass system, J. Sound Vib. 332 (2013) 199–212. https://doi.org/10.1016/j.jsv.2012.08.018.

[70] J. Xu-Xu, A. Barrero-Gil, A. Velazquez, Dual mass system for enhancing energy extraction from Vortex-Induced Vibrations of a circular cylinder, Int. J. Mar. Energy. 16 (2016) 250–261. https://doi.org/10.1016/j.ijome.2016.08.002.

[71] D. Zhao, X. Hu, T. Tan, Z. Yan, W. Zhang, Piezoelectric galloping energy harvesting enhanced by topological equivalent aerodynamic design, Energy Convers. Manag. 222 (2020) 113260. https://doi.org/10.1016/j.enconman.2020.113260.

[72] C.H.K. Williamson, R. Govardhan, Vortex-induced vibrations, Annu. Rev. Fluid Mech. 36 (2004) 413–455. https://doi.org/10.1146/annurev.fluid.36.050802.122128.

[73] M.K. Kwak, D.H. Yang, Dynamic modelling and active vibration control of a submerged rectangular plate equipped with piezoelectric sensors and actuators, J. Fluids Struct. 54 (2015) 848–867. https://doi.org/10.1016/J.JFLUIDSTRUCTS.2015.02.001.

[74] S. Daneshvar, C. Morton, On the vortex-induced vibration of a low mass ratio circular cylinder near a planar boundary, Ocean Eng. 201 (2020) 107109. https://doi.org/10.1016/J.OCEANENG.2020.107109.

[75] A. Munir, M. Zhao, H. Wu, D. Ning, L. Lu, Numerical investigation of the effect of plane boundary on two-degree-of-freedom of vortex-induced vibration of a circular cylinder in oscillatory flow, Ocean Eng. 148 (2018) 17–32. https://doi.org/10.1016/J.OCEANENG.2017.11.022.

[76] M. Hafizh, A.G.A. Muthalif, J. Renno, M.R. Paurobally, A vortex-induced vibration-based self-tunable airfoil-shaped piezoelectric energy harvester for remote sensing applications in water, Ocean Eng. 269 (2023) 113467. https://doi.org/10.1016/j.oceaneng.2022.113467.

[77] A.G.A. Muthalif, M. Hafizh, J. Renno, M.R. Paurobally, An enhanced hybrid piezoelectric–electromagnetic energy harvester using dual-mass system for vortex-induced vibrations, JVC/Journal Vib. Control. 27 (2021) 2848–2861. https://doi.org/10.1177/10775463211041875.

[78] X. Li, Z. Li, B. Liu, J. Zhang, W. Zhu, Numerical research on a vortex shedding induced piezoelectric- electromagnetic energy harvester, (2021) 1–16.

https://doi.org/10.1177/1045389X211011665.

[79] H. Zhang, R. Song, J. Meng, X. Li, W. Sui, A direction adaptive hybrid piezo-electromagnetic energy harvester based on vortex-induced vibration, Ferroelectrics. 584 (2021) 113–120. https://doi.org/10.1080/00150193.2021.1984778.

[80] U.J.A. Abdelkefi, Characteristics and comparative analysis of piezoelectric-electromagnetic energy harvesters from vortex-induced oscillations, Nonlinear Dyn. 95 (2019) 3309–3333. https://doi.org/10.1007/s11071-018-04757-x.

[81] Y. Tadesse, Shujun Zhang, S. Priya, Multimodal energy harvesting system: Piezoelectric and electromagnetic, J. Intell. Mater. Syst. Struct. 20 (2009) 625–632. https://doi.org/10.1177/1045389X08099965.

[82] D. Cao, X. Ding, X. Guo, M. Yao, Design, Simulation and Experiment for a Vortex-Induced Vibration Energy Harvester for Low-Velocity Water Flow, Int. J. Precis. Eng. Manuf. - Green Technol. 8 (2021) 1239–1252. https://doi.org/10.1007/s40684-020-00265-9.

[83] G. Shi, T. Tan, S. Hu, Z. Yan, Hydrodynamic piezoelectric energy harvesting with topological strong vortex by forced separation, Int. J. Mech. Sci. 223 (2022) 107261. https://doi.org/10.1016/j.ijmecsci.2022.107261.

[84] SmartMaterials, Macro fiber composite - MFC, Sensor, Energy Harvester Energy Harvesting Systems Piezo Powering and Instrumentation Engineering Services, n.d. www.smart-material.com (accessed February 10, 2021).

[85] G. Donoso, C.L. Ladera, P. Martín, Magnetically coupled magnet-spring oscillators, Eur. J. Phys. 31 (2010) 433–452. https://doi.org/10.1088/0143-0807/31/3/002.

[86] C.G. Rodriguez, E. Egusquiza, X. Escaler, Q.W. Liang, F. Avellan, Experimental investigation of added mass effects on a Francis turbine runner in still water, J. Fluids Struct. 22 (2006) 699–712. https://doi.org/10.1016/j.jfluidstructs.2006.04.001.

[87] R.P.S. Han, H. Xu, A simple and accurate added mass model for hydrodynamic fluid—Structure interaction analysis, J. Franklin Inst. 333 (1996) 929–945. https://doi.org/10.1016/0016-0032(96)00043-9.

[88] A. Placzek, J.F. Sigrist, A. Hamdouni, Numerical simulation of an oscillating cylinder in a cross-flow at low Reynolds number: Forced and free oscillations, Comput. Fluids. 38 (2009) 80–100.

https://doi.org/10.1016/j.compfluid.2008.01.007.

[89] K. Lam, J.Y. Li, R.M.C. So, Force coefficients and Strouhal numbers of four cylinder in cross flow, J. Fluids Struct. 18 (2003) 305–324. https://doi.org/10.1016/j.jfluidstructs.2003.07.008.

[90] N.B. Khan, Z. Ibrahim, Numerical investigation of vortex-induced vibration of an elastically mounted circular cylinder with One-degree of freedom at high Reynolds number using different turbulent models, Proc. Inst. Mech. Eng. Part M J. Eng. Marit. Environ. 233 (2018) 443–453. https://doi.org/10.1177/1475090217751992.

[91] Y. Fang, Z. Han, Numerical experimental research on the hydrodynamic performance of flow around a three dimensional circular cylinder, Appl. Mech. Mater. 90–93 (2011) 2778–2781. https://doi.org/10.4028/www.scientific.net/AMM.90-93.2778.

[92] M.M. Zdravkovich, Conceptual overview of laminar and turbulent flows past smooth and rough circular cylinders, J. Wind Eng. Ind. Aerodyn. 33 (1990) 53–62. https://doi.org/10.1016/0167-6105(90)90020-D.

[93] F.R. Menter, Two-equation eddy-viscosity turbulence models for engineering applications, AIAA J. 32 (1994) 1598–1605. https://doi.org/10.2514/3.12149.

[94] ANSYS Inc., ANSYS FLUENT User's Guide, Cannonsburg, 2021.

[95] S. Dong, G.E. Karniadakis, DNS of flow past a stationary and oscillating cylinder at Re = 10000, J. Fluids Struct. 20 (2005) 519–531. https://doi.org/10.1016/j.jfluidstructs.2005.02.004.

[96] V.-T. Nguyen, H.H. Nguyen, Detached eddy simulations of flow induced vibrations of circular cylinders at high Reynolds numbers, J. Fluids Struct. 63 (2016) 103–119. https://doi.org/https://doi.org/10.1016/j.jfluidstructs.2016.02.004.

[97] R. Jin, M. Liu, B. Geng, X. Jin, H. Zhang, Y. Liu, Numerical Investigation of Vortex Induced Vibration for Submerged Floating Tunnel under Different Reynolds Numbers, Water . 12 (2020). https://doi.org/10.3390/w12010171.

[98] A. Erturk, D.J. Inman, A Distributed Parameter Electromechanical Model for Cantilevered Piezoelectric Energy Harvesters, J. Vib. Acoust. 130 (2008). https://doi.org/10.1115/1.2890402.

[99] Y. Kuang, M. Zhu, Evaluation and validation of equivalent properties of macro fibre composites for piezoelectric transducer modelling, Compos. Part B Eng.

158 (2019) 189–197. https://doi.org/10.1016/j.compositesb.2018.09.068.

[100] Z. Li, Y. Liu, P. Yin, Y. Peng, J. Luo, S. Xie, H. Pu, Constituting abrupt magnetic flux density change for power density improvement in electromagnetic energy harvesting, Int. J. Mech. Sci. 198 (2021) 106363. https://doi.org/10.1016/j.ijmecsci.2021.106363.

[101] H. Zhou, C. Xu, C. Lu, X. Jiang, Z. Zhang, J. Wang, X. Xiao, M. Xin, L. Wang, Investigation of transient magnetoelectric response of magnetostrictive/piezoelectric composite applicable for lightning current sensing, Sensors Actuators, A Phys. 329 (2021) 112789. https://doi.org/10.1016/j.sna.2021.112789.

[102] M. Hafizh, A.G.A. Muthalif, J. Renno, M.R. Paurobally, I. Bahadur, H. Ouakad, M. Sultan Mohamed Ali, Vortex induced vibration energy harvesting using magnetically coupled broadband circular-array piezoelectric patch: Modelling, parametric study, and experiments, Energy Convers. Manag. 276 (2023) 116559. https://doi.org/10.1016/j.enconman.2022.116559.

APPENDIX A: STATE SPACE EQUATIONS

PEH System with Tip Mass

$$z_1 = \theta(t), z_2 = \dot{\theta}(t), z_3 = V(t) \quad \text{Eq. 44}$$

$$\dot{z_1} = \dot{\theta}(t), \dot{z_2} = \ddot{\theta}(t), \dot{z_3} = \dot{V}(t) \quad \text{Eq. 45}$$

$$\dot{z_1}(t) = z_2(t) \quad \text{Eq. 46}$$

$$a_3 = f + \frac{\alpha^2 \cdot a^2}{K_p \cdot K_{trans}} \quad \text{Eq. 47}$$

$$\dot{z_2}(t) = -\frac{C_{eq}}{M_{eq}} \cdot \dot{\theta}(t) - \frac{K_{eq}}{M_{eq}} \cdot \theta(t) - \frac{\Theta}{l_B \times M_{eq}} \cdot V(t) - \mu \ddot{\theta_0}(t) \quad \text{Eq. 48}$$

$$\dot{z_2}(t) = -\frac{C_{eq}}{M_{eq}} z_2(t) - \frac{K_{eq}}{M_{eq}} z_1(t) - \frac{\Theta}{l_B \times M_{eq}} z_3(t) - \mu \ddot{\theta_0}(t) \quad \text{Eq. 49}$$

$$\dot{z_3}(t) = -\frac{V(t)}{C^s R_l} + \Theta_f \cdot \theta(t) \quad \text{Eq. 50}$$

$$\dot{z_3}(t) = -\frac{z_3}{C^s R_l}(t) + \Theta_f z_1(t) \quad \text{Eq. 51}$$

Combined System with Tip Mass

$$y_1 = x(t), y_2 = \dot{x}(t), y_3 = \theta(t), y_4 = \dot{\theta}(t), y_5 = I(t) \quad \text{Eq. 52}$$

$$\dot{y}_1 = \dot{x}(t), \dot{y}_2 = \ddot{x}(t), \dot{y}_3 = \dot{\theta}(t), \dot{y}_4 = \ddot{\theta}(t), \dot{y}_5 = \dot{I}(t) \quad \text{Eq. 53}$$

$$\dot{y}_1(t) = y_2(t) \quad \text{Eq. 54}$$

$$\dot{y}_2(t) = -\frac{K}{M} \cdot x(t) + \left(l + x_0 + x(t)\right) \cdot \dot{\theta}^2(t) + g\cos\left(\theta(t)\right) - BL_{coil} \cdot I(t) \quad \text{Eq. 55}$$

$$\dot{y}_2(t) = -\frac{K}{M} y_1(t) + \left(l + x_0 + y_1(t)\right) \times \left(y_4(t)\right)^2 + g\cos\left(y_3(t)\right) - BL_{coil} \times y_5(t) \quad \text{Eq. 56}$$

$$\dot{y}_3(t) = y_4(t) \quad \text{Eq. 57}$$

$$\dot{y}_4(t) = -\frac{2 \cdot \dot{\theta}(t) \cdot \dot{x}(t)}{M(l + x_0 + x(t))} \quad \text{Eq. 58}$$

$$\dot{y}_4(t) = -\frac{2y_4(t)y_2(t)}{M\left(l + x_0 + y_1(t)\right)} \quad \text{Eq. 59}$$

$$\dot{y}_5(t) = \frac{B \cdot L_{coil} \cdot \dot{x}(t)}{L_{ind}} - \frac{R \cdot I(t)}{L_{ind}} \quad \text{Eq. 60}$$

$$\dot{y}_5(t) = \frac{B \cdot L_{coil} \cdot y_2}{L_{ind}} - \frac{R \cdot y_5}{L_{ind}} \quad \text{Eq. 61}$$

$$q_1 = \theta(t), q_2 = \dot{\theta}(t), q_3 = V_\theta(t), q_4 = x(t), q_5 = \dot{x}(t), q_6 = V_x(t) \quad \text{Eq. 62}$$

$$\dot{q}_1 = \dot{\theta}(t), \dot{q}_2 = \ddot{\theta}(t), \dot{q}_3 = \dot{V}_\theta(t), \dot{q}_4 = x(t), \dot{q}_5 = \ddot{x}(t), \dot{q}_6 = \dot{V}_x(t) \quad \text{Eq. 63}$$

$$\dot{q}_1(t) = q_2(t) \quad \text{Eq. 64}$$

$$\dot{q}_2(t) = \frac{a_1}{a_2} \cdot C_L(t) - \frac{a_3}{a_2} \cdot \dot{\theta}(t) + \frac{a_4}{a_2} \cdot \theta(t) \quad \text{Eq. 65}$$

$$\dot{q}_2(t) = \frac{a_1}{a_2} \cdot \sin(\omega t) - \frac{a_3}{a_2} \cdot q_2 + \frac{a_4}{a_2} \cdot q_1 \quad \text{Eq. 66}$$

$$\dot{q}_3(t) = \frac{\Theta \cdot \mathrm{l} \cdot \dot{\theta}(t)}{C^s} - \frac{V_\theta(t)}{R_L \cdot C^s} \quad \text{Eq. 67}$$

$$\dot{q}_3(t) = \frac{\Theta \cdot \mathrm{l} \cdot \mathrm{q}_2}{C^s} - \frac{q_3}{R_L \cdot C^s} \quad \text{Eq. 68}$$

$$\dot{q}_4(t) = q_5(t) \dot{y}_4(t) = -\frac{2y_4(t)y_2(t)}{M\left(l + x_0 + y_1(t)\right)} \quad \text{Eq. 69}$$

$$\dot{q}_5(t) = -\frac{k}{m} \cdot x(t) + \left(l + x_0 + x(t)\right) \cdot \dot{\theta}^2 + g\cos\theta(t) - BI(t)L_{coil} \quad \text{Eq. 70}$$

$$\dot{q}_5(t) = -\frac{k}{m} \cdot q_4 + \left(l + x_0 + x(t)\right) \cdot (q_2)^2 + g\cos(q_1) - \frac{B \cdot L_{coil} \cdot q_6}{R_L} \quad \text{Eq. 71}$$

$$\dot{q}_6(t) = \frac{B \cdot L_{coil} \cdot R_L \cdot \dot{x}(t)}{L_{ind}} - \frac{V(t) \cdot R_L}{L_{ind}} \quad \text{Eq. 72}$$

$$\dot{q}_6(t) = \frac{B \cdot L_{coil} \cdot R_L \cdot q_5}{L_{ind}} - \frac{q_6 \cdot R_L}{L_{ind}} \quad \text{Eq. 73}$$

APPENDIX B: TABLE OF PARAMETERS AND VARIABLES

Table 15 List of Parameters and Variables for Dual Piezoelectric Mass Arrangement

Symbol	Description	Value	Unit
D	Main cylinder bluff-body diameter	*58*	*mm*
L	Substrate beam length	*70*	*mm*
d_c	Secondary cylinder bluff-body diameter	*18*	*mm*
l_c	Secondary substrate beam length	*30*	*mm*
H	Main bluff-body height	*60*	*mm*
H_c	Secondary bluff-body height	*30*	*mm*
ρ_{beam}	Beam substrate density	*2770*	*kg/m^3*
$\rho_{cylinder}$	Cylinder bluff-body density	*7850*	*kg/m^3*
ρ_{fluid}	Fluid density	*999*	*kg/m^3*
ρ_{piezo}	Active piezoelectric patch density	*7800*	*kg/m^3*
M	Equivalent system mass	–	*kg*
M_a	Added equivalent mass	–	*kg*
K_m	Main oscillator equivalent spring stiffness	*80*	*N/m*
K_c	Secondary oscillator equivalent spring stiffness	*40*	*N/m*
C_P	Clamp capacitance for piezoelectric transducer	–	*F*
Θ	Electromechanical coupling coefficient	–	*NV^{-1}*
C_m	Added mass coefficient (ratio of added mass to structure mass)	*0.128*	–
A_{2814}	2814-P2 piezoelectric active area	*392*	mm^2
A_{0714}	0714-P2 piezoelectric active area	*98*	mm^2